THESIS FOR THE DEGREE OF LICENCIATE OF ENGINEERING

Preparation and characterization of graphene/metal composites

KRISTOFFER HARR MARTINSEN

Department of Industrial and Materials Science
CHALMERS UNIVERSITY OF TECHNOLOGY
Gothenburg, Sweden 2021

Preparation and characterization of graphene/metal composites

KRISTOFFER HARR MARTINSEN

Department of Industrial and Materials Science
Chalmers University of Technology

ABSTRACT

Since the isolation of graphene in 2004, much research has been conducted to understand this novel material and how its properties can be utilized in different applications. One type of venture involves graphene as a reinforcing filler in metal matrix composites (MMC) which is becoming increasingly prevalent in the automotive and aerospace industries. Such composites combine the machinability and processing flexibility of metals with the unique properties of graphene. In fact, copper-graphene composites have demonstrated ameliorated mechanical strength with thermal conductivities elevated beyond pristine copper. However, the challenges that remain to commercialize copper-graphene composites are numerous. The most challengeable one is that graphene must be uniformly dispersed in the matrix and adhere to copper through an industrially scalable and affordable process. Moreover, the volume fraction of graphene must be efficiently controlled, lest superfluous amounts lead to structural detriment.

In this regard, the emphasis of this study was to investigate a scalable and simple method to obtain such MMC via powder metallurgy. Specifically, gas atomized copper powder was functionalized with 3-aminopropyl-triethoxysilane (APTES) in toluene (APTES-Cu), resulting in a positively charged surface; then aqueously dispersed and negatively charged graphene oxide (GO) could then be self-assembled on the surface APTES@Cu via electrostatic interaction (Cu@APTES-Cu). The thickness of GO layers and morphology on the powder was controlled by modulating APTES grafting duration and APTES concentration in toluene. Cu@APTES-Cu powders were thermally annealed before compaction and sintering in inert atmosphere.

The results show that surface modification of metal powders serves as a scalable and versatile approach to coat graphene on metal particles for the preparation of graphene/metal composites. Surface modification of copper with 0.2 vol% APTES in toluene for 30 minutes was sufficient to obtain composite powders with incomplete GO coating, which nonetheless demonstrated improved hardness. However, cold working of sintered composites was essential to densify the porous structure created by reduced GO during sintering. On the other hand, sintered composite samples that exhibited higher thermal conductivity than copper was obtained with higher APTES and GO loading. After thermal annealing, these thicker GO coatings were found to improve thermal conductivity in sintered composites by acting as thermal bridges between individual composite particles. Despite incomplete sintering of these composites, a 20% increase in thermal conductivity was attainable. Finally, both polarization scans and etching measurements in concentrated HCl and ammonium persulfate (APS) indicate that the GO coating decomposes on the outer surface during sintering. However, the reduced GO coating can retard corrosion of the internal composite structure by diffusion inhibition.

Keywords: Copper, surface functionalization, graphene oxide, metal matrix composite, anticorrosion.

Preface

This licentiate thesis is based on work at Chalmers University of Science and Technology, Department of Industrial and Materials Science. The work was supervised by Prof. Vincenzo Palermo, with assistance from Prof. Uta Klement, Dr. Jinhua Sun and Dr. Zhenyuan Xia.

The overarching goal of this research was to investigate a readily scalable synthesis approach of coating graphene on copper particles, which can be employed in various sintering processes to produce novel composites.

The work detailed herein was carried out by the author, except the X-ray spectrometry and thermogravimetric analysis which was performed by Dr. Jinhua Sun.

APPENDED PAPERS:

Paper I: Coating graphene on Cu for improved thermal, mechanical properties, and printability for additive manufacturing
K. H. Martinsen, J. Sun, A. Kovtun, E. Bojestig, J. Hansson, Y. Liu, J. Liu, U. Klement, E. Hryha, L. Nyborg and V. Palermo
In manuscript

Paper II: Dual anticorrosion protection of Cu by silanes and graphene with controlled thickness
K. H. Martinsen, J. Sun, Z. Xia, A. Kovtun, U. Klement, E. Hryha, L. Nyborg and V. Palermo
In manuscript

Contribution to the appended papers

Paper I: I prepared the samples, performed the characterization, conducted most of the experiments, was involved in the planning and wrote the manuscript in collaboration with the co-authors. Eric Bojestig performed the selective laser sintering of the samples at Chalmers University of Technology. Ya Liu and Josef Hansson performed thermal conductivity measurements, also at Chalmers University of Technology.

Paper II: I prepared the samples, conducted the experiments and wrote the manuscript in collaboration with the co-authors. X-ray spectrometry (XPS) and thermogravimetric analysis (TGA) was performed by Jinhua Sun at Chalmers University of Technology.

Abbreviations

2D	Two-dimensional
APTES	3-aminopropyltriethoxysilane
APS	Ammonium persulfate
ASTM	American Society for Testing and Materials
DI	Deionized
EDS	Energy dispersive spectrometry
GO	Graphene oxide
HIP	Hot isostatic pressing
HV	Hardness Vickers
LFA	Laser flash analysis
rGO	Reduced graphene oxide
SEM	Scanning electron microscopy
SE	Secondary electrons
SLM	Selective laser melting
SLS	Selective laser sintering
SPS	Spark plasma sintering
TGA	Thermogravimetric analysis
XPS	X-ray photospectrometry
XRD	X-ray diffraction
4PP	4 Point probe

Contents

Chapter I - Introduction

Graphene has been extensively studied since its isolation from graphite by Novoselov and Geim in 2004[1]. This attention owes to the unique physical properties of graphene which include exceptional electrical conductivity[1] ($1.5x10^4$ cm^2/Vs), thermal conductivity[2] ($5x10^3 W/mK$) and Young's modulus[3] (1 TPa). Since then, focus has gradually shifted from understanding graphene's fundamental properties to how the material can be practically used and commercialized. One of the main challenges is developing a readily scalable, high yield process for producing monolayers of graphene with large lateral size. As an alternative of perfect graphene which can only be prepared by mechanical exfoliation of graphene in small size, graphene oxide (GO) can be synthesized by a solution processing method from graphite, and after reduction, the reduced graphene oxide (rGO) with high surface area and electrical conductivity can be obtained in large scale for various applications.

While potential applications of rGO are numerous, one of particular interest is as a filler in copper to create a metal matrix composite (MMC) material[4]. For instance, if properly integrated into the copper matrix, rGO can complement copper with its own unique properties. Specifically, it is proposed that rGO can ameliorate wear resistance while improving copper's thermal and electric conductivity[5]. In addition, rGO can act as a protective coating against corrosion[6],[7].

However, for such MMC composites to be commercially available, their production must be inexpensive and readily scalable. This requires developing a facile method to uniformly incorporate GO throughout the copper matrix, in addition to stringent requirements on sheet size and morphology. Moreover, since the interfacial interaction between graphene (oxide) sheets and metal surfaces is very weak and only limited to van der Waals forces, it is necessary to modify the surface chemistry of either constituent to improve their interaction.

To this end, powder metallurgy of surface modified copper powder is promising. By modifying the surface chemistry of copper particles with specific functional molecules, the GO can be homogeneously dispersed in a powder feedstock by increased interaction between graphene and the copper surface. The resultant graphene/Cu composite powder can then be utilized in processes ranging from conventional press-and-sintering to additive manufacturing for further applications.

Research objectives

The main purpose of this research is to develop a facile and scalable method for surface engineering of copper power with GO. To this end, the work in this thesis is twofold.

The first part concerns the process and chemistry behind surface modification of copper powder with GO. This involves adjusting the processing parameters such as loading of functional molecules and graphene to control the thickness of graphene coating.

The second part investigates the effect of this coating and what properties it bestows. Herein, sintered composites of copper-graphene are evaluated and compared with pure copper. This involves investigation of corrosion rates of powders, as well as mechanical and conductive performance in sintered samples.

Thus, the overarching research objectives are the following:

1. What synthesis mechanisms determine the coating quality of GO on copper powders?
2. How can GO thickness and morphology be controlled by changing synthesis parameters?
3. How the graphene coating affects the properties and performance of copper?
4. How can copper powder modified with a GO coating find use in industry?

Limitations

Samples in this work were only sintered in a conventional ceramic furnace, so an evaluation of sample properties as a factor of thermal processing methods was not part of this scope. Furthermore, limitations in machining prevented preparation of specimens for tensile testing. Only hardness testing could be used to evaluate mechanical performance of samples.

Chapter II - Background

Graphene and its properties

Graphene is a two-dimensional (2D), one-atom thick lattice consisting solely of covalently bound carbon atoms (Figure 1a). To form this highly ordered structure, the valence electrons in carbon are in planar sp^2 orbitals and covalently bond through σ-bonds. These hybrid orbitals are amalgamations of 3 valence electron orbital configurations in carbon, namely the s, p_x and p_y orbitals. In other words, 3 out of 4 valence electrons in a carbon atom are tightly bound to the base plane in these electron orbitals and covalently bind to the s, p_x or p_y orbitals of neighboring atoms. The fourth electron is in a delocalized, unbound state in the p_z orbital which can interact with p_z electrons in adjacent carbon atoms. This is called a π-bond and together with the σ-bonds, it constitutes the double bonds found in aromatic compounds. In this sense, graphene is structurally similar to polyaromatic molecules.

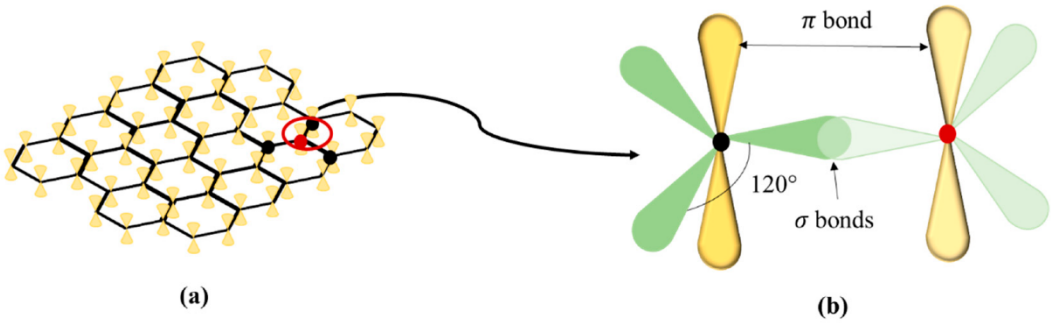

Figure 1: *(a) Crystal structure of Graphene with visible π orbitals, (b) sp^2 configuration in graphene. Adapted from Karimi et al.[8] under the Creative Commons license.*

This highly ordered and covalent structure, in conjunction with delocalized electrons, gives graphene some interesting properties not found in most other materials. Perfect graphene, meaning a detached single layer from graphite, can boast of a 1 TPa Young's modulus and an intrinsic strength of 130 GPa, making it one of the strongest materials known to date[3]. In addition, electrons in graphene has no forbidden energy states and are in this sense "gapless", resulting in reminiscent of metallic electron transport. Combined with its delocalized π-electrons, this endows graphene with very high electron mobility[9] and electrical conductivity in the lateral plane[1].

Graphene is also hydrophobic, chemically inert, and impermeable by most gases. Moreover, the pure and isolated monolayers of graphene show ultrahigh thermal conductivity[2] (5000 W/mK), which is more than ten times higher than bulk copper. All these properties make graphene a very attractive material for a plethora of applications, including microelectronics[10], heat exchangers[11], filters and sensors[12]. Another interesting application is as a filler in polymer or metal based composite materials[13], in which graphene nanosheets would be incorporated to improve the physical properties of matrix material.

However, while these novel properties of graphene created entirely new fields of materials research and show promising industrial applications, more efforts are needed to realize their commercialization. Firstly, the extraordinary properties of graphene are extraordinary but closely tied to the high crystallinity of the covalent sp^2 lattice. In other words, if the surface chemistry is modified by introducing covalent bond, the delocalized electrons in the p_z state must be used for bonding by forming a hybrid sp^3 orbital. As a result, the record-breaking

tensile strength and thermal conductivity of graphene are only representative for controlled systems in which graphene is a monolayer and suspended. Similarly, the electric conductivity relies heavily on the delocalized electrons. Introducing dopants or adjacent graphene layers will perturb electron conductivity by reducing charge carrier density and mean free path[14]. In short, these stringent conditions make graphene a challenging material to engineer.

Synthesis of graphene

Another challenge in industrial application of graphene lies in its large-scale synthesis. In nature, graphene is abundant, but it only exists in graphite with ordered structures. Van der Waals forces between individual graphene layers in graphite maintains the structure, but also makes it difficult to completely isolate single layers from graphite. Although the structure of graphite has been known for some time, graphene was only isolated for the first time by Novoselov and Geim in 2004[1]. Their simple method involved mechanically exfoliating graphene from graphite by using transparent tape. With enough exfoliations, a single layer could be obtained. However, mechanically exfoliated graphite exhibits the best performance, but it is hardly to be used for practical applications due to low yield; however, it is the best choice in research to create small yet pristine layers of graphene.

Despite its simplicity, mechanical exfoliation is not viable for use at industrial scale. More scalable processes such as electrochemical exfoliation rely on good dispersion in affordable solvents, such as Dimethylformamide. Since graphene is hydrophobic, exfoliated graphene layers in water will be poorly dispersed and aggregate over time[15]. Combined with poor processing for monolayers, this is one of the main challenges in commercializing graphene. Pure, monolayer graphene can only be obtained with limited methods, few of which are sufficiently fast for high throughput. One of the most widely used methods for synthesizing pristine monolayers is chemical vapor deposition (CVD) that needs a precursor gas, like methane or ethane, to grow graphene on a copper substrate as both catalysis and substrate[16],[17].

As shown in figure 2, the synthesis of single layer graphene via CVD method is performed at high temperatures and the gas decomposes and diffuses into copper. Carbonaceous compounds have low solubility in copper[18], which forces carbon to nucleate at the Cu surface. The carbon atoms then bond with one another since this is energetically favorable, rather than remaining dissociated. Once a monoatomic layer of desirable size has been synthesized, the graphene can be transferred by etching away the copper substrate. Other techniques for example ??? are variations of this methodology – constructing single layers by assembly of precursors on a molecular scale.

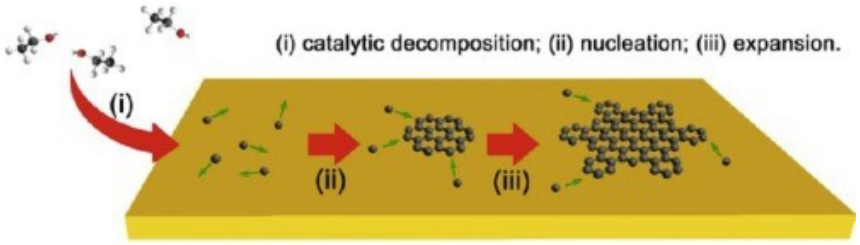

Figure 2: *Schematic illustration of the CVD process for synthesizing monolayer graphene on copper, showing catalytic decomposition and adsorption (i), nucleation (ii) and lateral growth (iii). Reused from Chen et al.[16] with permission.*

Graphene oxide and its properties

While graphene have great potential in industrial applications, its stringent fabrication requirements and low throughput are challenges that need to be solved. [19]. As an alternative to perfect graphene, GO has garnered attention due to its scalable synthesis in solution, and its combination of rich surface chemistry and potential as an inexpensive precursor for graphene synthesis.

As the nomenclature implies, graphene and GO are structurally similar. However, whereas graphene is chemically inert and solely composed of hybrid sp^2 orbitals, the GO monolayer contains a substantial amount of hybrid sp^3 orbitals bound to oxygenated functional groups. GO is a derivative of graphene as illustrated in figure 3, on the surface and edges of GO, there are hydroxide (-OH), carboxyl (-COOH), carbonyl (-CO) and even epoxide groups (-O-). Carboxyl groups are confined to edges on the GO layer, while hydroxides can exist both on edges and bonded to the layer's sp^3 hybrid orbitals. Bridging epoxide groups also exist and are confined to the lateral faces. The exact chemical composition and oxidation states vary depending on synthesis method.

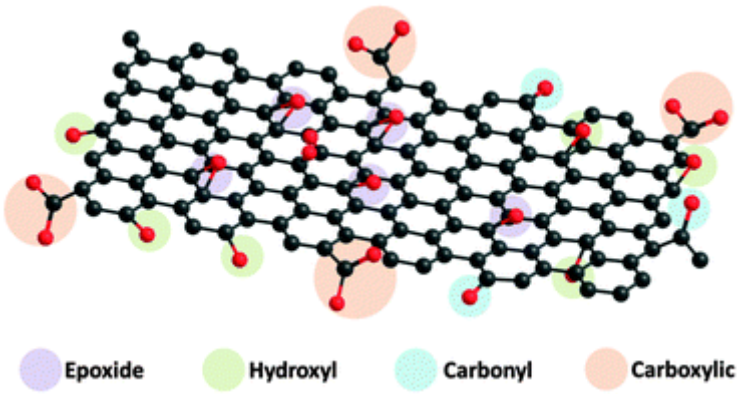

Figure 3: *Molecular structure of GO. Adapted from Chua et al.[20] with permission.*

Addition of these polar functional groups to a graphene monolayer significantly alters its properties. In terms of tensile strength, GO is considerably weaker than graphene since the layer mostly contains single σ-bonds. In fact, the Young's modulus of GO is reported to be in the range 207.6 ± 23.4 GPa[21], which is an order of magnitude lower than graphene. If fully oxidized, the structure entirely consists of hybrid sp^3 orbitals formed by bonding the previously delocalized electrons in p_z. In this case, fully oxidized graphene has completely transitioned from being a semimetal with no bandgap $E_g = 0$ eV, into an insulator with $E_g > 0$ eV. This is also reflected in the electrical resistance[22], which increases to $1.64*10^4$ Ω.

Figure 4 depicts the electronic band structures of graphene and GO. At six discrete points in momentum space, the valence band (VB) and conduction band (CB) in graphene are conical and intersect at the Dirac point. Not only is the bandgap zero at this point, but fermion charge carriers such as holes and electrons are considered massless. Introducing functional groups to graphene breaks down this quantum mechanical property by creating a band gap. However, the exact band gap of GO varies and is heavily affected by number of functional groups.

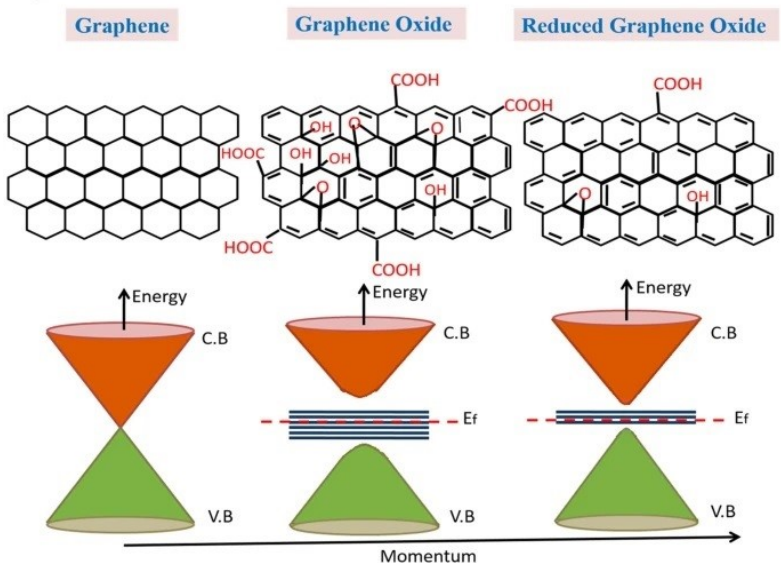

Figure 4: *Electronic band structure of graphene, GO and reduced GO. Adapted from Sehrawat et al.[23] under the Creative Commons license.*

Introducing functional groups to graphene not only deteriorates its electrical conductivity, but also its thermal conductivity in the lateral plane. In fact, the thermal conductivity in fully oxygenated GO is reported to be only 0.5-1 W/mK at room temperature[24]. This reduction in thermal conductivity owes to the increased disorder in structure, caused by an increase in possible vibrational modes by transitioning from sp^2 to sp^3 bonding. In addition to disorder caused by functional groups, GO synthesis is quite aggressive and tends to introduce defects either by incorporating adatoms or cleaving lateral bonds, creating vacancies in the lattice.

Synthesis of GO and reduced GO

While "bottom-up" methods like CVD are the only viable means for obtaining pristine monolayer graphene without impurities, the synthesis of GO is both more flexible and scalable. The "top-down" was used to synthesize GO from graphite. The current standard for top-down synthesis of GO is often attributed to Hummers and Offeman[25], who improved existing methods involving strong oxidation of graphite to yield GO. Most commercially available GO is produced with this method.

The principles behind Hummers' method is illustrated in Figure 5. First, a carbon source such as graphite ore is immersed in a protonated solvent with a strong oxidizing agent and $NaNO_3$, which catalyzes the reaction. Commonly, the agent is $KMnO_4$ and the solvent is a strong acid such as H_2SO_4. Oxidizing the graphite causes it to expand significantly, thus increasing the interlayer spacing and diminishing van der Waals interactions. This causes the graphite oxide to delaminate into flakes, which can then be treated with dilute HCl or H_2O_2 to remove metal contaminants. Intense stirring is often involved to delaminate the GO layers. The resultant powder can then be further rinsed with water until the pH of solution reaches 5-6 before sonication to further exfoliate graphite oxide into GO.

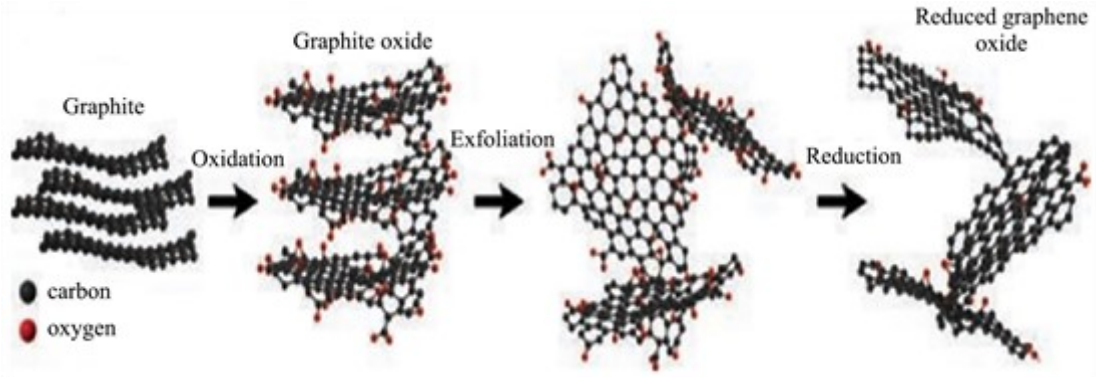

Figure 5: *Illustration of Hummer's method for obtaining rGO. Adapted from Amieva et al.[26] under the Creative Commons license.*

Although it is a standard method for synthesizing GO, Hummers' method has its limitations. One issue that prevents industrial scalability is its production of toxic NOx gases via catalysis reactions. For this reason, researchers aim to improve the method by eliminating use of $NaNO_3$. Improved versions[27] often use alternatives such as H_3PO_4 or $S_2O_8^{2-}$. Another limitation is that the quality of GO obtained from Hummers' method is affected by both the quality of raw graphite and process control. The lateral sheet size is usually smaller than the original graphite due to elastic strain introduced by addition of oxygen groups and shearing forces from intense stirring. However, results reported by Zhang et al.[28] show that foregoing mechanical agitation in favor of a stationary Hummers' method can produce GO layers more than 100 μm long.

Removal of oxygen groups from GO and restoration of the sp^2 structure is often desirable, since this significantly improves the thermal, electrical, and mechanical properties of GO. However, although there are several approaches to reduce GO (rGO), a complete restoration of the sp^2 structure is unfeasible with most methods.

The most common methods for synthesis of rGO are either via chemical or thermal reduction of GO. For the chemical reduction method, a strong reductant is used with GO in a hydrothermal redox reaction to chemically dissociate the oxygen functional groups. In research, hydrazine (NH_2NH_2) is commonly used[29] since it is reported to be an efficient reductant, obtaining rGO with C/O ratios near 10:1 while also restoring some of the sp^2 bonding structure[30]. However, hydrazine is both costly and far from eco-friendly, which limits its potential in commercializing rGO. Consequently, many researchers are devoting their attention to finding better and more affordable alternatives. While few can match the efficacy of strong reductants like hydrazine, findings indicate that simple chemical compounds like L-ascorbic acid[31] and alanine[32] can be viable candidates.

As for thermal reduction method, it is an annealing process for bond dissociation by heating GO in an inert atmosphere. The most common approach for heating GO is by using a conventional ceramic furnace, though more advanced setups employ microwave heating[33]. Unlike chemical reduction, thermal reduction is characterized by a stepwise change in which oxygen containing species are released from the GO. In GO, there is a significant amount of water intercalated between sheets. These intercalated water molecules are the first to be released upon heating due to weak hydrogen bonding with adjacent hydroxide and epoxide groups in GO. Dehydration occurs in the 100-200 °C regime and coincides with decarboxylation of labile oxygen functional groups like hydroxide and epoxide. From 300 °C and to 500 °C, decarboxylation becomes more severe and causes significant structural defects in the sheets as more stable groups are removed in the form of CO and CO_2. Fortunately, this pyrolysis can be somewhat offset at temperatures 500 °C to 900 °C due to partial restoration of the sp^2 structure in rGO[34],[35].

GO metal composites

A metal matrix composite (MMC) is a relatively new class of material consisting of a filler component dispersed in a metal matrix. The filler material can be a metal, though due to differences in solubility and melting points they do not alloy with the matrix metal but retain their morphology. Development of MMCs has been motivated by growing demands for specialized components, especially in the automotive and aerospace industries which favor strong yet lightweight materials to reduce fuel consumption[36]–[38]. As such, specialized MMCs have become increasingly common in industry.

In this regard, graphene is interesting as a reinforcing filler material in copper. Monolayers of graphene are light with a very low density of only 1.06 g/cm^{-3}, yet possesses high Young's modulus, thermal conductivity and electric conductivity. In addition, the chemical inertness of graphene makes it a possible to combine these features with corrosion passivation[6].

However, homogeneous dispersion of graphene fillers in a copper matrix has proven difficult. Ideally, dispersed monolayers of graphene should have lateral size larger than a critical size[39] (ca. 30 μm for standard polymer composites) and be structurally stable without many defects, even after heat treatment processes used for fabricating the copper composite. If the average sheet size is below the critical size, the shear transfer loading between matrix material and filler be subpar. Currently, most commercially available graphene dispersions fabricated by graphite exfoliation have average sheet sizes an order of magnitude smaller[40].

Furthermore, for a filler to structurally reinforce the host matrix, there must be some degree of interfacial adhesion between the filler and base materials. Perfect Graphene is chemically inert and has low wettability on must surfaces, meaning that it does not readily attach to the matrix

material[41]. In addition, due to its low density, Van der Waals interaction between graphene layers and poor solubility in copper, it tends to aggregate during high temperature processes like sintering[42]. As a result, the degree of load transfer between pristine graphene and copper is lower than the inherently strong mechanical properties of graphene would suggest.

Thus, instead of introducing perfect graphene as a reinforcing filler, a more affordable alternative is to use GO. In addition to possessing higher interfacial adhesion to copper due to hydrogen bonds and van der Waals forces, GO is weakly acidic and possesses a negative surface charge due to the presence of carboxylic group. This enrichens the potential for interface chemistry on GO, either by grafting new functional groups or using the negative surface charge on Cu to improve adhesion via electrostatic interaction.

This tunable surface chemistry can facilitate the dispersion of GO within a metal matrix. Consequently, the upper and lower bounds for a copper-GO MMC's properties can be estimated by using the rule of mixtures with respect to the fraction f of graphene volume V_g and copper volume V_{Cu}, as given in equation 1.

$$f = \frac{V_g}{V_g + V_{Cu}} \qquad (1)$$

The estimation assumes a homogeneous dispersion of fillers in the matrix. In the case of elastic modulus E, the upper bound for a GO-copper composite would be $E_{c,max}$ which assumes that loading is performed parallel to the graphene sheet direction.

$$E_{c,max} = fE_g + (1-f)E_{Cu} \qquad (2)$$

If the loading is perpendicular instead, the maximum loading would be the lower bound $E_{c,min}$.

$$E_{c,min} = \left(\frac{f}{E_g} + \frac{1-f}{E_{Cu}}\right)^{-1} \qquad (3)$$

Similarly, the rule of mixtures can be used to predict the resultant upper and lower bounds for electric and thermal conductivity, either parallel or perpendicular to the GO filler. Graphene would be distributed randomly within the copper matrix, so actual values would be intermediate to the upper and lower bounds.

Chapter III - Materials and methods

This section covers the materials used in synthesizing graphene coated Cu powders, as well as the methods involved in their synthesis, characterizations and analysis.

Materials

The copper powder was purchased from Carpenter Powder Products AB under the product name UltraFine Copper-MIM CCP 3123 270M+15μm, originally sold as a high-purity powder for metal injection molding. The mesh size 270M signifies that 61 μm is the largest particle diameter with a 15μm standard deviation. The particle size distribution was included in the product data sheet and is given in Figure 6 as the cumulative sieve pass. This means that the percentages given in the figure indicate how much of the powders can pass through sieves with the given opening diameters. As illustrated in the figure, 94% of all Cu particles have a diameter smaller than 62 μm and 40.8% of particles have diameters below 31 μm.

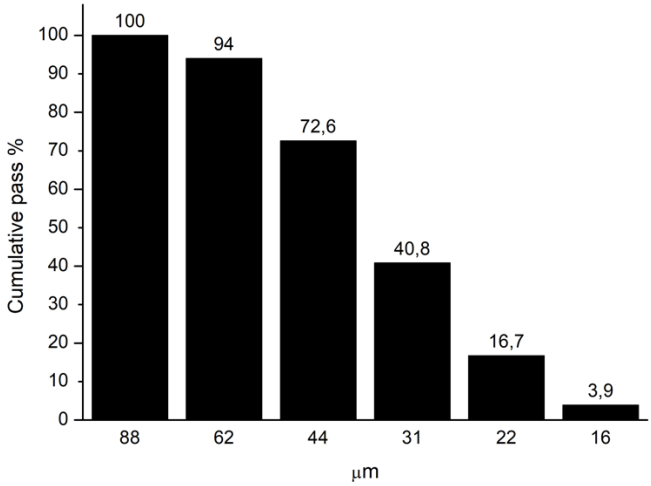

Figure 6: *The size distribution of Cu particle.*

Figure 7 shows SEM images of the pristine copper powder. Most particles are spherical, though many small particles of 5-10 μm have fused together during production. Particles with more than 50 μm diameters were irregularly shaped. The copper powder was synthesized by gas atomization.

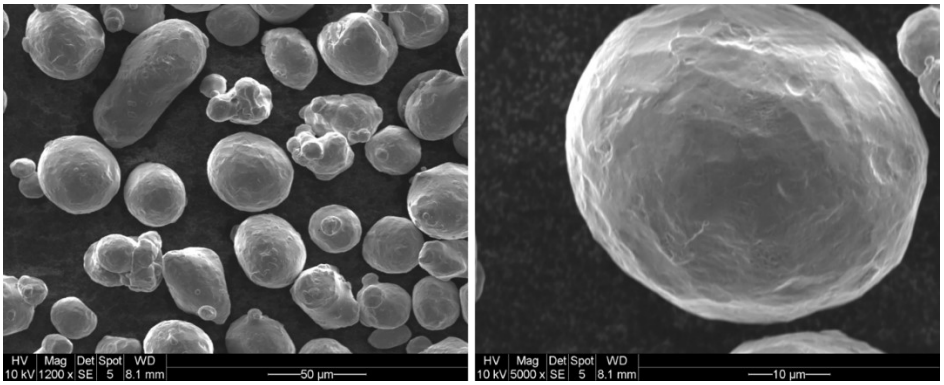

Figure 7: *SEM images of as received Cu powder particles.*

Moreover, the product certification data sheet from Carpenter gives the elemental composition of the Cu powder in wt%, as summarized in table 1 below. At the time of synthesis, only trace elements present on the powder surface were iron and oxygen, the latter in the form of surface oxides.

Table 1: Elemental composition of Cu powder in wt%.

Cu	**Fe**	**Ag**	**Sn**	**Zn**	**C**	**S**	**O**	**N**
Bal.	0.04	N/A	0.00	0.00	N/A	N/A	0.04	0.00

The GO used in this study was purchased from Graphenea. The concentration of GO suspension is 0.4 wt% in water. According to the supplier, the water suspension contains 95% monolayer GO with mean particle size less than 10 µm. GO in suspensions tend to agglomerate over time in storage due to interlayer van der Waals forces and hydrogen bonds[43]. Table 2 gives the elemental composition of purchased GO, as provided by the supplier.

Table 2: Elemental composition of GO

C	**H**	**N**	**S**	**O**
49-56%	1-2%	0-1%	2-4%	41-50%

The silane molecule, 3-aminopropyltriethoxysilane (APTES), was used to modify the surfaces of copper powders. Figure 8 shows that APTES has an amine functional group and is sensitive to moisture. In contact with water, the ethoxy functional groups can readily hydrolyze and be replaced with hydroxide groups[44]. In addition, Brønsted acids can protonate the amine group and bestow a positive charge to APTES. APTES can then form covalent bonds through condensation reactions through its hydrolyzed alkyl chains, and the protonated APTES have electrostatic interaction with negatively charged materials.

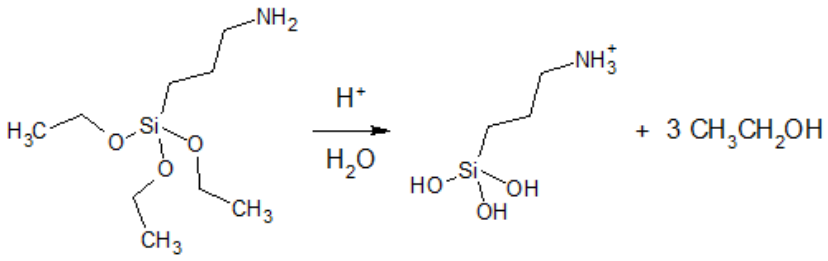

Figure 8*: Protonation of amine and hydrolysis of APTES:*

The combination of branched hydroxide chains and positively charged ammo group makes APTES a versatile surfactant molecule. Moreover, it has previously been used to surface engineer other transition metals like titanium and iron by covalently bonding to surface hydroxides[45] and oxides[44], respectively. For Cu, because of its surface oxide layer (~6nm) the APTES has the possibilities to form single, double, or triple covalent bonds with surface oxides and hydroxides via condensation reactions (Figure 9). Multiple covalent bonds on the Cu surface increases the resilience of the surfactant. Furthermore, APTES can self-polymerize to form a coherent, linked scaffold which further contributes to its structural strength[46]. If APTES has not been protolyzed in an acidic environment, the amine group will only form weak hydrogen bonds to the oxide surface. However, even in a neutral aqueous solution some amines will protonate, as will condensation reactions aggregate APTES by self-polymerization. Hence, it is necessary to limit these reactions by using non-polar, organic solvents like toluene instead.

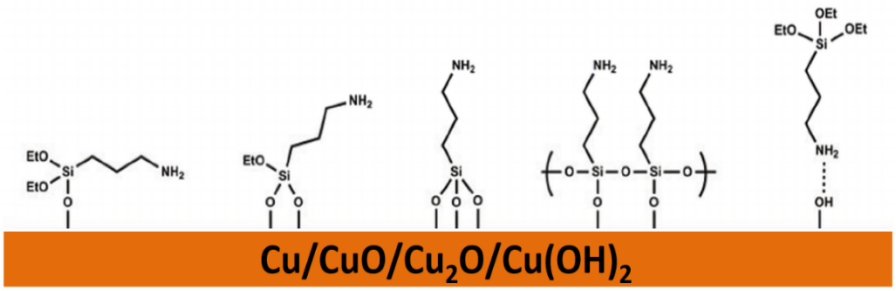

Figure 9: *Possible covalent bonds formed between hydrolyzed APTES and surfaces oxides on Cu.*

For this study, 99% APTES from Sigma Aldrich was used in 98% toluene from VWR. APTES readily deteriorates if exposed to airborne humidity and was therefore stored in sealed packages in a refrigerator.

Experimental

This section covers the synthesis methods used for most samples. The experimental procedures begin with modifying the surface of copper particles before coating with GO.

The synthesis parameters used for the samples are summarized in table 3. The amount of GO used in synthesizing each sample is given as a permille of the Cu weight. The weight of GO in grams refer to the weight of the GO dispersion before dilution.

Table 3: Synthesis parameters of CuGO samples

Amount GO	Cu	APTES	Toluene	Duration	GO (sol)	Sonication	V_{GO}	V_{Cu}
33wt‰	0.3g	6.5vol%	15mL	15h	2.5g	N/A	50mL	50mL
2wt‰	80g	0.5vol%	200mL	20h	40g	2h	1000mL	1000mL
	10g	1.0vol%	50mL	8h	5g	1h	400mL	200mL
1.66wt‰	30g	0.05vol%	150mL	8h	4.2g	3h	100mL	100mL
		0.1vol%					500mL	600mL
		0.5vol%						
		0.8vol%						
		1.5vol%						
		0.2vol%		15h			100mL	100mL
		0.5vol%						
		1.5vol%						
1wt‰	30g	0.1vol%	150mL	8h	7.5g	1h	600mL	200mL
		0.3vol%						
		0.5vol%						
		0.8vol%						
		1.5vol%						
	10g	0.2vol%	25mL	30 min	2.5g	15 min	25 mL	25mL
	500g	2.5vol%	500mL	15H	75.4g	10 min	500mL	500mL
0.25wt‰	100g	0.2vol%	250mL	30 min	5g	15 min	250mL	250mL

Surface modification of copper powder with APTES

In this study, the copper powder manufactured by Carpenter was modified with APTES in toluene.

Copper was rinsed once with toluene before suspension in a toluene in borosilicate glass jars, followed by addition of 0.1vol%-2.5vol% APTES depending on the target thickness. The volume percentage of APTES was calculated based on the toluene volume. The solutions were sealed and mixing time varied between 30 minutes to 20 hours.

Cu-APTES was subsequently rinsed three times with new toluene before drying in air at 40 °C.

Coating Cu-APTES powder with GO

Dry Cu-APTES was suspended in distilled water before addition of sonicated GO of various concentrations. Sonication time ranged between 10 minutes to 3 hours, whereas the wt‰ of GO relative to Cu ranged from 0.25wt‰ to 2wt‰.

Cu-APTES and GO mixed for 1 minute before disposal of the leftover solution. Resultant CuGO powder was gently rinsed with water before drying overnight in air at room temperature.

After synthesis, CuGO was either characterized by SEM or further processed. Some samples were weighted and corroded in etching solutions of 10vol% acetic acid or 0.5M ammonium persulfate (APS). Other were thermally reduced in a ceramic furnace.

Compaction and sintering

CuGO powders were compacted by a hydraulic, uniaxial die press at pressures ranging from 0.625 GPa to 1.875 GPa. This produced green bodies of CuGO, i.e. compacted samples consisting of loosely bound particles. The green bodies and sintered composites detailed in this thesis were all compacted at 1.25 GPa. The dies were cylindrical, yielding compacted green bodies shaped like discuses with dimensions 1cm x 0.15cm. Compacted samples detailed in this thesis were fabricated using 1g CuGO or Cu powder.

Compacted green bodies were then extracted and analyzed with Raman or sintered in a ceramic mullite furnace for 4 hours at 1050 °C under Ar atmosphere. The heating rate was 5 °C/min. The gas flow rate was maintained at 8 SCCM for the duration of the sintering, and samples were extracted after the measured furnace temperature had reduced to 80 °C.

Some sintered samples were fractured for fracture surface characterization. Such samples were clamped in a vice and fractured with impact force by a conventional hammer.

Thermal reduction of CuGO power

Thermal reduction of CuGO powder was performed in the same ceramic furnace with 5 °C/min heating rate, Ar atmosphere and 8 cm^3/s gas flow rate. The target temperature was 400 °C with 2 hours holding time. Like for the sintering, the reduced CuGO powder was extracted after furnace temperature had diminished to 80 °C.

Corrosion measurements

Besides polarization, which is mentioned in detail in a later section, the passivating effect bestowed by GO and rGO were also assessed by static corrosion in etchant solutions, acetic acid, HCl solution and APS solution.

The first measurements were performed on 0.3 g of Cu and CuGO samples in vials of 5 mL 10% acetic acid. The duration was set to 2.5 hours, and the vials were gently shaken every 30 minutes. After etching the etched powders were rinsed with DI water 3 times and dried at 40 °C under vacuum for 3 hours.

Similarly, the experiment was repeated with 0.3g Cu and CuGO powders in 10mL 10 vol% acetic acid for 7 days. This time, the vials were not shaken intermittently. After 7 days the powders were rinsed 3 times with DI water and dried at 40 °C for 3 hours.

The last etching experiment performed with 2g Cu and CuGO powders were done in vials with 0.5 M 10 mL APS solutions. The etching duration was 5 hours and samples were gently shaken hourly. After etching, the samples were rinsed with DI water 5 times and dried at 40 °C for 3 hours.

The sintered Cu and CuGO with the weight ~0.3g were etched in 250 mL 37% HCl for ~300 hours. These samples were gently shaken once a day, between weightings. Before weighting, the corroded samples were rinsed 3 times in DI water and gently dried with compressed air.

The weightings were repeated until the samples had decomposed to the point of disintegrating in the HCl solution.

Surface characterization

Scanning electron microscopy (SEM)
SEM is the workhorse of high-magnification microscopy and characterization.

As the name implies, a SEM is a microscope that produces images of an object by raster-scanning it with electrons[47]. These electrons are emitted from a high-voltage electron gun operating at 1kV-20kV and focused into a beam by several condenser lenses. These lenses are in fact toroidal magnetic fields, the shapes of which can be controlled to correct for astigmatism and focus the electron beam.

While an optical microscope would produce an image by concentrating photons reflected from the surface of an object, the SEM operates a little differently. In a SEM, the emitted electron beam interacts with the objects surface, resulting in several signals which can provide various information about the sample.

Secondary electrons (SE) are produced when the primary radiation, e.g. the incident electron beam, ionizes atoms on the surface of sample. In the main imaging mode, these SE are detected by raster-scanning to construct images. As such, SE signals can provide crucial information about the surface topography of samples.

Alternatively, another imaging mode can be use that relies on backscattered electrons (BSE). In this mode, electrons emitted from the electron gun penetrate deeper into the sample and scatter elastically. These elastically scattered electrons are then detected to construct an image. Since the scattering centers are atomic nuclei, the probability of elastic scattering increases with element mass. Consequently, BSE can be used to qualitatively characterize a sample's elemental composition by contrast. Heavy elements scatter more efficiently and appear brighter than light elements.

Inelastic scattering also occurs at deeper penetration depths. When emitted electrons scatter inelastically, they transfer some of their kinetic energy to electrons in the sample. These excited electrons briefly exist at a higher energy state before reverting to their ground state, thus releasing x-rays in the process. These x-rays are used to obtain information of a sample's elemental composition in energy dispersive spectrometry, which is covered more in detail in a later section.

For our inspections, we mainly used a JEOL 7800F Prime operating with 5kV accelerating voltage.

Raman
In Raman spectrometry, a monochromatic laser (e.g., 532 nm) is used to stimulate vibrational modes in molecules. The amount and characteristics of vibrational modes present in a sample depends on the types of covalent bonds present, as well as the mass of the bonding atoms.[48]

The mechanism involves an incident laser that excites valence electrons in the sample to higher, virtual energy states, e.g. very short-lived energy states that quickly revert to their ground states, releasing radiation in the process. Most of the radiation scatters elastically, meaning that

the emitted photons have the same energy as the incident photons, which is known as Rayleigh scattering.

However, a small subset of the emitted radiation consists of photons with slightly less or more energy than the incident photon. This is the definition of Raman scattering, and the energy discrepancy is indicative of the vibrational and rotational states in the molecule.[49]

The vibrational modes in graphitic materials are represented by the D and G bands, whose vibrations resonate at the ~1350 cm^{-1} and ~1580 cm^{-1} wavenumber, respectively. In pure graphene or graphite, an additional 2D vibrational mode exists at ~2700 cm^{-1} which represents vibration modes between multiple layers[50],[51]. Since graphitic materials have simple structures consisting of planar sp^2 and tetragonal sp^3 orbitals, the available vibration modes are limited and characteristic. In graphite, graphene and GO, the G band corresponds to the planar stretching of C-C bonds in sp^2 orbitals. In other words, high intensity for the G band indicates high purity and low defect density. Conversely, the D band arises due to presence of sp^3 bonding orbitals in the planar sp^2 lattice. In GO, these sp^3 bonding orbitals are caused by oxygen-containing functional groups like hydroxides, or even adatom impurities bonding to the layer. In addition, structural defects like vacancies and dangling bonds contribute to the D band. Consequently, the D band intensity gives a measure of oxygen content and the defects in GO and the chemical purity of graphene. For this reason, pristine graphene has ideally no D band and the quality of rGO is often represented by an intensity ratio $\frac{I_D}{I_G}$, where I_D is the intensity of the D band and I_G is the intensity of the G band in the sample.[52]

The instruments used for this type of analysis in the present study were a WITec alpha300 R Raman spectrometer, coupled with a 532 nm Nd:YAG (Yttrium-Arsenide-Gallium) laser. Primarily, the Raman spectrometry was used to confirm the presence of GO on Cu powders and within sintered samples. This was done both by point analysis. Raman mapping was also measured on the green sample to characterize the distribution of graphene.

Elemental analysis

X-ray photoelectron spectrometry (XPS)

XPS is a valuable tool for chemical analysis to determine the composition, covalent bonds, and oxidation states of materials. It is a surface analysis method that employs monochromatic X-ray irradiance under high vacuum to eject electrons from a sample.[53] These photoelectrons possess kinetic energy that is characteristic to covalent bonding states, and the photoelectrons are only generated within 10 nm of the surface. In other words, once detected these photoelectrons can provide crucial information of the chemical states on the sample's surface, in particular the binding energy E_b as calculated from the simple equation below.

$$E_b = hv - E_k \qquad (4)$$

Here, E_k is the kinetic energy of emitted photoelectrons whereas $h = 4{,}135667696 * 10^{-15} eVs^{-1}$ is the Planck constant and v is the frequency of an incident X-ray. Together, hv constitutes the energy of said X-ray.

The binding energy E_b is characteristic to each type of covalent bond and will be influenced by the oxidation state of the bonding atoms. This influence yield small variations in the binding

energy, which in turn can give a complete understanding of which bonding modes are present. For example, in a C-OH bond the binding energy is 286,5 eV while in a C=O bond it is 288 eV. In the first case, copper has an oxidation state I and in the second case it is II.

This sensitivity to oxidation states makes XPS a powerful method for elemental analysis, especially concerning carbonic compounds.[54]

The XPS analysis detailed in this study was performed on a PHI 5000 VersaProbe III Scanning XPS Microprobe. The X-ray source was monochromated $Al\ K_a$ with emission energy 1486.6 eV. The XPS analysis was used to inspect surface-modified Cu powders and evaluate the bonding modes between Cu-APTES and APTES-GO. These powdered samples were mounted on carbon tape. Cross sections of press-and-sintered samples were also analyzed with XPS. In both cases, the X-ray beam diameter was 0.1mm.

Energy dispersive spectrometry (EDS)

Energy dispersive spectrometry (EDX) is a qualitative elemental analysis method that is often done in conjunction with SEM. It utilizes an electron beam emitted from an electron gun, typically from the same gun as in the SEM, to promote valence electrons in a sample's surface to higher energy states. The lifetime of such higher energy states before the excited electrons will revert to their base energy states. This relaxation releases X-ray radiation which is characteristic to the element. Although it quickly provides information about the surface's elemental composition, it is only qualitative in nature and no additional information, such as bonding states, can be discerned. However, it can be used with SEM to create elemental mappings, which qualitatively describes how known compounds distribute or aggregate.

Laser flash analysis (LFA)

The laser flash technique is a widely used method for measuring the thermal diffusivity and thermal conductivity of a sample. As the name implies, the concept of the method is to flash a controlled laser pulse at a thin sample's surface and then measure the developing temperature increase on the other side of the sample. The higher the thermal diffusivity of the sample, the faster the heat will diffuse to the detector side[55]. For simplicity's sake, this often requires that the sample is machined into a specific shape to fit into a sample holder and distribute heat evenly. As illustrated in figure 10 below, the most common shape is a small disk or coin.

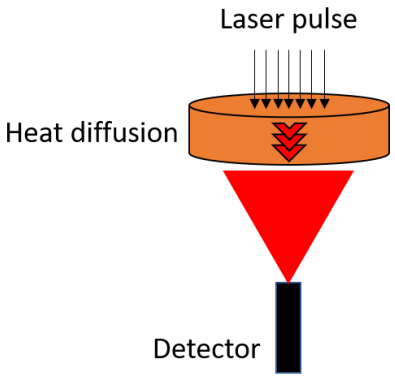

Figure 10: *The LFA method.*

In a well-controlled setup, the system is adiabatic, meaning that no heat is transferred to the sample from the outside nor expelled as waste. In this case, the thermal diffusivity a [cm^2/s] can be calculated from the following formula.

$$a = 0.1388\frac{d^2}{t_{1/2}} \qquad (5)$$

Here, d [cm] is the sample thickness in cm and $t_{1/2}$[s] is the half-life of the highest measured diffusivity. It should be noted that one requirement for using the LFA method is to coat the sample surface with a micrometer thick layer of graphite to ensure good laser absorptivity. If the original sample is too thin, the graphite's thermal diffusivity will dominate. This is only a problem for samples of thickness less than 10 μm. Once a is found, it can be used to calculate the thermal conductivity k[W/mK] of the same sample with the following equation[56].

$$k = a(T) * C_p(T) * \rho(T) \qquad (6)$$

Here, C_p[J/kgK] is the specific heat capacity of the sample at constant pressure and ρ [kg/m^3] is its density. As implied in the equation, these properties are temperature dependent. For most materials, both their heat capacity and density will increase with temperature, albeit not significantly within a few hundred degrees Celsius.

In this work, a Netzsch LFA447 was the LFA instrument of choice. For the sake of simplicity, C_p, a and ρ were assumed constant during the LFA measurement. The Archimedes method was used to measure ρ for the samples and C_p was the heat capacity of copper. The specific heat capacity of the sample would be influenced by the inclusion of GO, though it was assumed that the heat capacity of the copper matrix would dominate. In other words, the calculated k relied solely on measured a and would be compared against pure copper. The influence of graphite on the samples' thermal conductivity was negligible, since all samples had millimeter scale thickness.

Hardness testing

Hardness tests are a standard measurement within materials engineering which gives information about a material's hardness and resistance to plastic deformation. To date, there are several types of hardness testing methods, but they all follow the same principles involving indenting a sample material with a geometric shape. The first hardness test was invented by the Swedish engineer Johan August Brinell in 1900 and utilized a small, mounted sphere to indent the test piece with a known force. The material's hardness could then be calculated by correlating the indentations diameter with the applied force.[57]

While the Brinell hardness test is still used in materials engineering, one of its main drawbacks lie in the dimensions of the indenter. A spherical indenter would often require a large force to deform the test-piece, frequently resulting in microfractures and larger cracks if the material was too brittle. As such, it has largely been replaced with the Vickers hardness test method

which can be used for all metals and has a much wider range of hardness values. Instead of using a spherical indenter, the Vickers hardness test uses a pyramidal diamond indenter[58]. This makes it easier to calculate the hardness from the indentation.

The Vickers hardness, given as HV, can be calculated with the following formula:

$$HV = \frac{2F \sin(\frac{136}{2})}{d^2} \quad (7)$$

Here, F is the applied force in kilogram-force, d is the arithmetic mean of indentation diagonals and the angle 136° corresponds to the angle between the indenter's two opposite faces. Since this angle is constant, the equation can be simplified[59].

$$HV = 1.854 \frac{F}{d^2} \quad (8)$$

In this study, Vickers hardness measurements were performed on sintered Cu and sintered Cu-composite with a Struers DuraScan-70 to investigate whether graphene in the latter case would increase mechanical toughness. Due to the relative softness of sintered copper the measurements were performed with $F = 1$ kgf, or HV1 if given in standardized format. A mean Vickers hardness for each sample was found as an average of 5 indentations.

Four-point probe (4PP)

Resistivity is a fundamental property in a material and can be defined as the resistance against current flow, or the inverse to conductivity. As a fundamental property it is influenced by material composition and purity, but not dimensioning. The following relation, called Pouillet's law, exists between resistivity ρ [Ω/m] and resistance R [Ω].

$$R = \rho \frac{l}{A} \quad (9)$$

Consequently, the measured resistance in a specimen is proportional to resistivity and the ratio between length l [m] and cross-sectional area A [m^2].

The most facile and widely used method for measuring resistivity is the four-point probe (4PP). As illustrated in figure 5, the setup consists of four probes with a controlled current passing between the two outermost probes while the two innermost probes act as electrodes in a voltmeter[60]. The spacing d [cm] is equal between each probe.

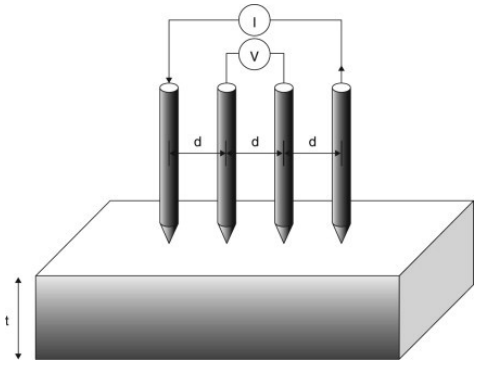

Figure 11: *Schematic of the 4PP setup. Adapted from T. Santos*[61] *with permission.*

In the ideal case, the sample to be measured is wafer-like[62] with a thickness of maximum 40% of the probe spacing d and has a surface area 40 times larger than d. In this case, the measured sheet resistance R_S can be defined with measured voltage difference ΔV and applied current I through a modification of Ohm's law:

$$R_S = \frac{\pi}{\ln(2)} \frac{\Delta V}{I} \qquad (10)$$

However, the measured R_S will increase with sample thickness t since the mean free path of electrons decreases. In other words, the thicker the sample, the more the bulk material will influence the measured resistance. To rectify this, it is possible to apply a correction factor which is provided in literature[62]. The correction factor depends on the ratio between thickness and probe spacing, e.g. $\frac{t}{d}$.

Additional rectification must be done if the sample's surface area is small, to the point when it is on the same order of magnitude as the probe spacing d. This rectification will depend on the surface geometry and for a circular surface area the correction factor C is defined by the ratio between diameter s and probe spacing d:

$$C = \frac{\ln(2)}{\ln(2) + \ln(\frac{s^2}{d^2} + 3) + \ln(\frac{s^2}{d^2} - 3)} \qquad (11)$$

In other words, if $s \gg d$ the correction factor C will approach unity.

The samples measured with 4PP in this work were compressed cylinders with diameter $s = 1$ cm and variable thickness, ranging between $0.3 < t < 0.5$ cm. The probe spacing was constant and $d = 0.2$ cm. Thus, the correction factor for circular surface area is $C = 0.742$ and the correction factor for sample thickness is between $0.72 < 0.74$. Since all samples were of comparable dimensions and only the relative variation in R_S between Cu and composites was of interest, the correction factors were not used to find the true values. The applied current was 100 mA for all samples.

Thermal characterization

Thermogravimetric analysis (TGA)
TGA is a much-used method for investigating temperature-dependent phenomena including phase transitions, thermal stability, and chemisorption or physisorption[63]. Put simply, the sample to be investigated is placed in a heat resistant crucible, typically made of alumina, and heated at a controlled rate in a certain atmosphere. Depending on the purpose of the measurement, the atmosphere can be oxidizing, inert, reducing, or reactive. In combination with other techniques such as spectrometry, TGA can be a simple yet powerful tool for analyzing a material's behavior at elevated temperatures.

For our purposes, we mainly used a NETZSCH TG 209F1 with 10°C/min heating rate up to 1000 °C in nitrogen atmosphere to investigate the thermal stability of APTES and GO on Cu. No isotherm was used.

Potentiodynamic polarization

Corrosion is a process in which electrons are released by a metal (oxidation) and received an element in the corroding solution (reduction). This electron flow can be modulated by forcing an applied potential on the system, then measured by a potentiostat in an electrochemical cell with an electrolyte. This is the principle behind potentiodynamic polarization[64], which is an inexpensive method for investigating the electrochemical kinetics of metals and alloys. It is also a standard method for checking the effectiveness of passivating coatings designed to retard or stop corrosion, as well as the pitting susceptibility of the sample.

A setup for potentiodynamic polarization consists of a counter electrode, working electrode, reference electrode and electrolyte as shown in the figure below. The electrolyte is an ionically conductive medium, most often a liquid, which emulates the environment that would corrode a sample. For most standardized corrosion tests, this would be a 3,5 wt% saline solution made with deionized water to resemble corrosion in salt water.

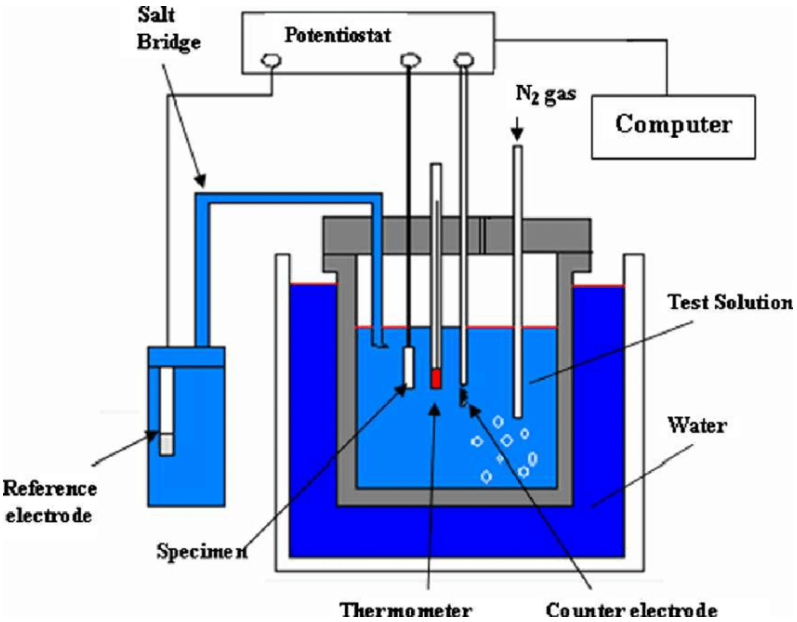

Figure 12: *Schematic of a polarization cell for potentiodynamic polarization. Adapted from Obeyesekere with permission.*[65]

The working electrode is the sample to be tested, whereas the counter electrode is connected in parallel to the working electrode and continuously measures the current via the potentiostat while running the experiment. The reference electrode, also in a parallel connection to the working electrode, transmits an applied potential from the potentiostat. In a typical potentiodynamic polarization experiment, this applied potential will change at a predefined rate, called the scan rate (mV/s). To obtain representative readings with little noise, a slow scan rate is usually preferred. In this regard, The ASTM standard scan rate is defined as 0.1667 mV/s[66]. The corrosion potential E_{Corr} is defined as the potential difference between the working electrode (sample) and the reference electrode.

Since the potentiodynamic experiment controls the potential, or driving force of a cathodic or anodic reaction, the reaction rate i.e. current density will change. At the open circuit potential (OCV), the total anodic and cathodic currents are equal. As a result, the measured or applied current will be zero.

An idealized anodic polarization scan is depicted in Figure 13, which may not be fully representative for the work presented in this thesis. Still, it serves as an illustrative demonstration. In this case, the scan starts from a low potential at point 1 and progresses towards the potential at point 2 at the defined scan rate. At point A, the rest potential or OCV ensures that the anodic and cathodic reactions on the electrode occur at equal rates. In other words, most electrons are being used to drive the reduction and oxidation reactions. As a result, there are nearly no electrons contributing to the measured current. As the applied potential increases, the oxidation reaction takes dominates. This active region, B, signifies that the reaction rate increases with applied potential up to a limit, C. The limit potential at C is also called the passivation potential, since further increasing the applied potential reduces the reaction rate via point D and into a passive regime, E. In this regime the reaction rate is largely insensitive to overpotentials, maintaining a constant oxidation rate. As the overpotential increases further, it will reach the breakaway potential at F, beyond which the oxidation reaction rate again augments as shown at G. The mechanisms governing this transgression are complex and dependent on several factors. For passivated metals or alloys in a saline solution, like stainless steel or aluminium, it may be an indicator of pitting corrosion. This mechanism is severe, as passivated areas of the sample surface would break down due to chloride and the oxidation is accelerated by a small anodic surface area, namely the pit. In other cases, if there are oxygen moieties on the sample surface, it may be a sign of electrolytic reactions producing oxygen.

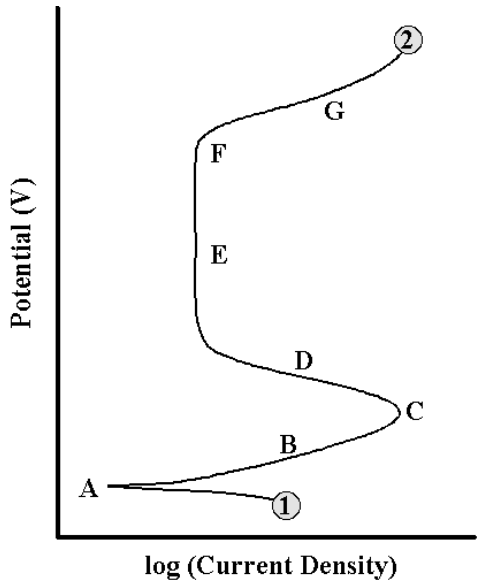

Figure 13: *An ideal anodic polarization. Reused from AMETEK Scientific Instruments*[67].

A cathodic polarization is shown in figure 14. Here, the overpotential is at first high at point 1, then moves in the negative direction towards point 2.

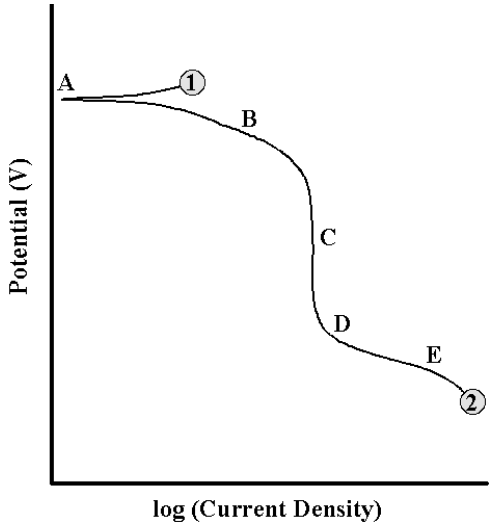

Figure 14: *An ideal cathodic polarization. Reused from AMETEK Scientific Instruments*[67].

Like before, the OCV at point A means that the reduction and oxidation occur at equal rates and the net current passing through the potentiostat is near zero. At point B the cathodic reaction takes place. Exactly which reaction takes place depends on which reductive species are present. At neutral pH and in the presence of dissolved oxygen, the following reaction dominates.

$$\frac{1}{2}O_{2(aq)} + H_2O + 2e^- \rightarrow 2OH^- \qquad (12)$$

The kinetics of this reaction is diffusion limited, meaning that the maximum current density from this cathodic reaction depends on how easily oxygen can diffuse to the electrode surface. Consequently, modifying the surface chemistry of the sample with graphene would affect this oxygen diffusion, thus reducing the corrosion rate by hindering mass transport. Alternatively, in a more acidic environment, the reduction of hydrogen is possible at higher potentials.

$$2H^+ + 2e^- \rightarrow H_{2(g)} \qquad (13)$$

Since H^+ is ionic and not a dissolved gas like O_2, it is drawn to the cathode by the overpotential. Also, due to its atomic size it is less affected by passivating coatings designed to hinder mass transport, such as graphene.

Decreasing the overpotential beyond point B will not increase the reaction rate further, since the mass transport has reached a saturation point by point C. However, if the overpotential becomes even more negative, the potential might initiate another chemical reaction which will gradually become the dominant one. This onset is shown at point D in the figure. For example, this could be reduction of water or reduction of native surface oxide on the sample.

The polarization curves in figures 13 and 14 can be expressed mathematically by the Butler-Volmer equation, given below.

$$i = i_{Corr}\left\{exp\left[\frac{a_a zF}{RT}(E - E_{Corr})\right] - exp\left[\frac{a_c zF}{RT}(E - E_{Corr})\right]\right\} \qquad (14)$$

The equation describes how the electrical current density i (A/cm^2) in a sample depends on the potential difference between the sample and the surrounding medium, i.e. electrolyte. In an electrochemical cell the reaction rate can be modulated from its exchange current density i_o(A/cm^2) by applying a potential E (V) which is different from the reactions equilibrium potential E_o. In corrosion chemistry, the exchange current density and equilibrium potential define the corrosion rate and corrosion potential at steady state, respectively, meaning that the cathodic and anodic reactions occur at equal rates. Thus, i_{Corr} and E_{Corr} are used interchangeably with i_o and E_o. Without any applied potential E, the electrical current density driving the corrosion is only influenced by the system's temperature T(K), the z number of electrons involved in the reaction and the charge transfer coefficients for the anodic and cathodic reactions. These are a_a and a_c, respectively, and have values between 0 and 1 which define the propensity for a successful charge transfer in an anodic or cathodic reaction at the electrode/electrolyte interface. These coefficients are influenced by the chemical compounds involved in the half-reactions, as well as the electrolyte. R (8.314 J/Kmol) and F (96485 C/mol) are the ideal gas constant and Faraday's constant, respectively.

If the applied potential is significantly different from equilibrium so that $|E - E_{Corr}| \gg 0$, the relatively complex Butler-Volmer equation can be simplified to the Tafel equation. It is and approximation and is only valid in the linear regimes of the Butler-Volmer equation, which typically begin ±0.1V from E_{Corr}. If this is the case and the applied potential is $E < E_{Corr}$, the first term in equation 14 dominates and the relationship simplifies to equation 15.

$$E - E_{Corr} = \beta_a \ln\left(\frac{i}{i_{Corr}}\right) \tag{15}$$

This linear equation relates the overpotential $E - E_{Corr}$ to the reaction rate of the anodic process, given as the slope β_a. Similarly, if the applied potential is $E > E_{Corr}$, the cathodic process described by the second term in equation 14 dominates, and the reaction rate is given by the slope β_c.

$$E - E_{Corr} = -\beta_c \ln\left(\frac{i}{i_{Corr}}\right) \tag{16}$$

If both reaction rates β_a and β_c have been found experimentally or fitted numerically, it is possible to estimate the corrosion current density i_{Corr} at $E = E_{Corr}$. Graphically, this is presented as the intersection of the linear equations.

In this study, an experimental setup consisted of sintered Cu or CuGO samples as the working electrode, standard Ag/AgCl refence electrode and a counter electrode. The electrolyte was 3.5 wt% 700mL saline solution made with distilled water. Measurements were carried out with 0.5mV/s scan rate and the potential range was from -0.5V to 0.2V. The potentiostat was controlled with the CorrWare software, which was also used to estimate i_{Corr} by fitting experimental data with Tafel curves. Prior to each measurement, the electrochemical cell and electrodes were rinsed with DI water, then ethanol and dried in an oven at 40 °C. The saline solution was then used to rinse the cell and electrodes before starting an OCV equilibration for 20 minutes.

Chapter IV - Results and summary of papers

This section summarizes the results obtained in this study. By modifying key parameters such as concentration of APTES surfactant, GO concentration and synthesis time, the coating thickness on Cu particles can be controlled.

The GO layer thickness influences the properties in the composite powder as well as the sintered composite.

Synthesis route for thick coatings

Initially, pure Cu powder and highly concentrated GO suspensions were mixed in solution to observe the adhesion between the two composite constituents. As confirmed in literature[41],[68], the wetting between Cu and GO is limited to Van der Waals interaction, so GO layers were visibly detaching in the first attempts at creating CuGO composites without any surfactant molecules. This motivated the use of APTES as a surfactant molecule on Cu to improve adhesion via electrostatic interaction. In an acidic solution, mediated by the carboxyl groups on GO, the amine group on APTES will readily protolyze to positively charged ammonium. This ammonium group possesses a net positive charge and can attract negative charges vicinal molecules, e.g. hydroxide and epoxide groups on GO.

Figure 15 shows 33wt‰ CuGO composite powder synthesized by mixing 6.25vol% APTES in 15 mL toluene with 0.3g Cu for 24 hours, followed by mixing with unsonicated GO in 100mL DI water. Images a), b) and c) all display different particles from the same sample batch. This early attempt proved that adhesion between Cu and GO can be significantly improved with facile, scalable methods involving electrostatic attraction between GO and the substrate. However, at this point the process was not optimized and formation of CuGO clusters was still an issue.

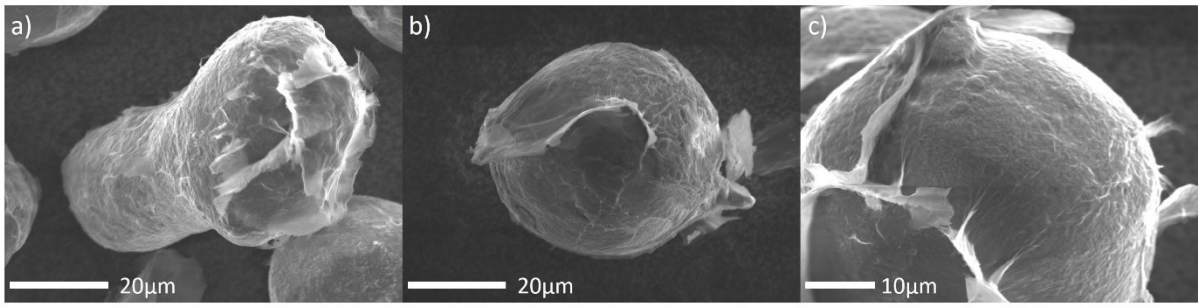

Figure. 15: *CuGO powder synthesized with 33wt‰ GO and 6.25vol% APTES for 15 hours. Each image originates from separate CuGO particles from the same sample batch.*

The next batch of samples were synthesized with better control of coating thickness and dispersion in mind. To this end, the mixing time for APTES was maintained while both GO and APTES concentration was reduced and GO was sonicated for 10 minutes. The magnetic plate was set to 60 °C to accelerate adsorption, though the actual temperature of toluene during Cu-APTES synthesis was lower since no thermocouple was inserted. Figure 16a) and b) show that this approach greatly reduced clustering of composite particles and coating thickness, while maintaining uniformity. As shown in figure c), the GO sheets were visible at 2000x magnification, revealing that this approach was sufficient for obtaining a mostly unform coating consisting of GO multilayers. Higher magnification at 50000x indicate that, while distributed evenly, the coating was still graphitic and consisted of multiple layers of GO. As an amalgamation of consecutively stacked layers, thick causes high surface roughness.

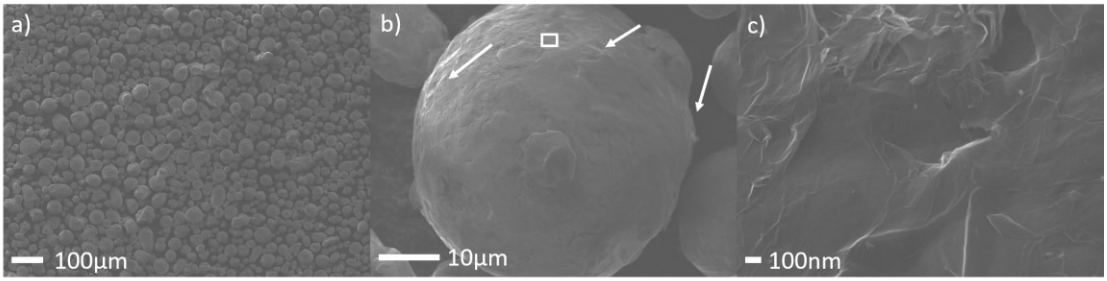

Figure. 16: *CuGO powder synthesized with 0.625wt‰ Cu:GO ratio and 2.5vol% APTES for 15 hours. The rectangular area indicated in b) contains the high magnification image c).*

Although this is just a small excerpt of the composite powder samples that were synthesized with thick GO coating, they illustrate the general process methodology for obtaining such samples. Since the reaction kinetics for formation of a monoatomic layer of APTES on CU is slow at room temperature, the synthesis of composites with thick coatings not only require higher APTES concentration but also more time for solution mixing. The adsorption of APTES can be accelerated by increasing the solution's temperature, though this increases the risk of polymerization of bonding APTES molecules.

Synthesis route for thin coatings

Synthesizing CuGO composite powders with GO coatings of controllable thickness is not only crucial for limiting GO waste, which is expensive, but also for engineering the composite's corrosion protection and thermal/electric conductivity. Furthermore, GO can readily reduce at temperatures as low as 200 °C, releasing carbonaceous gases and exfoliating layers in the process due to high interlayer pressure. Thus, synthesizing thinly coated composite powders would be beneficial to reduce pore formation from gas release and improve mechanical performance.

The main methods for reducing layer thickness were shortening APTES mixing time and lowering APTES concentration. Since the self-assembly of APTES monolayers on Cu is slow at room temperature, shortening the mixing time will reduce the amount of APTES adsorbing on the surfaces. A similar effect can be obtained by maintaining a long mixing duration while reducing the APTES concentration. A composite powder synthesized with 100g Cu, 0.2wt‰ GO and 0.2vol% APTES in 250 mL toluene is shown in figure 17. The APTES functionalization step was only maintained for 30 minutes, resulting in a uniform and thin GO coating after synthesis with no agglomeration of CuGO powders, as shown in a). Moreover, the high magnification c) of the inset area in image b) shows that the GO coating is mostly transparent and only identifiable by wrinkling of the upper GO layers, which is caused by imperfect GO layer stacking. In figure 17c), areas with wrinkling of few-layered graphene oxide are indicated by red arrows. The sonication duration was short, being only 15 minutes. This short duration resulted in GO macroparticles in suspension being visible by eye, indicating that the detachment and dispersion of GO layers was not complete. Despite this, the GO coating appeared thin and uniform throughout the powders, indicating that larger flakes had failed to adhere to the surface and remained in solution after the CuGO synthesis.

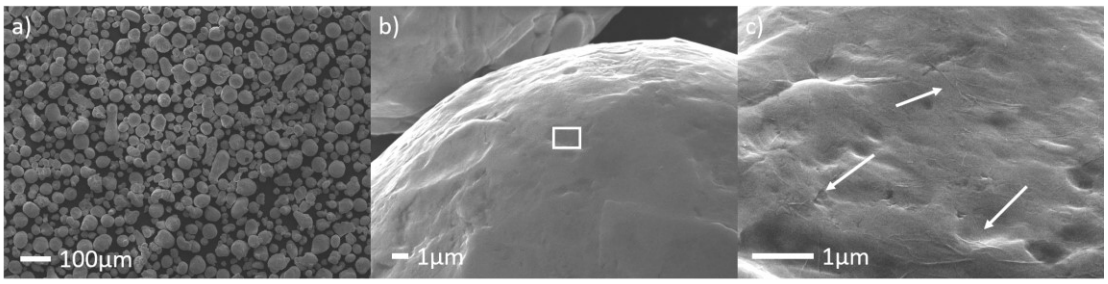

Figure 17: *CuGO powder synthesized with 0.2wt‰ GO and 0.2vol% APTES for 30 minutes.*

Repeating the synthesis procedure with identical parameters and increasing the GO concentration from 0.25wt‰ to 0.625wt‰ GO yielded similar results, as shown in figure 18. Figure 18a) shows that the increased GO concentration did not increase frequency of clusters, while b) and c) show that neither was the observable layer thickness affected, though it did increase the propensity of small 1-3 µm sized Cu-APTES particles to become enveloped in GO and stick to larger hosts. While not all GO in solution was adsorbed as a coating, that which did coat the powders was uniformly dispersed. Like for the preceding sample, the GO coating thickness was qualitatively assessed by high magnification inspection of particle surfaces. Quantitative methods like X-ray fluorospectrometer (XRF) could be used to determine coating thickness on powders, but in this study they were omitted since GO coatings were thin (10-30nm) and comprised of carbon, which is a contaminant on most metal surfaces[69]. Some preliminary measurements of GO layer thickness on Cu powders were done with X-ray diffraction (XRD), but no characteristic diffraction peaks were found for (100) and (001) between 0-10 2Θ.

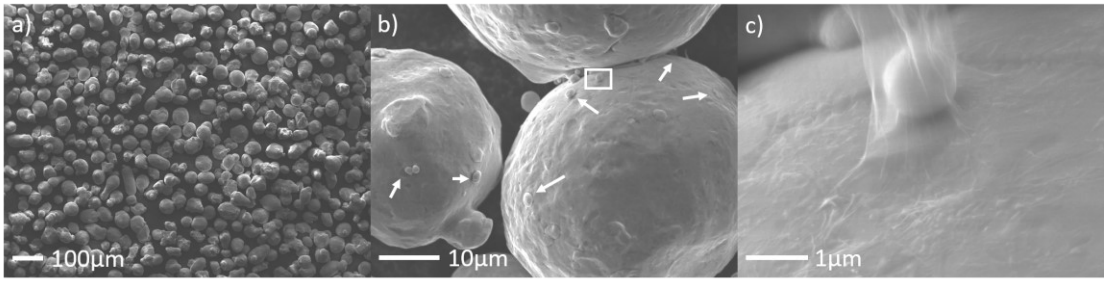

Figure 18: *CuGO powder synthesized with 0.625wt‰ GO and 0.2% APTES for 30 minutes.*

Lastly, the importance of APTES functionalization duration alone was evaluated. In this case, both the GO concentration and APTES concentration were high, at 1wt‰ and 2.5vol% APTES respectively. The synthesized batch was smaller, consisting of 10g Cu and 25mL toluene. Like before, GO was only sonicated for 15 minutes and the duration of APTES functionalization was 30 minutes. Despite the higher GO and APTES concentration, the resulting GO coating on this sample was of comparable thickness to the sample shown in figure 18. In both samples, the coating was sufficiently thin so as to not obscure the features of the Cu surface yet could be identified by GO sheets folding and wrinkling. In other words, these GO coatings did not possess enough layers to impede the 5kV SEM beam. This new sample, shown in figure 19, also did not exhibit any aggregation or attached CuGO particles. The particles in figure 19a)

exemplify this, and the image b) and inset magnification c) reveal that despite the lack of such telltale indicators of GO, very thin layers of GO encompass most of the particle surfaces-

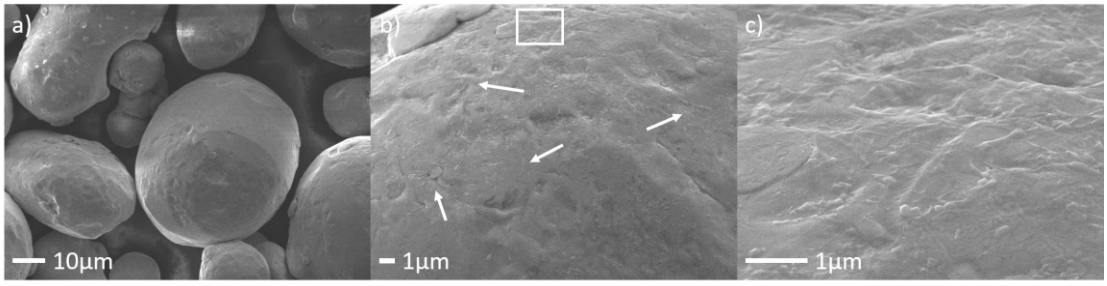

Figure 19: *CuGO powder synthesized with 1wt‰ GO ratio and 2.5% APTES for 30 minutes.*

Though these are just some examples of synthesized CuGO particles with thin adlayers of GO, the results indicate that the magnitude of electrostatic interaction between APTES and GO plays a crucial role in controlling layer thickness of GO. Reducing the amount of APTES on Cu particles, either by reducing APTES concentration or the duration of functionalization, will lower electrostatic attraction between GO and Cu-APTES on the particle's surface. Consequently, low positive surface charge on Cu-APTES favors mono- or few-layered GO sheets.

Thermal reduction

Figure 20 shows the surface of a composite CuGO particle which originates from the same sample batch as the particles in figure 16, which were synthesized with 0.625 wt‰ GO ratio and 15 hours mixing with APTES. The particle has undergone thermal reduction at 400 °C for 2 hours to remove oxygen from the GO coating, resulting in Cu-rGO. Some of the rGO coating was exofoliated in the process, revealing bare Cu . The effectiveness of the thermal reduction in argon atmosphere was evaluated by comparing C/O ratios of original GO from Graphenea against the C/O content found on synthesized powder. For this purpose, elemental EDS analysis was performed on 5 points as detailed in the figure. These points are denoted spectrum 9 to 13 in the figure.

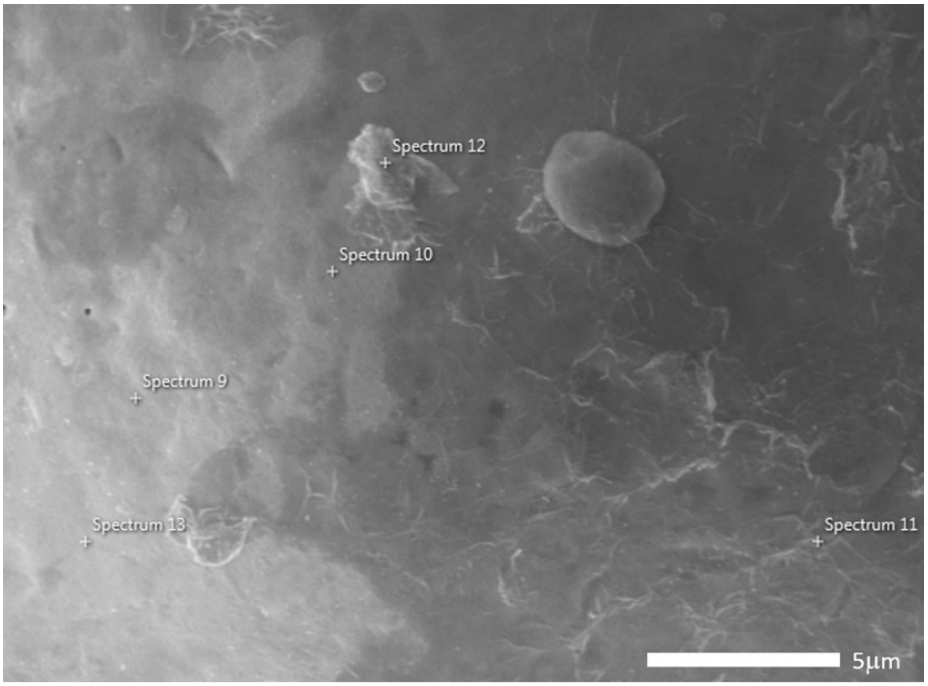

Figure 20: *CuGO composite powder after thermal reduction. The sample was synthesized with 0.625wt‰ GO and 2.5vol% APTES overnight.*

The elemental compositions of the points are given in table 3. Trace amounts of carbon and oxygen exist on the entire surface, not only on the rGO coating. On points 9, 10 and 13, which are bare Cu, the C/O ratios range from 3.6 to 9. On the other points 11 and 12, it ranges from 6.1 to 7.5, illustrating that on average the carbon content is higher in these regions. Furthermore, since the C and O signal contribution in point 11 and 12 are influenced by the substrate, the actual C/O ratio on rGO is likely lower. Compared with point 9 and 10, the Cu content in points 11 and 12 are 5.3% to 8.2% lower while the oxygen content is only slightly larger. Consequently, the main contributor to lowering the Cu intensity in point 11 and 12 would be carbon. Thus, the added carbon content from the GO coating varies between 5.3% to 8.2% and the C/O ratio in rGO would be from 5:1 to 8:1, assuming a 1% carbon content on pure Cu. In comparison, the C/O ratio in original GO from Graphenea ranges between 5:4 to 1:1. In other words, the oxygen content in GO can be effectively reduced by thermal treatment at 400 °C for 2 hours.

Table 4: Elemental composition after thermal treatment

Point	Cu	C	O	Si
Spectrum 9	90.0	9.0	1.0	N/A
Spectrum 10	89.3	8.6	2.0	N/A
Spectrum 11	81.8	15.7	2.1	0.4
Spectrum 12	84.7	12.9	2.1	0.3
Spectrum 13	91.1	7.0	1.9	N/A

Cross section of sintered samples

Sintered samples of Cu and CuGO composites were fractured to inspect the fracture morphology. Figure 21a)-d) shows the cross-section copper sintered at 1050 °C for 4 hours in argon atmosphere. The sample's density was 8.4 g/cm^3 after sintering, or 94% of max density.

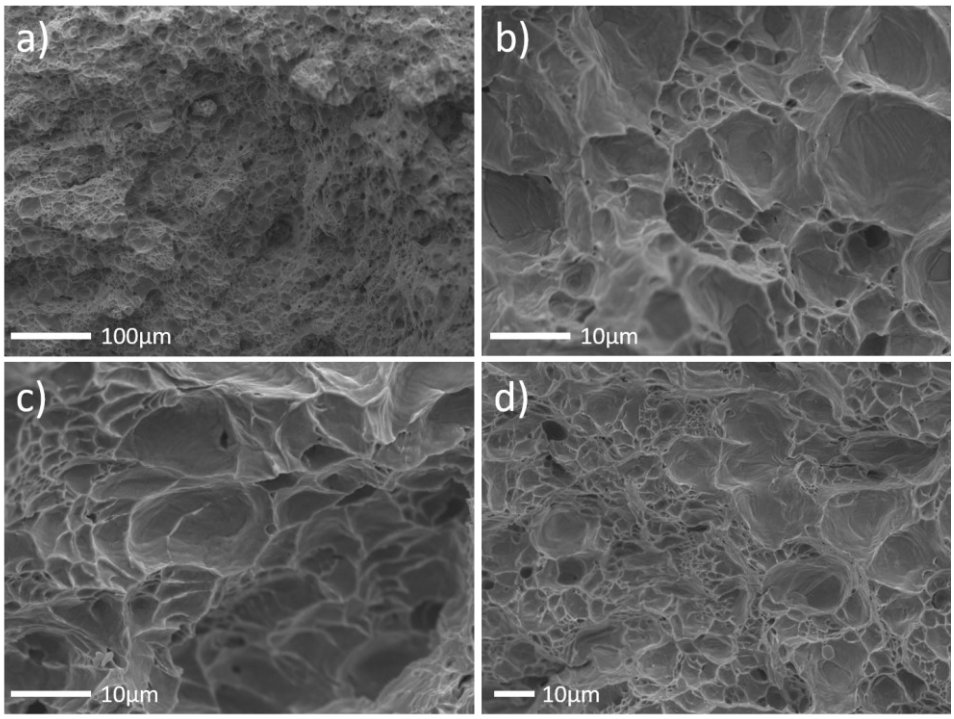

Figure 21: *Cross section of sintered Cu.*

Figure 22 depicts the fracture surface of a sintered composite of Cu-rGO, which had undergone thermal reduction at 400 °C for 2 hours in argon prior to sintering. The composite powder was synthesized with 0.625wt‰ GO ratio and 2.5vol% APTES in overnight mixing for 15 hours, and is the same powder shown in figure 16 and 20. The measured density was 8.7 g/cm^3.

Compared to sintered Cu, the internal structure of this composite contains Cu-rGO particles that have not fully fused with adjacent particles, as shown in figure 22 a). The arrows indicate internal regions with varying degrees of densification. In regions with low densification, individual Cu-rGO particles can be identified in the matrix. Conversely, regions with higher density appear more amorphous, like pristine copper. Image b) shows another example of where smooth areas or sockets are juxtaposed with both porous cavities and regions with

rougher surfaces, indicating necking with vicinal particles. Higher magnification imaging of these smooth areas, like in image c), indicate a high prevalence of rGO existing both as detached sheets and layers blanketing the sockets. In d), closer inspection of the poorly densified Cu-rGO reveal that intact rGO sheets act as bridges between multiple particles. Similarly, the upper and lower parts of the image depict areas with rGO damaged by the fracture.

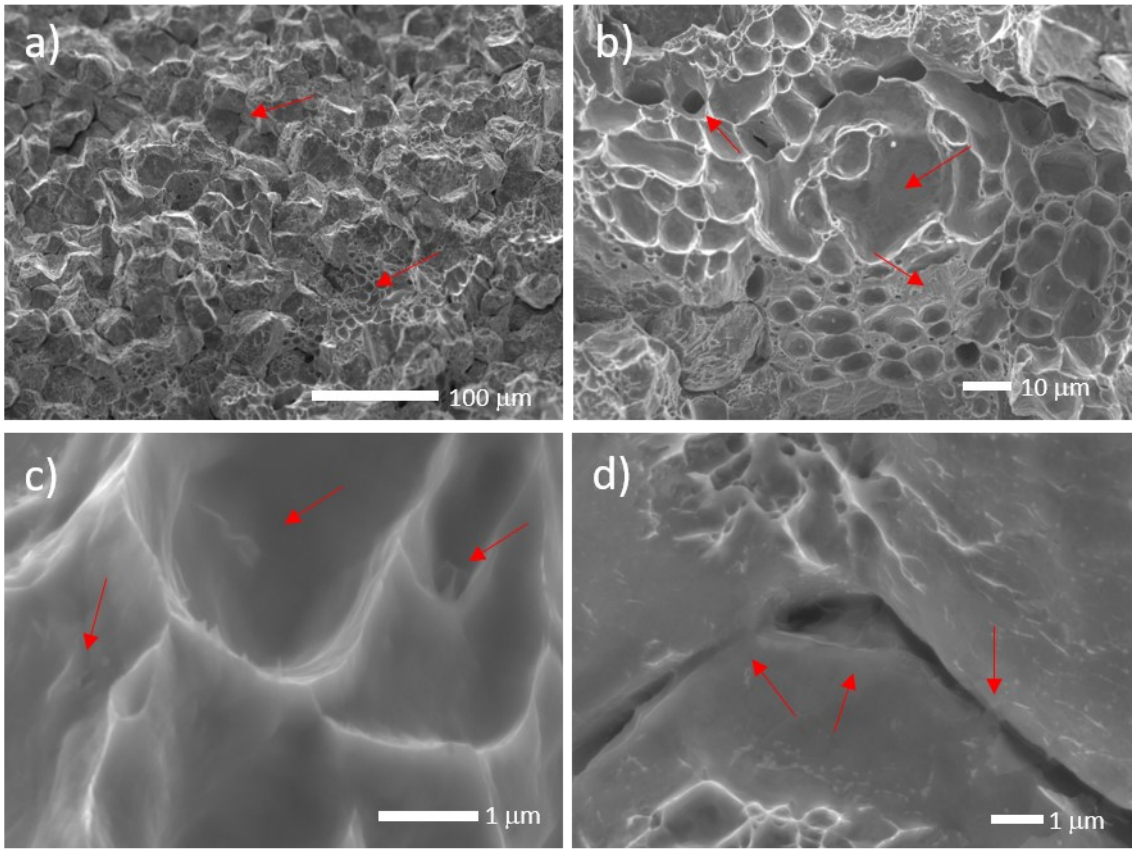

Figure 22: *Cross section of a sintered composite of thermally reduced CuGO powder. Images a) and b) are low magnification images of the fracture surface, whereas c) and d) are closer inspections of the socket structures and particle boundaries, respectively.*

The importance of oxygen removal by thermal processing is illustrated in figure 23, which depicts the cross section of a sintered composite of CuGO synthesized with 1wt‰ GO, 2.5vol% APTES and 30 minutes duration of functionalization. The CuGO composite powder was not thermally reduced to Cu-rGO before compaction and sintering at 1000 °C for 4 hours. As a result of hydroxide and epoxide decomposition due to heating, the internal structure becomes highly porous as shown in figure a) to c). It should be noted that the GO coating in this composite powder was thin due to the short duration of functionalization. In other words, even a thin coating of GO releases enough gas during heating to inhibit diffusion mechanisms between Cu particles. At high magnification, like in image d), no clear indicators trace amounts of GO sheets were found.

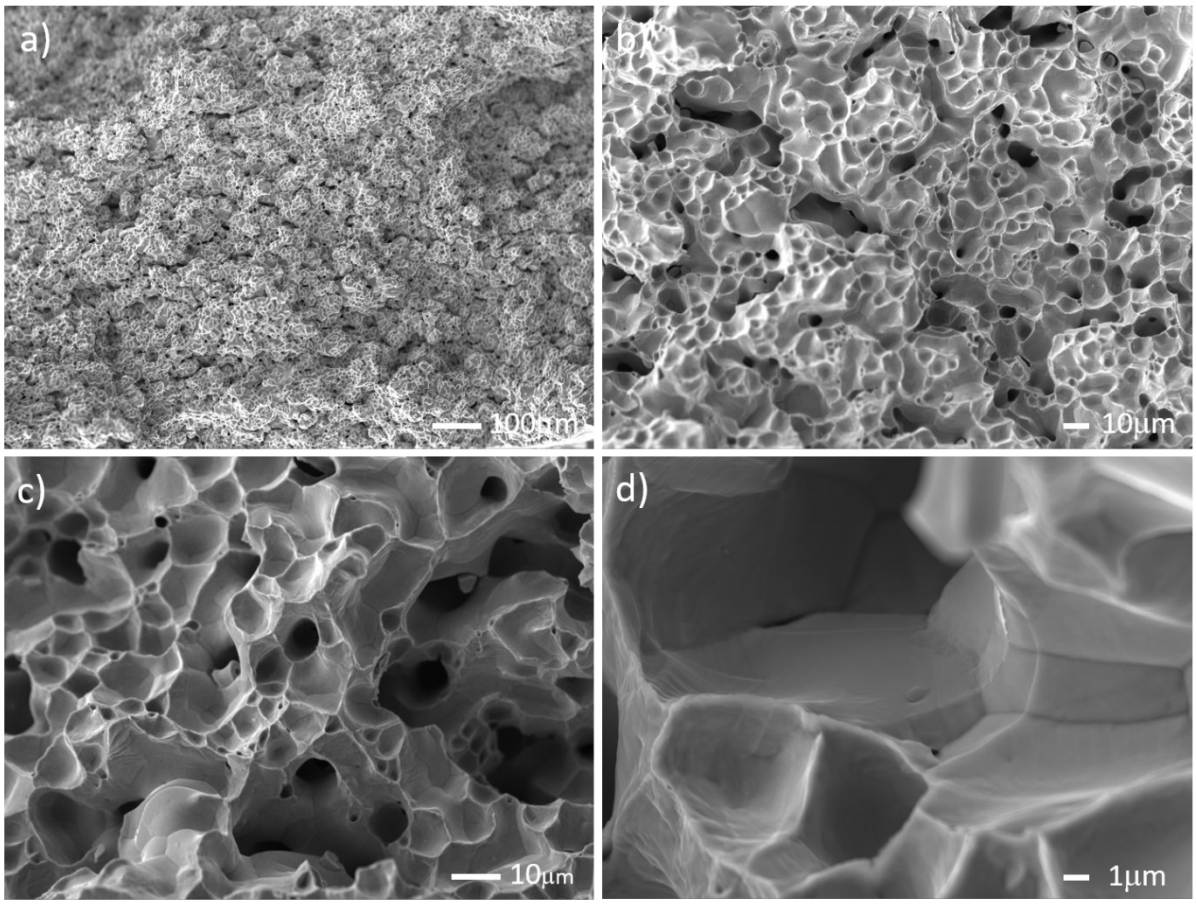

Figure 23: *Cross section of a sintered composite of CuGO powder synthesized with 1wt‰ GO ratio and 2.5vol% APTES for 30 minutes.*

Scaling GO coating thickness with APTES concentration

The results in previous sections show that the GO coating thickness can be controlled by altering synthesis variables. For batch synthesis by solution mixing, the available variables are GO concentration, APTES concentration and duration of Cu functionalization with APTES in toluene. Additional variables influencing the synthesis are solution's temperature during functionalization of Cu with APTES, as well as the pH in the GO suspension. However, currently the influence of these variables is beyond the scope of this work.

Multiple experiments were conducted to evaluate the influence of these parameters. One example is given in figure 24, which depicts 5 sample batches synthesized with identical parameters and various APTES concentrations. Specifically, they were synthesized with 1wt‰ GO, 8 hours Cu-APTES functionalization duration and 3 hours of GO sonication. The APTES concentrations were 0.1%, 0.3%, 0.5%, 0.8% and 1.5% for the samples shown in figure 24a) to 24e), respectively. Lower magnification images of the samples are not included, since no samples showed signs of clustering. In the juxtaposed images the arrows pinpoint locations with readily visible multilayer GO.

For samples synthesized with 0.1% and 0.3% APTES, shown in fig. 24a,b, thin layers of GO were only detectable under high magnification and by noticing obscured features of underlying Cu. At these low APTES concentrations it was difficult to assess the coverage of GO on particles. However, regions with clear features from Cu were frequent, indicating only a partial

coverage of GO. The degree of coverage is significantly different from the sample synthesized with 0.1% APTES and the one synthesized with 0.3%. This is demonstrated in fig. 24b), in which micron-sized particles of Cu decorate the host particle's surface and are enveloped in the GO coating, as indicated by the red arrow. From here and several micrometers to the right and below of the small particles, the features of the Cu host particle are obscured by a thin layer of GO, indicating a partial coverage of at least 5 μm.

Increasing the APTES concentration to 0.5% and 0.8% does not cause a clear increase the coverage of GO, as shown in respectively in figure 24c) and 24d). Instead the prevalence of multilayer GO seems to increase, indicating a stronger electrostatic attraction between ammonium and functional groups on GO. Specifically, while the surface area covered by GO appears to be unchanged, the number of cases of localized multilayers of GO increases. This was determined qualitatively with SEM by finding areas with increased wrinkling and higher degree of obfuscation of the Cu surface features. A clearer relationship between synthesis time, APTES concentration and GO layer thickness would be possible with Brunauer-Emmett-Teller (BET) or other quantitative inspections.

In short, SEM characterization alone is not enough to accurately assess the influence of APTES concentration on coating coverage or thickness. Since the reaction rate for APTES functionalization on Cu is slow at room temperature, 8 hours may not be sufficient to create meaningful disparity among the samples depicted in figure 24.

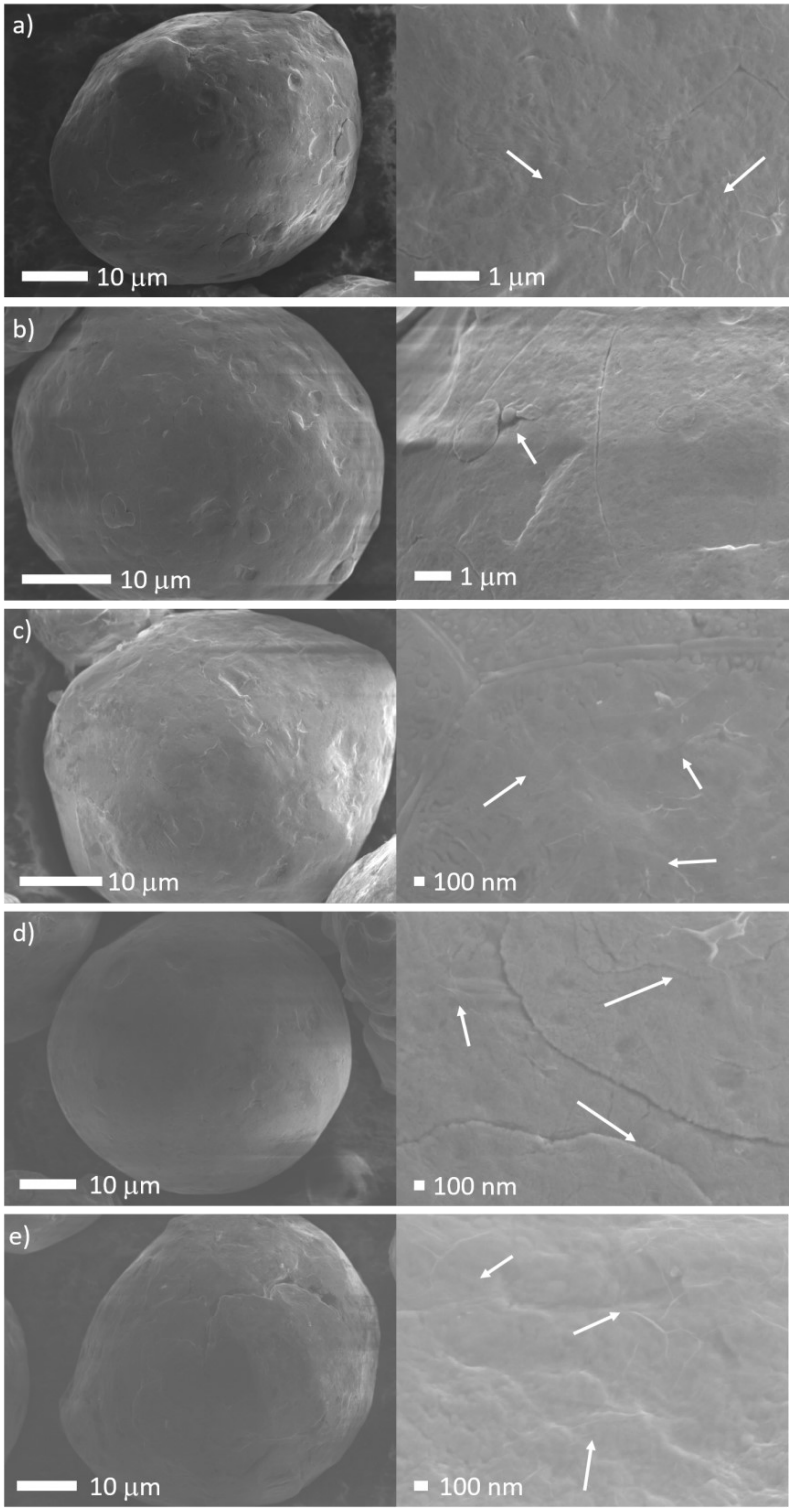

Figure 24: *CuGO composite powders synthesized with a) 0.1%, b) 0.3%, c) 0.5%, d) 0.8% and e) 1.5% APTES. Each row corresponds to one sample. The arrows point at regions with detectable GO.*

Raman

As a complement to SEM characterization, the efficacy of the synthesis method was also inspected with Raman spectrometry. The coating thickness and uniformity could be qualitatively verified by creating mappings of characteristic D and G bands in GO. Figure 25 shows the spectrum of GO on a Cu particle after filtering the background contribution from Cu. The G band from spectra such as the one in the figure were used to construct Raman intensity mappings of compacted green bodies of the samples from the previous section. These mappings are presented in figure 26.

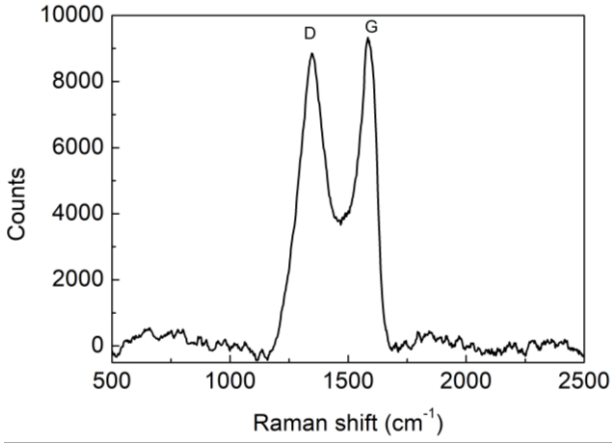

Figure 25: *Raman spectrum of GO on unsintered Cu particle.*

The optical microscopy images in figure 26a) to 26e) correspond with the Raman mapping on the same row. Even samples synthesized with low APTES concentrations, such as 0.1% and 0.3%, show appreciable G band intensities in mapping a) and b), respectively. The G band intensities increase with even higher APTES loading, as shown by progressively stronger features in images c) to e). While the G band intensity increase is substantial from 0.1% to 0.3% APTES loading, it is subtler between 0.3% to 0.8% APTES loading. Increasing the APTES loading from 0.8% to 1.5% causes the G band signal to further strengthen, nearly saturating the mapping area.

This increase in coating coverage correlates with the SEM images in figure 24, for which the sample synthesized with 1.5% APTES displayed the most uniform and widespread coverage of GO. However, the optical microscopy images (figure 26a) to 26e)) also reveal a gradual increase in graphitic graphene, shown as black spots. In other words, increasing the APTES concentration not only improves the electrostatic attraction to GO monolayers and increases coverage rate as a result, but can also be detrimental in the sense that the electrostatic attraction becomes strong enough to retain multilayer, i.e. graphitic GO.

Since all Raman mappings were performed on GO, the $\frac{I_D}{I_G}$ ratios for all five images were roughly 1.

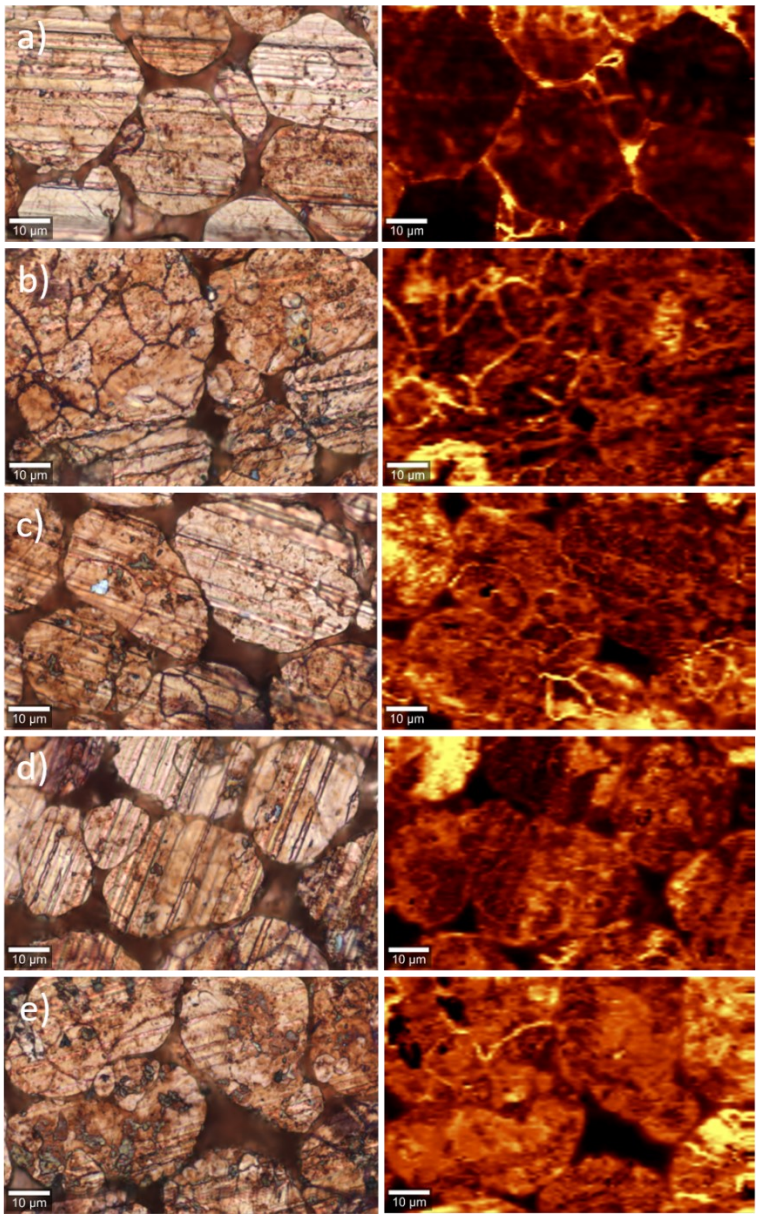

Figure 26: *Optical images (left) and Raman mapping (right) of unsintered CuGO samples. The samples were synthesized with a) 0.1%, b) 0.3%, c) 0.5%, d) 0.8% and e) 1.5% APTES for 8 hours. The scale bars represent 10µm.*

Additional Raman analysis was conducted on sintered composites to investigate the integrity and quality of graphene after heat treatment.

Figure 27 shows the optical microscope images of a cross section from a sintered Cu-rGO composite, which was fractured to investigate the retention of Cu-rGO in the composite matrix after sintering. The CuGO composite powder was synthesized with 0.25wt‰ GO, 0.1% APTES concentration and mixing for 3 hours. The reduction was carried out at 400 degrees °C for 2 hours in argon atmosphere, like for the preceding Cu-rGO samples.

A Raman mapping of the uneven fracture surface proved unfeasible, so point analysis was instead performed at individual points. The colored Raman spectra in the figure correspond to each colored point. The three spectra, taken at the fracture surfaces shown by optical

microscopy, all display significant signal intensities for D and G bands at 1350 cm^{-1} and 1580cm^{-1}. This indicates that rGO persists within the copper matrix. The red and blue spectra also show bands for CuO at 520 cm^{-1}, as well as Si from APTES at 630cm^{-1} at 1000cm^{-1}. The large bands at 50cm^{-1} to 100cm^{-1} are artefacts from the background subtraction and convolutes additional bands for CuO, which would normally be found at 290 cm^{-1} and 340 cm^{-1}.

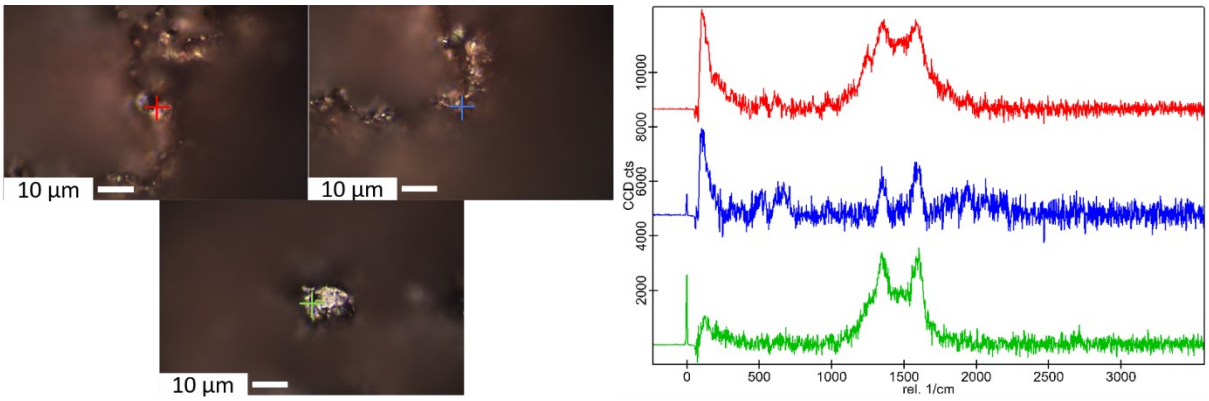

Figure 27: *Raman of cross section of sintered Cu-rGO sample synthesized with 0.25wt‰ GO, 0.1vol% APTES and 3 hours APTES functionalization duration. Each spectrum corresponds to the marker of the same color.*

As a complement to the Raman analysis, the cross section analyzed in figure 27 was characterized with SEM. Figure 28 shows the fracture surface after sintering. The surface morphology resembles Cu in figure 21 and the Cu-rGO sample in figure 22. Unlike the other Cu-rGO composite, however, this sample has lower internal porosity while retaining some visible traces of rGO. The rGO is most readily visible in pores or in their vicinity.

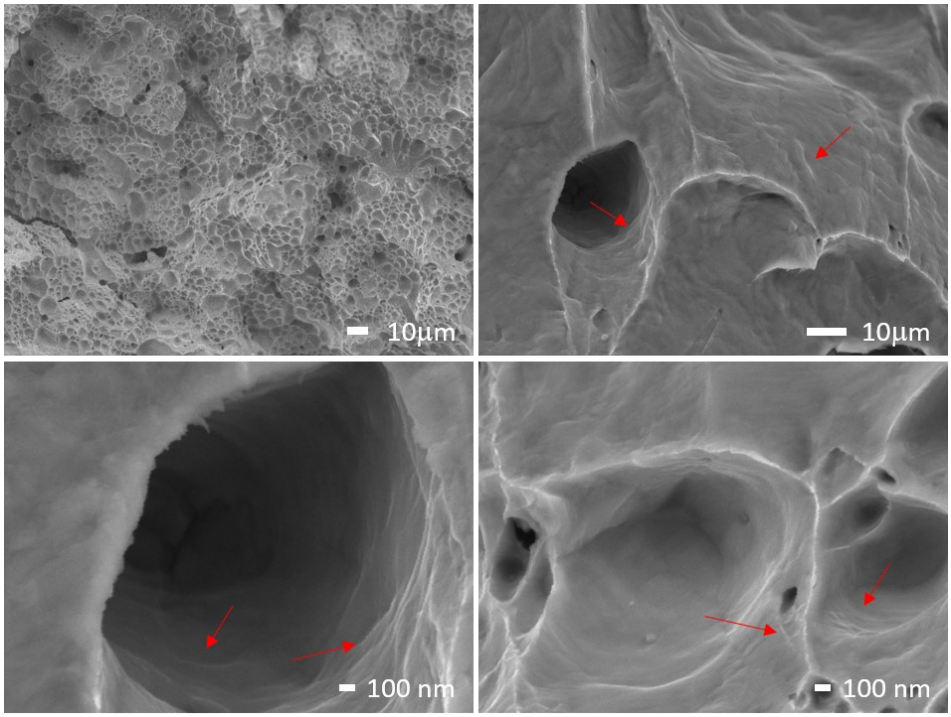

Figure 28: *Cross section of the same sample after sintering. Arrows indicate areas with visible rGO.*

Thermogravimetric analysis (TGA)

TGA was used to investigate the thermal stability of APTES and GO on Cu. Figure 29 below shows the thermal weight loss profile of Cu and two CuGO composites powders, both of which had not been thermally reduced before the measurement. One sample was synthesized with 0.25wt‰ GO, 0.2% APTES and 30 minutes APTES treatment time. The other was synthesized with 0.625wt‰ GO, 2.5% APTES and 15 hours APTES treatment time.

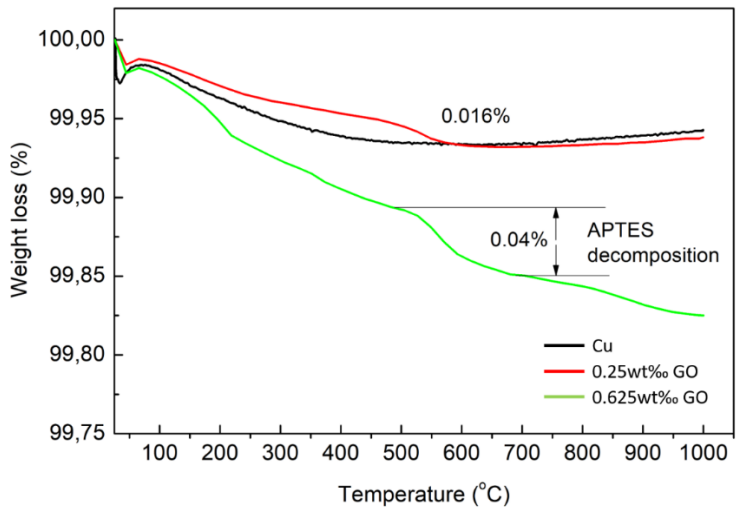

Figure 29: *TGA of Cu and CuGO composite powders with thin (0.25wt‰ GO) and thick (0.625wt‰ GO) coatings.*

The sample with the thickest coating, synthesized with 0.625wt‰ GO, decomposed at a linear rate between 100 °C to 500 °C. The other CuGO composite powder also decomposed within this range, albeit at a slower rate.

The initial weight loss starting at 70 °C owes to dehydration of intercalated water in the GO layers. This dehydration continues until 200 °C, after which decomposition of labile oxygen groups in GO dominates until 350 °C. These functional groups are mostly hydroxides and epoxides. At 350 °C, a small weight loss event is observed for the 2.5% APTES sample, indicating the onset at which more stable oxygen groups in GO decompose. In the same sample, the decomposition of APTES begins at 520 °C and results in a 0.04% weight loss. For the other sample, the weight loss is 0.016%. In other words, if one compares the weight loss with APTES concentration, the sample synthesized with 2.5% APTES lost 12.5 times less weight than the 0.2% APTES sample.

The sample with the thin coating undergoes the same weight loss events, but at 520 °C the rGO and APTES completely pyrolyze. Since the coating is thin, the gravimetric curve approximates pure Cu.

XPS

Due to the synthesis method of the CuGO powder, it was vital to analyze the integrity of the APTES and GO coating after exposure to ethanol. Figure 30 shows the survey spectrum of Cu-APTES after rinsing with ethanol, followed by drying at ambient conditions. The background was not subtracted with Shirley or Tougaard methods since the survey only served to verify the presence of elements found in APTES.

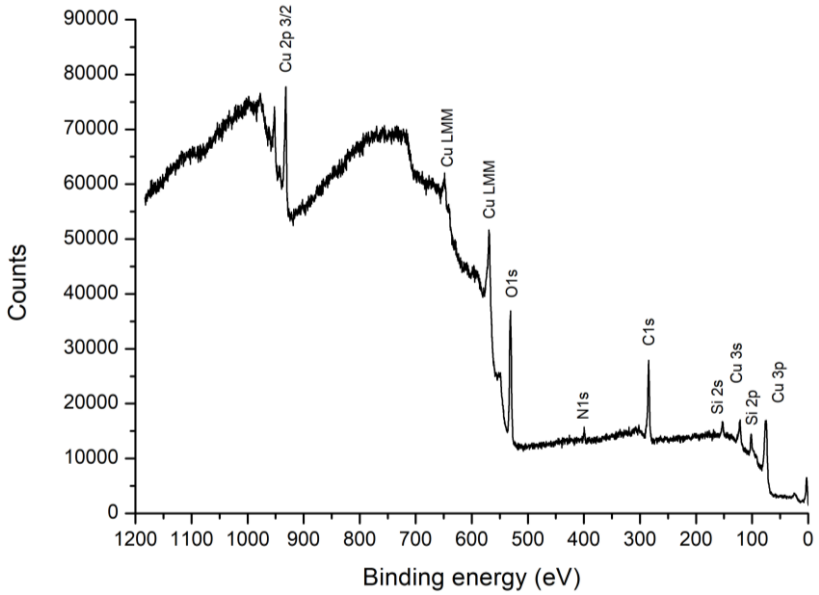

Figure 30: *Wide XPS spectrum of Cu-APTES after rinsing in water. Peaks for N 1s and Si 2s were detected at ~400cm^{-1} and ~102 cm^{-1}, respectively.*

In figures 15 to 20, it is shown that GO coatings are preserved on the surface of Cu particles even after destabilizing processes like rinsing and thermal reduction. This strong affinity between APTES and GO is attributed to two mechanisms.

Firstly, in toluene the Cu surface covalently bonds via condensation reactions to -OH groups in APTES, which have hydrolyzed at a diminished rate thanks to the anhydrous conditions. The presence of such Si-O-Cu bonds was verified using XPS spectroscopy, as shown in figure 30 and figure 31. In figure 31a), the Cu 2p peak was found to be a convolution of two peaks originating from $Cu(OH)_2$ at 935.2 eV and CuO/Cu_2O at 933.7 eV. After synthesizing Cu-APTES, the resultant XPS peak in figure 31b) show that $Cu(OH)_2$ peak vanished while a single peak at 934.3 eV was preserved, which can be ascribed to formation of Cu-O-Si bonds. As shown in figure 31c), this peak remained after thorough rinsing with ethanol. The diminished peak intensity indicates that some APTES was removed by rinsing, possibly by detaching due to copper surface oxides partaking in alcohol reduction[70].

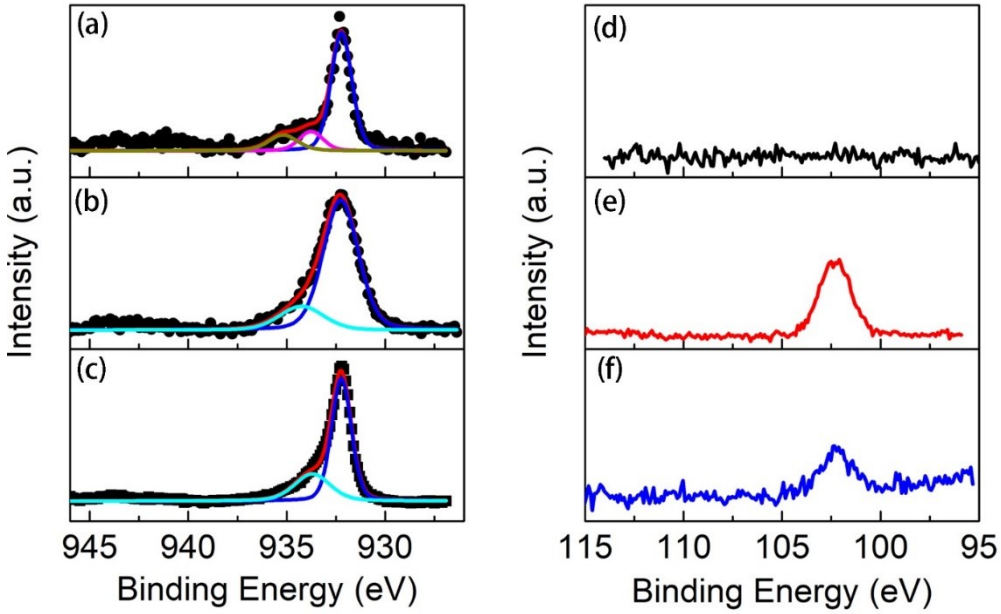

Figure 31. *Cu 2p XPS spectra of a) pure Cu particles, b) Cu-APTES synthesized using 1% APTES solution, and c) Cu-APTES after rinsing in ethanol. Si 2p XPS spectra of d) pure Cu particles, (e) Cu-APTES synthesized using 1% APTES solution, and (f) ethanol washed Cu-APTES.*

Secondly, the amine group on APTES readily undergoes protonation in hydrous environments and bestows a net positive surface charge to Cu-APTES; which in turn attracts GO electrostatically. GO is negatively charged due to carboxylic groups at sheet edges. This was confirmed by measuring a -30mV zeta potential in the GO dispersion, as shown in figure 32. As a result, well-dispersed GO nanosheets in water can rapidly self-assemble on Cu by electrostatic interaction with $-NH^{3+}$ on APTES. In XPS, the presence of APTES after CuGO synthesis was confirmed by identifying the Si 2s peak and N 1s peak. After rinsing in ethanol, the N 1s peak in figure 31e) diminishes to 31f), which reveals that the APTES layer has a sufficiently strong adhesion to Cu for acting as an electrostatic scaffold for GO. Furthermore, drying at ambient conditions promotes cross-linking between adjacent APTES molecules via condensation reactions, which further strengthens the molecular scaffold.

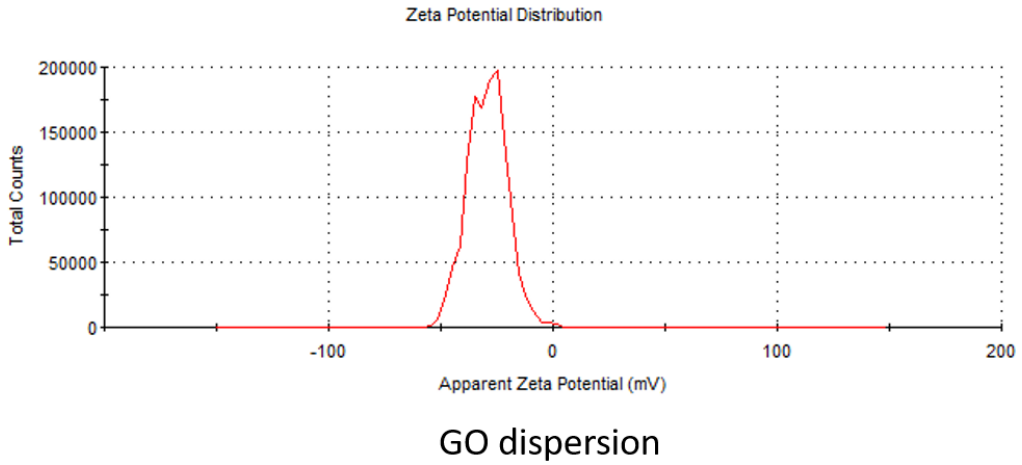

Figure 32. *Zeta potential distribution of GO dispersion used for coating.*

Corrosion protection

Chloric acid (HCl)

The first experiments were conducted with sintered samples etched in 10mL concentrated HCl for up to 300 hours. Each sample was rinsed with DI water and dried by blowing with compressed air before measurement. The results are shown in figure 33 with "R." denoting that the CuGO sample was thermally reduced prior to this experiment. As shown in the figure, the weight loss was most significant for the composite until 250 hours of etching, after which the etching of Cu accelerates due to increased porosity. Conversely, at this point the composites display higher corrosion resistance than Cu – only 7% of the original weight of Cu remains, whereas the CuGO composite synthesized with 0.625wt‰ GO have ~50% remaining weight and the composite with 0.25wt‰ GO has 70% remaining weight. Also, both Cu-rGO and CuGO with a thick coating performed worse than a Cu-rGO sample synthesized with thinner coating. HCl is highly erosive to metals due to Cl^- forming structurally weak metal chlorides, which explains why the Cu sample disintegrated after 260 hours while some CuGO remained. Similarly, the 0.625wt‰ CuGO composites etched at an accelerated rate due to the high internal porosity through which HCl could propagate. However, once saturated by HCl the diffusion of H^+ and Cl^- ions are inhibited by GO and rGO, the latter being slightly hydrophobic. The lack of weight discrepancy between Cu and composites between 0 to 175 hours of etching indicates that no appreciable amount of GO or rGO exists on the outer surface of the sintered composites.

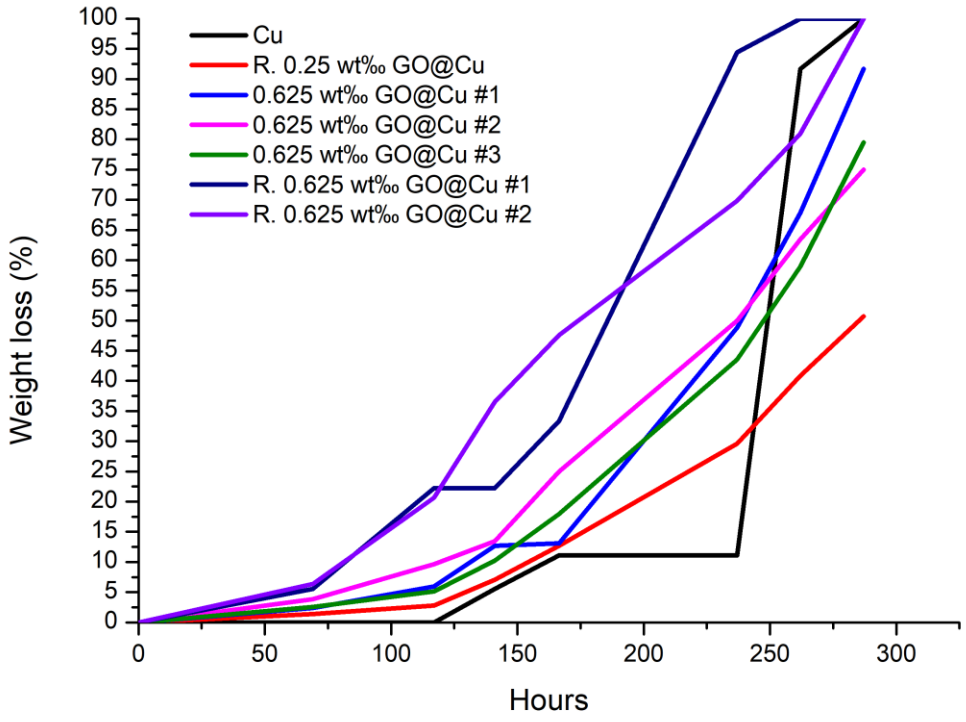

Figure 33: *Weight loss of sintered samples in 37% HCl.*

Ammonium persulfate

Ammonium persulfate (APS) is a strong oxidizing agent which is frequently used as an alternative to $FeCl_3$ in the electronics industry to etch copper circuits. In an aqueous solution, APS dissociates to ammonium ions and sulfate radicals. As such, it can be used to evaluate the overall protection provided by GO/rGO against oxidizing agents in an acidic solution.

The final etching experiment was performed with Cu and CuGO composite powders in 10 mL 0.5M APS, which were shaken once every hour to redistribute powders in the solution. The powders were rinsed with DI water and dried in vacuum before weighing. Figure 34 shows plots for percentile weight loss for Cu and 0.625wt‰ CuGO (a), Cu and CuGO samples synthesized with various amounts of APTES (b) and finally Cu and Cu-rGO (c).

After 3 hours of etching, all CuGO samples show lower weight loss than Cu. Specifically, the CuGO sample synthesized with 0.625wt‰ CuGO lost 8% weight compared with original Cu, which lost 15%. The other CuGO composite powders, which were synthesized with 1wt‰ GO and various APTES concentrations, show variance in weight loss after 3 hours. Interestingly, the samples synthesized with 0.5vol% to 1.5vol% APTES have lost more weight than the CuGO made with 0.1vol% and 0.3vol% APTES. In the latter case, the weight loss is between 8.2% and 7.4%, respectively. In comparison, the weight loss observed for Cu-rGO powders began approximating that of Cu after 1 hour in APS. The rate of weight loss for Cu-rGO powders followed no clear trend with APTES concentration, nor with thickness of the GO coating. In addition, Cu-rGO lost 7-8% mass after 1 hour in APS, while CuGO lost between 6-7% mass. Within the first 30 minutes of etching, this difference is even more significant with

CuGO losing 4-6% mass while Cu-rGO lost 7-8%. The low variance in weight loss in Cu-rGO the first hour of etching may be caused by insufficient drying.

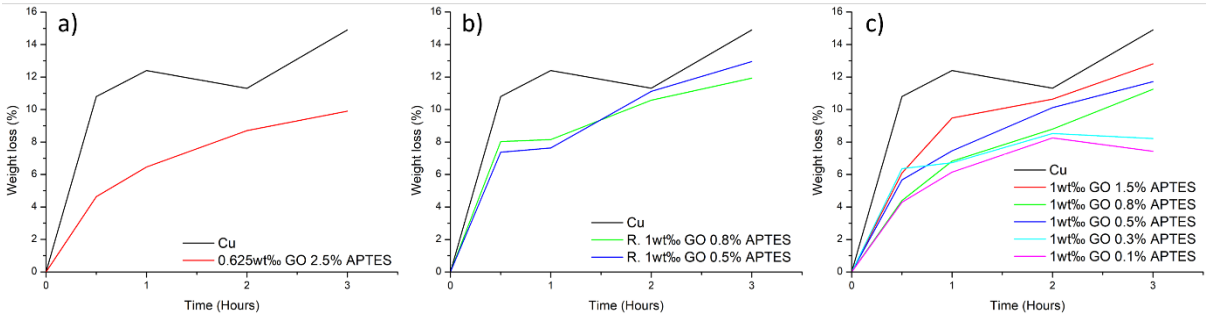

Figure 34. *Etching of Cu and a) 0.625wt‰ CuGO, b) 1wt‰ Cu-rGO and c) 1wt‰ CuGO with various APTES concentrations in 0.5M APS.*

The results show that an APTES-GO layer can efficiently protect Cu powder in an oxidizing environment consisting of 0.5M APS. In addition, based on the results herein, the thermal reduction process of CuGO to Cu-rGO is inefficient in the sense that it induces defects in GO and decomposes APTES to the point of reducing the electrostatic attraction between GO and APTES. This is evidenced by the lower chemical stability of Cu-rGO in the etching solution.

Potentiodynamic polarization curves

Potentiodynamic polarization of samples was performed in 700mL 3.5wt% salt solution with 0.5mV/s scan rate to evaluate the corrosion resistance provided by GO. Prior to running each measurement, the potentiodynamic cells were equilibrated for 20 minutes to reach open circuit potential (OCP).

Figure 35 shows the polarization curves for compacted green bodies of Cu and CuGO composites, synthesized with various APTES loadings. These CuGO composites are identical to the ones presented in figure 24. Compared to compacted Cu powder, the CuGO green bodies all exhibit E_{corr} shifted from -0.46V and reduced cathodic polarization potentials while retaining the same anodic polarization potential. In other words, the kinetics of the anodic reactions $Cu(s) \rightarrow Cu^{2+}+2e^-$ and $Cu(s) \rightarrow Cu^{+}+e^-$ have not been significantly affected by the inclusion of APTES nor GO. On the other hand, reduction reactions on the Cu surface have become inhibited. This shift in corrosion potential correlates with APTES loading and thus GO coating uniformity, as indicated by a +0.12V shift for 0.1% Cu-APTES and +0.15V for 1.5% APTES. The CuGO composite powders synthesized with 0.5% and 0.8% APTES exhibit slightly higher positive shift, which implies that the cathodic corrosion inhibition is not dominated by APTES coverage alone. It should be mentioned that for these results, the E_{corr} for Cu is -0.46V and deviates from the values presented in literature[71], which is closer to -0.35V. This lower corrosion potential could be an effect of higher surface area due to porosity.

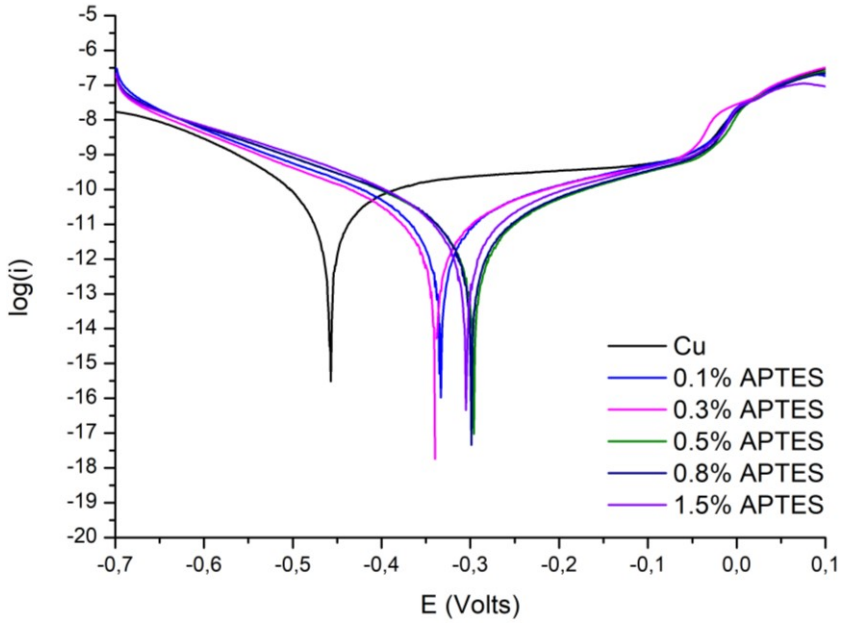

Figure 35: *Polarization curves of green bodies of Cu and CuGO synthesized with various concentrations of APTES. All samples were synthesized with 1wt‰ GO and 8 hours synthesis time.*

These results show that a APTES-GO surface treatment of Cu powder can inhibit the cathodic corrosion reaction, by virtue of acting as an oxygen diffusion barrier. The corrosion protection behavior for sintered CuGO composites was also investigated and compared with sintered Cu. These resulting polarization curves are shown in figure 36 and indicate that reduction of CuGO prior to sintering is paramount for retaining a protective layer on the composite surface. In this figure, the nearly identical polarization of Cu and 0.625wt‰ CuGO imply that the outer surface of the composite has been stripped of GO during the sintering. In contrast, the surface of the Cu-rGO composite is sufficiently passivating to result in a +0.9V shift in E_{corr} to -0.206V and a reduction of the corrosion current i_{corr} from $7.14*10^{-6}$ A/cm^2 to $3.86*10^{-7}$ A/cm^2.

Thermal reduction of the coated particles has also affected the polarization kinetics. The anodic domain in Cu-rGO displays a passivated regime that is absent in the samples of Cu and CuGO, resulting in log(i) only changing by 0.5 between -0.45V < E < -0.27V. Hence, within the interval -0.45V to -0.3V the log(i) for the Cu sample changes nearly four times as quickly as the Cu-rGO composite. In addition, log(i) in the cathodic domain between -0.206V and -0.07V is initially much lower than for both the Cu and CuGO sample. However, as shown in figure 37, the asymmetric polarization curve for Cu-rGO indicates that there is no passivation for the cathodic reaction and that the corrosion rate accelerates from E > -0.15V. In other words, the rGO coating can passivate the sample surface to limit anodic decomposition of Cu and the cathodic reaction involving reduction of solvated oxygen, yet the cathodic reduction of oxygen is diffusion limited and the passivating effect breaks down quickly when increasing the potential.

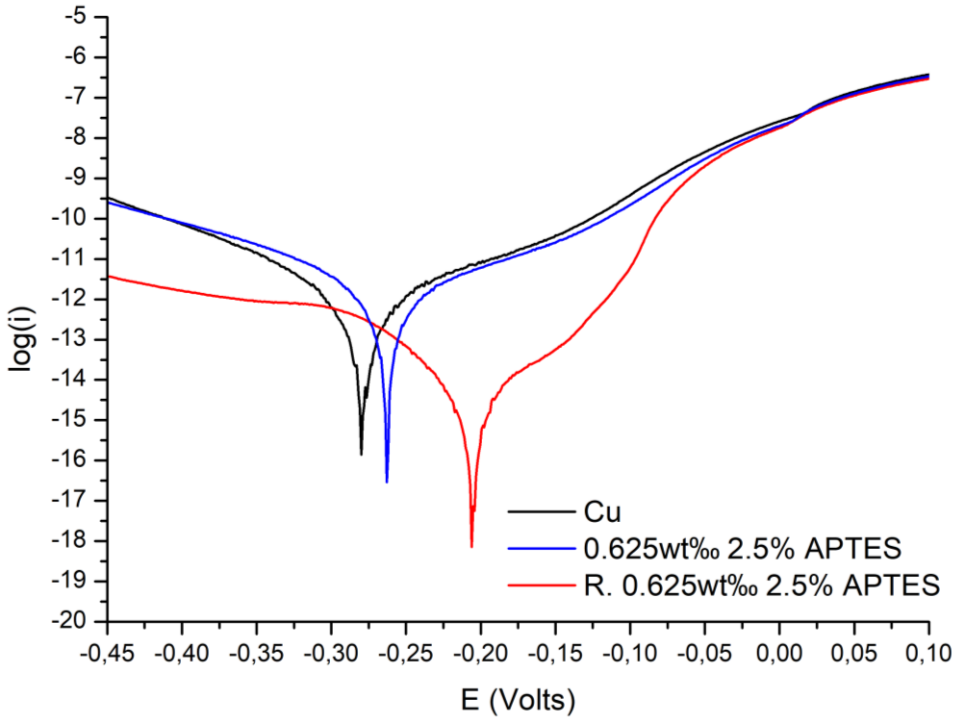

Figure 36: *Polarization curves of Cu and sintered CuGO composites with thick powder coating (0.625wt‰ GO) and 2.5vol% APTES.*

The polarization curves in figures 35 and 36 were fitted to Tafel plots to obtain estimates for $i_{Corr.}$ This was managed by manually selecting values for cathodic and anodic reaction slopes β_c and β_a that yielded reasonable values for i_{Corr}. Table 5 below summarizes the parameters used, as well as the resulting i_{Corr} and error function χ^2. The high values for χ^2 for the sintered samples are due to fitting the model based on points that were within 0.03V to E_{Corr}. This was necessary since the cathodic asymmetry shown for Cu-rGO in figure 37 prevented accurate fitting further from E_{Corr}. The results show that the corrosion current density i_{Corr} of CuGO is at the same order of magnitude, $1.91*10^{-5}$ A/cm^2 to $7.14*10^{-5}$ to A/cm^2, as in Cu, both as compacted powder and after sintering. In other words, most of the GO on the composite's outer surface is removed during sintering and that which remains is insufficient to provide to inhibit oxygen diffusion or passivate the surface oxides. On the other hand, sintered Cu-rGO powder exhibits a corrosion current of $3.86*10^{-7}$ A/cm^2, which is one order of magnitude lower than sintered Cu.

Table 5: Summary of fitting parameters used to obtain I_{Corr} and E_{Corr}

Sample type	Sample	GO (wt‰)	APTES (vol%)	β_a (mV)	β_c (mV)	I_{Corr} (A/cm^2)	E_{Corr} (V)	X^2
Green body	Cu	1		140	90	1.91*10^{-5}	-0.457	54.1
	1wt‰ GO 0.1% APTES		0.1	277	211	2.02*10^{-5}	-0.333	35.4
	1wt‰ GO 0.3% APTES		0.3	420	270	2.67*10^{-5}	-0.339	33.3
	1wt‰ GO 0.5% APTES		0.5	370	270	2.36*10^{-5}	-0.296	15.43
	1wt‰ GO 0.8% APTES		0.8	320	250	2.08*10^{-5}	-0.298	35.4
	1wt‰ GO 1.5% APTES		1.5	330	260	2.23*10^{-5}	-0.303	36.1
Sintered composite	Cu			200	160	7.14*10^{-6}	-0.279	113
	0.625wt‰ 2.5% APTES			80	78	5.31*10^{-6}	-0.278	103
	R. 0.625wt‰ APTES			65	62	3.86*10^{-7}	-0.206	90.5

Four-point probe

Figure 37 shows resistances obtained by four-point probe (4PP) measurements of sintered samples of Cu, CuGO and Cu-rGO composites. Like before, the "R." notation denotes that the CuGO powder had been thermally reduced prior to compaction and sintering. The presented resistances are averages of 5 measurements taken from one sample of each type. Sintered Cu demonstrated the highest resistance and standard deviation with 1.17±0.35Ω, which was comparable to the CuGO and Cu-rGO sample. However, the measured resistance in the Cu-rGO sample had less variance, resulting in an average resistance of 1.15±0.18Ω.

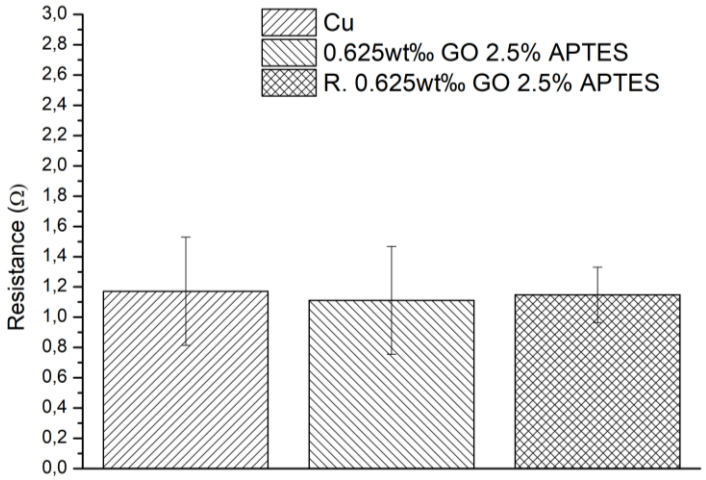

Figure 37: *Resistance in sintered Cu, CuGO and Cu-rGO samples, measured by 4PP.*

It is expected that inclusion of a GO filler would increase the resistance, since the oxygen functional groups makes it insulating or semiconducting. In this case, while the CuGO was not reduced to Cu-rGO prior to sintering, the sintering process has still removed some of the functional groups and thus limited the negative impact on conductivity. It should be mentioned that the 4PP method measures resistance at the contact surface and has limited penetration depth, meaning that most of the internal conditions are irrelevant. As shown in the polarization measurement, the outer surface of the composite is mostly free of GO. Despite low amounts of GO at or near the surface, the ~1.1Ω resistance and high variance in Cu and CuGO can be explained by incomplete sintering affecting the mean free path of the current. In other words, inclusion of GO coated particles is not detrimental to the sheet conductivity. As for Cu-rGO, it displayed comparable resistance but lower variance. The nearly identical resistance indicates that the surface primarily consists of Cu, like for the other samples, though lower variance implies higher densification. Since Cu-rGO releases less carbonaceous gases during sintering than GO and has higher thermal conductivity, the inclusion of RGO to the matrix may have promoted heat conduction and facilitated necking at the surface. Even so, since the resistances are nearly identical and GO/rGO acts as a diffusion barrier due to low solubility in Cu, the beneficial effect of this mechanism has been marginal.

Thermal conductivity

The LFA method was used to measure the thermal conductivities of sintered samples, as well as compacted green bodies of Cu and CuGO. Figure 38 presents the average thermal conductivities of samples synthesized with specific GO and APTES concentrations. The values for each sample type are composed from 3 samples.

Despite originating from the same CuGO batch and sintering under the same conditions, significant variance exists among similar samples. For example, measured thermal conductivities for sintered Cu varied from 366 W/mK to 316 W/mK, well below the 385 W/mK to 400 W/mK values for cast Cu reported in literature.

For CuGO samples the spread was heavily influenced by synthesis parameters and thermal reduction of CuGO. Samples synthesized with 0.25wt‰ GO and 0.2vol% APTES had low thermal conductivities, despite thermal reduction prior to sintering. The measured values ranged from 350 W/mK to 310 W/mK for Cu-rGO, and thermal conductivities for untreated

Cu-GO were below 300 W/mK. Conversely, the composite CuGO powders synthesized with 0.625wt‰ GO and 2.5vol% APTES displayed a wider spread in thermal conductivities, form 351 W/mK to 309 W/mK. After thermal reduction of the CuGO powder, this thermal conductivity improved significantly. The highest measured thermal conductivity for 0.625wt‰ Cu-rGO was 495 W/mK, which is 28% higher than pristine Cu.

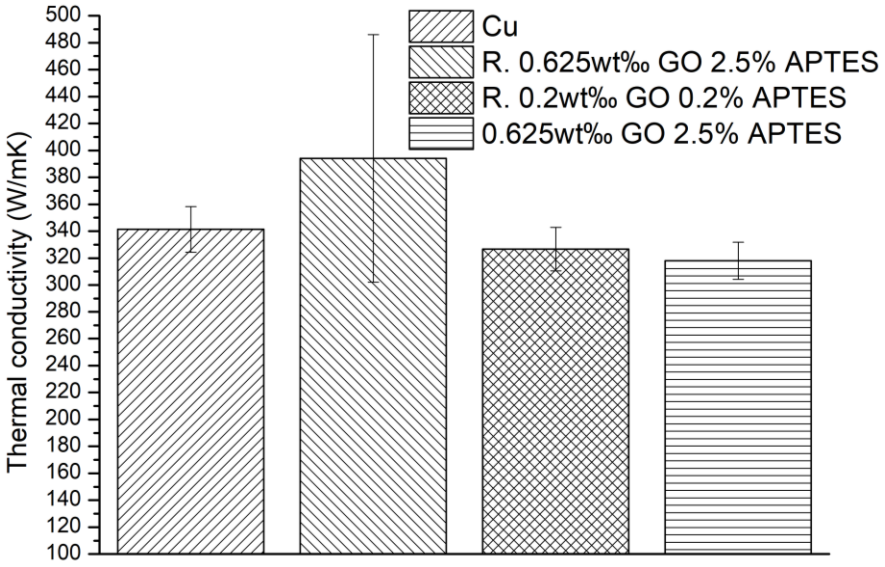

Figure 38: *Thermal conductivities of sintered samples.*

Despite the large value spread, some information can be gleaned from these results. First, although some thermal reduction of CuGO will occur during sintering, it is necessary to reduce CuGO composite powders prior to compaction. This limits the release of gases fron intercalated water in GO and decomposing functional groups, which increased internal porosity. Second, even after reduction, some Cu-rGO samples performed better than others. Specifically, the Cu-rGO composites synthesized with 0.25wt‰ GO all perform worse than Cu and composites made with thicker coatings. Finally, even after thermal reduction some Cu-rGO samples performed poorly.

The LFA method measures the bulk conductivity of the sample, meaning that internal porosity and low densification negatively affects heat transport as pores and grain boundaries scatter phonons. Hower, this alone does not explain the measured thermal conductivities. Figure 39 shows the densities of the same samples measured by Archimedes' method. Here, the five first samples displaying densities closest 8,96 g/cm^3 also have high thermal conductivities, as displayed in figure 38. However, other samples with high densities fail to demonstrate this high thermal conductivity. Thus it is not only poor densification of CuGO that limits thermal conductivity, but also the surface chemistry.

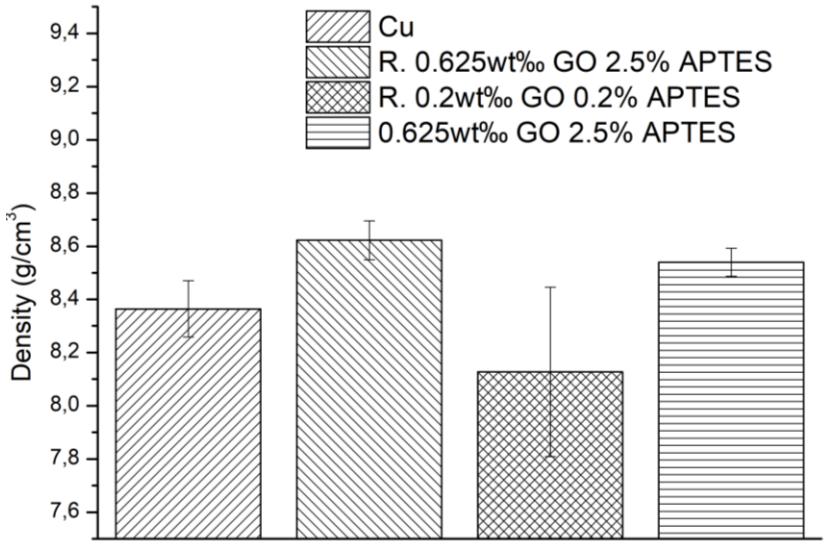

Figure 39: *Densities of samples presented in figure 36.*

As shown in figure 22d), there exist regions with low densification of adjacent Cu-rGO particles due to rGO acting like a diffiusion barrier. Yet, this sample also demonstrated thermal conductivity beyond 385 W/mK. Despite the local grains not densifying due to diffusion inhibition, the rGO sheets act as interconnecting bridges transporting phonons across particle boundaries. The efficiency of these thermal bridges would be limited by the rGO sheet size, sheet thickness and internal porosity. This would partly explain why samples made of 0.25wt‰ CuGO do not demonstrate high thermal conductivity after sintering – the internal porosity and low frequency of rGO results in few thermal bridges transporting phonons.

Vickers hardness

The efficiency of the filler as a reinforcing material is influenced by its surface chemistry and lateral size. While altering the GO lateral size is beyond the scope of this work, the surface chemistry can be altered by removal of oxygen functional groups or inclusion of new ones which have a higher affinity for the host matrix.

In this work, the surface chemistry of GO was engineered by thermal reduction. Thermal reduction would reduce the wettability of GO and consequently lower the Van der Waal interaction with the Cu substrate, but also improve filler efficiency by increasing sp^2 prevalence. In short, thermal reduction of GO would be essential to attain high thermal conductivity and structural reinforcement in the composite simultaneously.

Figure 40 shows the Vickers hardness of various thermally reduced and samples, measured with 1 kilogram-force (HV1). The samples were all compacted at the same pressure and sintered with the same process parameters. The sintered samples were then cold worked into discuses by compaction at 1.25 GPa. After cold working, the hardness for CuGO composites with thick coatings is slightly below but comparable to pure Cu. CuGO composites with lower APTES loading and consequently thinner rGO coatings demonstrate a ~10% increase in Vickers hardness.

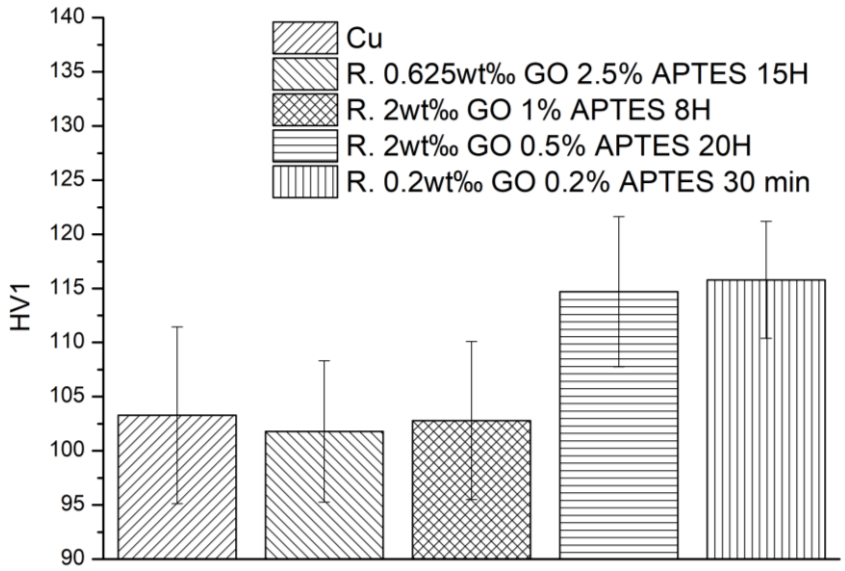

Figure 40: *HV1 hardness for Cu and reduced samples.*

The cause for hardening in these samples can be explained by a combined effect of dislocation impediment caused by rGO and higher densification from cold working. For the samples with thick coating the lower hardness can be caused by incomplete sintering as shown in figure 22, combined with rGO multilayers reducing shear (lubricating) slip planes between Cu-rGO particles.

Anticorrosion

Corrosion protection of Cu by GO coating is twofold: inhibiting the corrosion of coated powders, as well as inhibiting the corrosion of sintered and fully processed CuGO composites. This section summarizes some results for both approaches.

Acetic acid

Acetic acid has a plethora of uses in industry, but one of the more layman applications is removal of surface oxides from soft metals like copper. In this work, the hydrated versions of surface copper oxides Cu_2O and CuO act as substrates by undergoing condensation reactions with ethoxide on APTES. By etching powders with surfaces passivated by APTES, it is possible to evaluate the total coverage of APTES on Cu. It is also possible to evaluate the efficacy of APTES-GO as a passivator, compared with APTES.

In this experiment, various powders were etched in in acetic acid to determine the efficacies of APTES and GO as inhibitors for etching of surface oxides on Cu. The first preliminary experiment was performed by using 1g powders in 10 mL 10vol% acetic acid for 2,5 hours. The samples were gently shaken every 30 minutes to redistribute powders and diminish the adverse effect of a diffuse layer caused by Cu^{2+} ions passively accumulating near the GO coating, which has a net negative surface charge thanks to hydroxide and epoxide functional groups. Prior to measuring the weight loss, the etched powders were rinsed with DI water and dried under vacuum. The measured weight loss for each sample is given in figure 41.

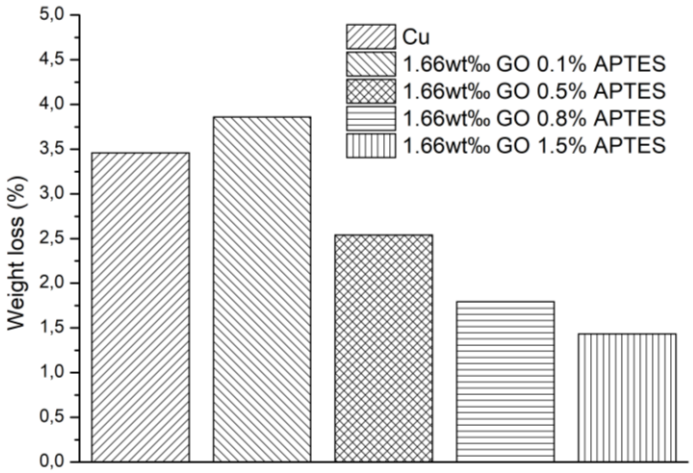

Figure 41: *Weight loss in CuGO after etching in 10% acetic acid for 2,5 hours.*

As shown in the figure, the weight loss reduces with increasing APTES loading for identical GO loading and duration of APTES functionalization. Under ambient conditions the amount of APTES chemisorbed on Cu after 8 hours is limited, resulting in not all APTES contributing to the electrostatic interaction between Cu and GO. As a result, a low APTES loading of 0.1vol% does not provide adequate protection of Cu, nor is the electrostatic interaction to hydroxide and epoxide strong enough to form multilayers of GO.

However, increasing the APTES loading in CuGO to 0.5vol% improves the etching protection. Since not all the 0.5vol% APTES had chemisorbed after 8 hours, this entails that an even lower APTES loading is adequate to work in tandem with GO as an etching inhibitor. The efficacy in reducing weight Cu loss further improves with APTES loading and results in 1.66wt‰ GO with 1.5vol% APTES inhibiting corrosion as efficiently as 0.5% APTES on Cu. This indicates that using GO as a secondary coating layer after APTES can ameliorate the corrosion protection by further inhibiting diffusion to the surface oxides.

The experiment was repeated with longer etching duration and more varied samples. This time, the etching rate was compared between CuGO and Cu-rGO by etching 0.3g powder in 10 mL 10vol% acetic acid for 7 days. Figure 42, 43 and 44 show the weight loss measured after rinsing the etched samples in DI water and vacuum drying. As shown in the figures, all CuGO and Cu-rGO powders lost less weight than the original Cu powder. For CuGO samples that were synthesized with overnight functionalization, shown in figure 42, the decline in weight loss is proportional to APTES concentration used in the synthesis. Specifically, the samples synthesized with 0.2vol%, 0.5vol% and 1.5vol% APTES lost 10.5%, 5% and 3.6% weight, respectively. In comparison, Cu lost nearly 12% weight due to etching. It is noteworthy that the highest improvement in passivation was at the 0.2vol% to 0.5vol% APTES threshold, which signifies that relatively low amounts of APTES may be sufficient for forming nearly uniform GO coatings.

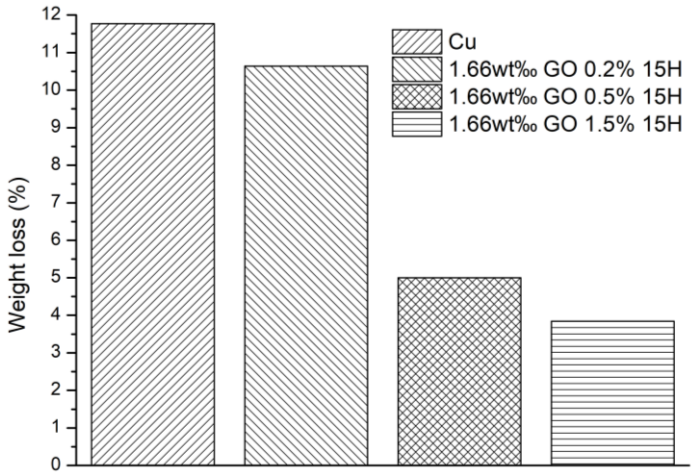

Figure 42: *Weight loss in CuGO after etching in 10% acetic acid for 7 days. The CuGO was synthesized by functionalizing Cu with APTES for 15 hours.*

Similarly, the protection against etching improves with treatment time with APTES , as seen by comparing these samples with some whose treatment time with APTES was only 8 hours, shown in figure 43. Here, CuGO synthesized with 0.5vol% APTES for 8 hours lost 3.5% more weight than its counterpart that was functionalized with APTES for 15 hours. However, for higher APTES loading this disparity diminishes, as can be seen when comparing CuGO synthesized with 1.5vol% APTES for 15 and 8 hours. Despite the much shorter synthesis duration, the weight loss is nearly identical at 3%. However, while most samples followed this trend in coating integrity, a few samples stood out. One such sample was synthesized with only 0.05vol% APTES for 8 hours yet demonstrated an efficiency comparable with 1.66wt‰ CuGO synthesized with 0.5vol% APTES for 15 hours. On its own, the diminutive amount of APTES used in synthesizing the former sample is not enough to provide this level of passivation against the acid. It should be noted that during synthesis of this sample, most of the GO dispersed in solution failed to adhere to the 0.05vol% Cu-APTES and remained in solution. In other words, it is possible that the low surface charge of 0.05vol% Cu-APTES has failed to accommodate heavier GO layer, thus selectively favoring large few-layered GO sheets.

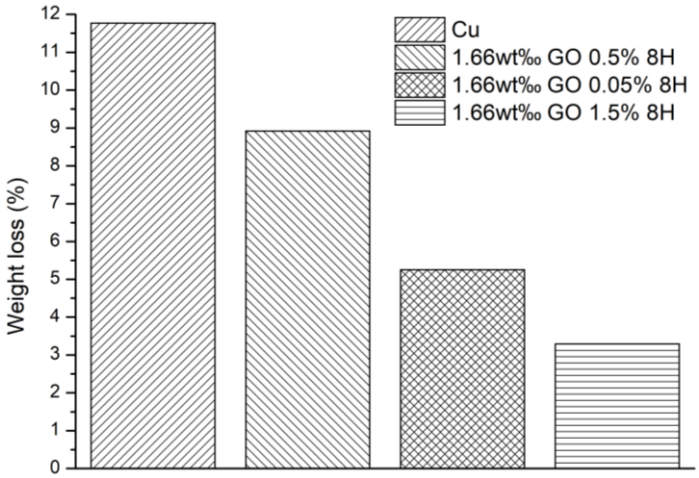

Figure 43: *Weight loss in CuGO after etching in 10% acetic acid for 7 days. The CuGO was synthesized by functionalizing Cu with APTES for 8 hours.*

Thermal reduction of 1.66wt‰ CuGO synthesized with 0.05vol%, 0.5vol% and 1.5vol% altered the weight loss profile as shown in figure 44. The Cu-rGO sample which attained the highest improvement in performance was the one synthesized with 0.5vol% APTES; while the one synthesized with 0.05vol% APTES performed worse. Respectively, the change in weight loss following reduction was 5% and 2%. For the sample synthesized with 1.5vol% APTES, influence of thermal reduction on weight loss was not detectable. In other words, for large APTES loadings the effect of thermal reduction is less significant since thick coatings of GO and rGO both prevent etching by acting as diffusion barriers against acetic acid. The invariance in weight loss could also signify that using a high APTES loading beyond 0.5vol% can be beneficial for stabilizing the GO during the reduction. Using a lower loading such as 0.05vol% APTES forms finer coatings but can deteriorate easily at elevated temperatures.

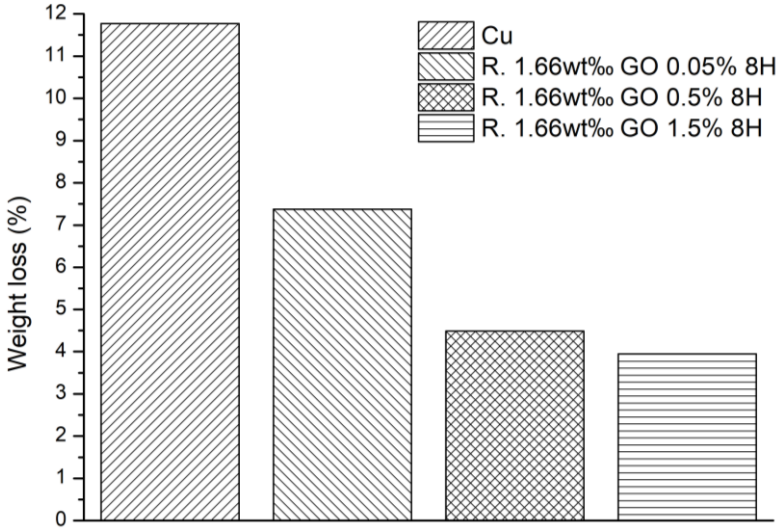

Figure 44: *Weight loss in Cu-rGO after etching in 10% acetic acid for 7 days. The Cu-rGO was synthesized by functionalizing Cu with APTES for 8 hours, then thermal reduction.*

Chapter V - Conclusions

The aim of this study was to investigate the veracity of a facile, scalable process for obtaining CuGO composite powders which could subsequently be further processed into Cu-rGO by thermal reduction. Owing to the properties of graphene (oxide), such powders can find use in additive manufacturing and conventional powder metallurgy to create sintered metal composites. The conclusions drawn from the results are summarized below:

Control of CuGO synthesis by altering synthesis parameters

Duration for functionalizing Cu with APTES

Cu-APTES was synthesized by stirring Cu in toluene and APTES with durations varying from 30 minutes, 8 hours, and 15 hours. Since the chemisorption of APTES on Cu necessitates covalent bonding with hydrolyzed APTES, the reaction is slow at room temperature and in toluene. Consequently, only CuGO samples with thin GO coatings were obtained from Cu-APTES synthesized with 30 minutes and 8 hours mixing, regardless of GO concentration.

Conversely, the samples synthesized with APTES for 15 hours or longer could accommodate more GO, resulting in CuGO composite powders with thicker coatings.

APTES concentration

This study shows that the net APTES concentration on Cu is the key factor influencing the electrostatic attraction to GO. This concentration was modulated either by altering the duration of Cu functionalization, or simply by increasing the APTES concentration for a given functionalization duration.

Thinly coated CuGO composite powders could be obtained with APTES concentrations as low as 0.05vol% after 8 hours mixing and combination with 1.66wt‰ GO loading. Similar CuGO samples were obtained with 0.1vol% to 0.3vol% APTES synthesized with concentrated 1wt‰ to 1.66wt‰ GO solutions. Such samples with low APTES loading failed to electrostatically withhold large amounts of GO and would release the excess upon gentle rinsing with water. SEM characterization of these powders confirmed that despite this release, a thin layer of GO remained in all cases. In addition, the low positive surface charge from such samples prevented retention of graphite oxide flakes and ensured that the thin GO coating was homogenous.

As for higher APTES concentrations, samples of medium and dense layer thickness were synthesized with 2.5vol% and 6.25vol% APTES, respectively. These samples were synthesized with 0.625wt‰ and 33wt‰ GO, respectively, and did not release GO upon rinsing.

However, synthesizing CuGO composite powders with a thick GO coating has not been successful for functionalization durations shorter than 15 hours.

GO concentration

As detailed in the section above, the results from this work indicate that the importance of the GO concentration is secondary to the effective APTES concentration on Cu.

Furthermore, for a given effective amount of APTES on Cu, there is a threshold for how much GO the Cu-APTES powder can accommodate. Saturating the Cu-APTES with excessive amounts of GO during solution mixing resulted in unstable coatings that easily released upon exposure to water.

In addition, although higher APTES concentration on Cu could accommodate more GO, the propensity for graphitic and non-uniform GO coatings increased with APTES.

Reduction of CuGO to Cu-rGO

EDS analysis of thermally reduced GO on Cu indicate that heating at 400 °C for 2 hours is adequate for increasing the C:O ratio from 1:1 to between 5:1 and 8:1.

Moreover, results from TGA measurements indicate that thermal reduction of GO undergo three stages. The first stage is dehydration of intercalated water molecules, which are labile and readily release between 70-200 °C. The second stage is decomposition of labile functional groups such as hydroxide and epoxides, which are the main oxygen-containing species in GO and decompose between 200-350 °C. The third stage is decomposition of more stable functional groups, such as ethers and esters. Beyond these temperatures, the reactions transitions to pyrolysis and carbonization which breaks down the C=C bonds in GO, as well as any covalent bonds C-N bonds with APTES.

However, the thermal processing of Cu-rGO did not consistently yield ameliorated performance in terms of thermal conductivity or passivation against corrosion. In figure 20, some of the Cu particle surface is exposed and detached rGO can be seen. This suggests that even a slow thermal reduction at 5C/min heating rate can decompose the coating layer by virtue of increasing interlayer pressure.

In addition to these detrimental effects on the GO coatings integrity, the thermal reduction employed in this study has a low throughput.

Sintering of CuGO and Cu-rGO (Raman/SEM/XPS)

After synthesis, GO presence on Cu particles was confirmed by SEM and Raman characterization. However, no appreciable amount of GO was detected on the outer surface of sintered CuGO composites. Potentiodynamic polarization of sintered 0.625wt‰ CuGO exhibited nearly identical E_{Corr} as sintered Cu, whereas sintered Cu-rGO demonstrated a positive shift in E_{Corr}.

After sintering, both GO and rGO was detected in the interior of the composite by using SEM and Raman. Synthesis of CuGO composites by using a Cu:GO weight ratio of 0.625wt‰ or higher resulted in a compacted internal structure, albeit with low densification as evidenced by individual CuGO particles remaining identifiable. Conversely, sintering CuGO particles with thinner coatings such as 0.25wt‰ without thermal reduction resulted in a highly porous internal structure. Despite this porosity, many adjected particles had successfully fused, indicating no diffusion impediment caused by GO in these regions.

Judging by these results, a well-controlled GO loading limits diffusion but also interlocks CuGO particles caused by GO overlapping particle boundaries. This effect was demonstrated for Cu-rGO synthesized with 0.625wt‰ GO, which incidentally also displayed higher thermal conductivity than pure Cu after sintering.

Thermal conductivity

As shown in figure 38, sintered CuGO composites displayed a marginal improvement in thermal conductivity, at best, resulting in 394 ± 92 W/mK, with the exception of a single sample

which showed a higher conductivity. The 0.25wt‰ Cu-rGO samples performed slightly worse than Cu, whereas 0.625wt‰ CuGO had the lowest thermal conductivity, averaging 326 ± 16,1 W/mK.

It should be noted that sintering at 1050 °C for 4 hours was not sufficient to obtain a fully densified Cu or CuGO samples – in figure 39, the average Cu density was 8,35 ± 0,10 g/cm^3 which is 7% lower than the density of cast Cu at 8,96 g/cm^3. Also, despite the high GO loading in 0.625wt‰ CuGO and Cu-rGO, they both achieved a higher density than sintered Cu with 8,5 ± 0,05 g/cm^3 and 8,6 ± 0,24 g/cm^3, respectively. However, due to high retention of oxygen in CuGO and the insulating properties of GO, a high thermal conductivity was not achieved.

The highly porous structure found in 0.25wt‰ Cu-rGO samples result in a low density at 8,1 ± 0,32 g/cm^3, which has an adverse effect on the thermal conductivity. Based on these disparities between 0.625wt‰ and 0.25wt‰ Cu-rGO, it seems that an rGO amount comparable to 0.625wt‰ can counteract the mechanisms forming pores in Cu-rGO samples with less rGO. However, the large spread in thermal conductivities for 0.625wt‰ Cu-rGO indicates that this ameliorating effect is highly conditional. SEM analysis has showed that partially sintered Cu-rGO particles can be interlocked by rGO sheets, which makes both the defect density in rGO sheets and their mean lateral size critical parameters for thermal conductivity. Extensive sonication, intense thermal reduction and poor dispersion in the metal matrix are potential factors that limit lateral sheet size and rGO quality.

Without any means to precisely control the size distribution of GO layers used in synthesizing CuGO composites, it will be difficult to reach a high level of reproducibility for thermal conductivity.

Resistance

The 4PP measurement shows that resistance in sintered samples of 0.625wt‰ CuGO and Cu-rGO were comparable to sintered Cu.

Though not shown in the SEM images of fracture cross sections in this thesis, the densification in CuGO and Cu-rGO were significantly higher close to the outer surface of the sample and gradually diminishing towards the center. This signifies that much GO has decomposed close to the outer surface, leaving only vestigial amounts of rGO/GO after sintering. Since the current in 4PP is transported just underneath the sample, the resistance is mainly influenced by Cu.

Hardness

The Vickers hardness in sintered Cu-rGO samples did not vary significantly from that of Cu after compaction at 1.25Gpa. This was the case for Cu-rGO synthesized with 2.5% APTES for 15 hours, as well as Cu-rGO made with 1% APTES for 8 hours. Like 0.625wt‰ Cu-rGO made with 2.5% APTES, the rGO coating on 2wt‰ CuGO made with 1% APTES was quite thick.

However, despite the high porosity in 0.25wt‰ Cu-rGO and a similar sample 2wt‰ Cu-rGO made with 0.5vol% APTES for 20 hours, they both achieved a 10% increase in hardness over Cu after compaction.

Since the all samples were made with the same Cu powder from Carpenter, the particle size in all samples are the same. In other words, the increase in hardness is not explained by Hall-Petch strengthening due to a small grain size[72].

Corrosion inhibition – polarization and weight loss measurements.

Compacted green bodies of CuGO synthesized with various APTES concentrations all demonstrated higher E_{Corr} and lower i_{Corr} than compacted Cu powder, although the i_{Corr} values were at the same order of magnitude. Specifically, the E_{Corr} shifted between 0.12V and 0.15V, whereas i_{Corr} verified to be one order of magnitude lower than i_{Corr} for Cu. In other words, before sintering the coverage of GO on Cu is sufficient to reduce the corrosion rate. In the polarization curves it is the cathodic contribution to i_{Corr} that diminished, signifying that diffusion of oxidating reactants limit the reaction rate.

However, sintered 0.625wt‰ CuGO had nearly identical i_{Corr} and E_{Corr} as pure Cu. This correlates with the 4PP measurements of various sintered CuGO samples, shown in previous sections. Considering the resistance and polarization characteristics both being comparable with Cu, this would indicate that no appreciable amount of GO remains on the surface after sintering.

As for Cu-rGO, a positive shift of 0.07V was observed and the cathodic polarization curve was lower than for CuGO, resulting in an i_{Corr} one order of magnitude lower than what was observed for CuGO green bodies and sintered 0.625wt‰ CuGO. The anodic polarization curve was also reduced, which signifies that rGo is stable enough to remain on the composite surface after sintering at 1050 °C and can passivate anodic decomposition of Cu.

Thus, reduction of GO to rGO is critical for retention not only within the metal matrix, but also on the outer surface of the particle. After reduction, the rGO is both more chemically stable and hydrophobic than GO, which further inhibits diffusion of oxidative species in the solution as evidenced by a lower cathodic reaction rate defined by i_{Corr}.

Etching CuGO and Cu-rGO powder in acetic acid and APS further elucidates the parameters governing the coating integrity, which are important for effectively distributing the GO/rGO throughout the matrix. For CuGO samples made with 1.66wt‰ GO it was found that an APTES concentration of 1.5vol% or higher is sufficient for reducing the CuGO weight loss from etching in 10vol% acetic acid to only 3%, which is nearly three times lower than pure Cu. This result was similar for samples made with 8 hours and 15 hours functionalization time. In addition, the relative difference between 1.5vol% and 0.5vol% APTES after 15 hours synthesis in toluene was small. This was also the case for Cu-rGO, which displayed less mass loss over a wide range of APTES concentrations.

Etching sintered samples in 37% HCl showed that there is not enough GO or rGO intact on the outer surface to significantly reduce corrosion rate. In addition, the corrosion rate quickly accelerates in HCl due to the high internal surface area caused by incomplete sintering. Ultimately, this severely deteriorates CuGO and most Cu-rGO samples early in the corrosion, though 0.25wt‰ Cu-rGO shows increased stability and retains 70% weight after 200 hours. The large variance in passivation indicates that the rGO distribution and adhesion to Cu can be further improved.

Similarly to etching in 37vol% HCl, the CuGO powders synthesized with low APTES and GO loading performed significantly better than both Cu and thickly coated CuGO in 0.5M APS. CuGO synthesized with 0.1% APTES and 0.625wt‰ CuGO lost 50% less weight than Cu within the first hour of etching. However, the efficacy of passivation diminished with time and weight loss was comparable with Cu after 3 hours. As for Cu-rGO, no clear trend could be established. Since APS is both acidic and highly oxidizing, the disparity between CuGO and Cu-rGO might be explained by the functional groups on GO both repelling ammonium and reacting with sulfate radicals. This effect is lost in Cu-rGO, is more hydrophobic but is also

damaged by the thermal reduction. In other words, to fully exploit the potential for Cu-rGO on industrial scale, a gentler approach much be used that does not introduce significant defects to the coating nor deteriorates APTES prior to sintering.

Chapter VI - Future work

Although the influence of APTES concentration, synthesis duration and GO concentration has been evaluated, much needs to be further investigated to ameliorate the properties of sintered samples. Below are some suggestions for further work:

- **Utilizing a different surfactant molecule than APTES**. While cross-linking in APTES is advantageous for surface engineering Cu powder, its chemisorption rate on Cu is slow, thus necessitating long synthesis duration or high concentration. Cross-linking and self-polymerization can also occur in solution, which limits the potential for increasing the chemisorption rate on Cu by raising the temperature or concentration. For this reason, it would be interesting to use alternative surfactant molecules which possess a similar structure to APTES. This way, a monomolecular layer can be assembled at a faster rate with heating and less risk of polymerization. Some alternatives to APTES would be cysteamine or 3-mercaptopropyl-triethoxydisilane (MPTES), whose sulfide groups has a high selectively to Cu.

- **More detailed study of mechanical properties after sintering**. In this work, the mechanical properties of CuGO/Cu-rGO were not assessed beyond hardness testing. Additional analysis should be performed by compression testing or by tensile testing of larger test pieces. For tensile testing, this would require machining of larger sintered samples into adequate shapes. For this reason, it would be beneficial to use selective laser sintering (SLS) or selective laser melting (SLM). Moreover, mechanical and thermal properties of laser sintered CuGO/Cu-rGO composites is a novel domain which has not been extensively explored.

- **Investigation of machining and forming processes**. Further work should also be done in machining of CuGO/Cu-rGO composites. The results from this work show that, with correct control of rGO distribution and mass fraction, it could be possible to achieve thermal conductivities higher than Cu. High thermal conductivity is primarily important in heatsinks, which is extensively used in heating elements and computer cooling fans. One approach would be to investigate the thermal properties of Cu-rGO composites after extrusion, which is a method commonly used in industry for producing such heatsinks. To this end, the material can either be extruded directly as a powder or sintered into a composite billet before machining.

- **Increasing GO/rGO volume fraction by reducing powder size**. In this work, the mean Cu particle size has been rather high at 34μm. By using a smaller mean particle size, e.g. 10μm it would be possible to achieve a higher volume fraction of rGO without affecting coating thickness. In addition, using smaller particles would increase the relative surface coverage consisting of single GO sheets, which in turn could reduce the prevalence of incomplete coatings. Using smaller particles could also increase the frequency of interlocking thermal rGO bridges like the ones found in 0.625wt‰ Cu-rGO, which displayed the highest thermal conductivity among the samples.

- **Size fractionation of GO sheets.** One way to engineer the properties of composites is to alter the distribution, orientation, and aspect ratio of its filler constituents. The GO dispersion used in this study consisted of GO sheets with an average size of 10μm, which was further compromised by processes like sonication, thermal reduction, and compression of CuGO powders. It is possible to synthesize GO sheets with controlled

aspect ratios via a modified Hummers' method, in which the pH during synthesis promotes selective precipitation of GO with the desired size. This was demonstrated by Wang et al.[73], which obtained good selectivity for 40μm GO sheets using this method.

- **Investigating the viability of scalable, inexpensive chemical reduction of Cu-rGO.** While thermal reduction of GO is a much-used process in research for obtaining rGO, it is not very scalable due to size limitations and low throughput of furnaces with inert atmospheres. Chemical reduction is an alternative, in which a chemical compound can reduce large amounts of CuGO in a batch process. In research, hydrazine is the most common chemical for hydrothermal reduction of GO. However, there are less expensive and more environmentally friendly alternatives. The list of eco-friendly reductants is growing thanks to extensive research. So far, research has shown that oxygen functional groups in GO can be reduced by organic acids like vitamin C, metal powders and baking soda[74]. Currently, there is a limited amount of research involving reduction of metal-GO composites with eco-friendly reductants.

- **Using other sintering methods**. Sintering in a ceramic furnace in inert atmosphere is a simple yet limited approach to creating densified MMC. Firstly, the density of the sintered item is limited to the effective compaction of the green body. Secondly, there is no rectification for mechanisms creating pores, such as gas release. Thus, using more advanced sintering approaches can both reduce sintering time and create denser sintered CuGO/Cu-rGO composites. Recently, spark plasma sintering (SPS) has been used by Yang et al.[75] to create Ag-rGO composite with improved electrical conductivity. Similar results can be obtained by using hot pressing[76].

Acknowledgements

Although this is only a small compilation of academic work, it could not be accomplished without the aid of others. Firstly, I would like to thank my supervisor, Professor Vincenzo Palermo for granting me this opportunity and for providing insight and support.

I owe much to Dr. Jinhua Sun. He not only shared his knowledge and proactively discussed my research with me, but often collaborated and aided me in my experiments. His role as supporting supervisor cannot be understated.

Dr. Zhenyuan Xia's positive demeanor and ideas motivated me to approach my experiments from new angles. In research it is all too easy to be consumed by the problems at hand, rather than taking a step back and re-evaluate one's options.

I would also like to thank Professor Uta Klement, Professor Antal Boldizar, my fellow doctorate students and friends.

Restrictions imposed due to COVID-19 prevented weekly "fika" gatherings, which I did not know I would miss as much as I did. Despite the sudden lack of weekly caffeine-and-sugar feasts as social arenas, I greatly appreciated the overall friendly atmosphere that facilitated both scientific and everyday discussions.

Last, but certainly not least, I must thank my family for their support and candid counsel.

References

1. Novoselov, K. S. *et al.* Electric field effect in atomically thin carbon films. *Science (80-.).* **306**, 666–669 (2004).

2. Balandin, A. A. *et al.* Superior Thermal Conductivity of Single-Layer Graphene 2008. *Nano Lett.* **8**, 902–907 (2008).

3. Lee, C., Wei, X., Kysar, J. W. & Hone, J. Measurement of the Elastic Properties and Intrinsic Strengthof Monolayer Graphene. **321**, 385–389 (2008).

4. Wang, A. *et al.* Preparation and characterizations of Cu2O/reduced graphene oxide nanocomposites with high photo-catalytic performances. *Powder Technol.* **261**, 42–48 (2014).

5. Chen, F. *et al.* Effects of graphene content on the microstructure and properties of copper matrix composites. *Carbon N. Y.* (2016) doi:10.1016/j.carbon.2015.10.023.

6. Krishnan, M. A. *et al.* Graphene-based anticorrosive coatings for copper. *RSC Adv.* **8**, 499–507 (2018).

7. Smith, A. T., LaChance, A. M., Zeng, S., Liu, B. & Sun, L. Synthesis, properties, and applications of graphene oxide/reduced graphene oxide and their nanocomposites. *Nano Mater. Sci.* **1**, 31–47 (2019).

8. Karimi, S. *et al.* A Review on Graphene's Light Stabilizing Effects for Reduced Photodegradation of Polymers. *Crystals* **11**, (2021).

9. Novoselov, K. S. *et al.* REVIEW A roadmap for graphene. *Nature* **490**, 192–200 (2012).

10. Ruhl, G., Wittmann, S., Koenig, M. & Neumaier, D. The integration of graphene into microelectronic devices. 1056–1064 (2017) doi:10.3762/bjnano.8.107.

11. Liu, W., Song, N., Wu, Y., Gai, Y. & Zhao, Y. Preparation of layer-aligned graphene composite fi lm with enhanced thermal conductivity. *Vaccum* **138**, 39–47 (2017).

12. Nag, A., Mitra, A. & Chandra, S. Sensors and Actuators A : Physical Graphene and its sensor-based applications : A review. *Sensors Actuators A. Phys.* **270**, 177–194 (2018).

13. Hu, Z. *et al.* Graphene-reinforced metal matrix nanocomposites - A review. *Mater. Sci. Technol. (United Kingdom)* **32**, 930–953 (2016).

14. Ohta, T., Bostwick, A., Seyller, T., Horn, K. & Rotenberg, E. Controlling the Electronic Structure of Bilayer Graphene. 951–955 (2006).

15. Liang, A. *et al.* Recent Developments Concerning the Dispersion Methods and Mechanisms of Graphene. *Coatings* **8**, 1–23 (2018).

16. Chen, X., Zhang, L. & Chen, S. Large area CVD growth of graphene. *Synth. Met.* **210**, 95–108 (2015).

17. Muñoz, B. R. & Gómez-aleixandre, C. Review of CVD Synthesis of Graphene **. 297–322 (2013) doi:10.1002/cvde.201300051.

18. Li, X. *et al.* Large-Area Synthesis of High-Quality and Uniform Graphene Films on Copper Foils. **3893**, 1312–1315 (2009).

19. Glavin, N. R. *et al.* Emerging Applications of Elemental 2D Materials. **1904302**, 1–22 (2020).

20. Chua, C. K. & Pumera, M. The reduction of graphene oxide with hydrazine: elucidating its reductive capability based on a reaction-model approach. *Chem. Commun.* **52**, 72–75 (2016).

21. Suk, J. W., Piner, R. D., An, J. & Ruoff, R. S. Mechanical Properties of Monolayer Graphene Oxide. *ACS Nano* **4**, 6557–6564 (2010).

22. Chem, J. M. Bottom-up synthesis of large-scale graphene oxide nanosheets. *J. Mater. Chem.* 5676–5683 (2012) doi:10.1039/c2jm15944a.

23. Abid, Sehrawat, P., Islam, S. S., Mishra, P. & Ahmad, S. Reduced graphene oxide (rGO) based wideband optical sensor and the role of Temperature, Defect States and Quantum Efficiency. *Sci. Rep.* **8**, 3537 (2018).

24. Renteria, J. D. *et al.* Strongly Anisotropic Thermal Conductivity of Free-Standing Reduced Graphene Oxide Films Annealed at High Temperature. 4664–4672 (2015) doi:10.1002/adfm.201501429.

25. Hummers, W. S. & Offeman, R. E. Preparation of Graphitic Oxide. **89**, 1958 (1958).

26. Amieva, E. J., López-Barroso, J., Martínez-Hernández, A. L. & Velasco-Santos, C. Graphene-Based Materials Functionalization with Natural Polymeric Biomolecules. in *Recent Advances in Graphene Research* (ed. Nayak, P. K.) (IntechOpen, 2016). doi:10.5772/64001.

27. Marcano, D. C. *et al.* Improved Synthesis of Graphene Oxide. **4**,.

28. Zhang, J. *et al.* Monolithic Crystalline Swelling of Graphite Oxide: A Bridge to Ultralarge Graphene Oxide with High Scalability. *Chem. Mater.* **30**, 1888–1897 (2018).

29. Park, S. *et al.* Hydrazine-reduction of graphite- and graphene oxide. *Carbon N. Y.* **49**, 3019–3023 (2011).

30. Park, S. *et al.* Chemical structures of hydrazine-treated graphene oxide and generation of aromatic nitrogen doping. *Nat. Commun.* (2012) doi:10.1038/ncomms1643.

31. Guardia, L., Paredes, J. I., Solı, P. & Tasco, J. M. D. Vitamin C Is an Ideal Substitute for Hydrazine in the Reduction of Graphene Oxide Suspensions ´ n. 6426–6432 (2010).

32. Wang, J., Caliskan, E. & Lidija, Š. Green reduction of graphene oxide using alanine. **72**, 1–6 (2017).

33. Jakhar, R., Yap, J. E. & Joshi, R. Microwave reduction of graphene oxide. *Carbon N. Y.* **170**, 277–293 (2020).

34. Le, G. T. T., Manyam, J., Opaprakasit, P., Chanlek, N. & Grisdanurak, N. Divergent mechanisms for thermal reduction of graphene oxide and their highly di ff erent ion a ffi nities. *Diam. Relat. Mater.* **89**, 246–256 (2018).

35. Dolbin, A. V *et al.* The effect of the thermal reduction temperature on the structure and sorption capacity of reduced graphene oxide materials. *Appl. Surf. Sci.* **361**, 213–220 (2016).

36. Lakshmi, B., Morshed, M., Nouri, J. M., Brabazon, D. & Naher, S. Mechanical properties of graphene oxide reinforced aluminium matrix composites. *Compos. Part B* **145**, 136–144 (2018).

37. Hu, Z. *et al.* Laser additive manufacturing bulk graphene-copper nanocomposites. *Nanotechnology* **28**, 1–9 (2017).

38. Tabandeh-khorshid, M., Kumar, A., Omrani, E. & Kim, C. Synthesis , characterization , and properties of graphene reinforced metal-matrix nanocomposites. *Compos. Part B* **183**, 107664 (2020).

39. Palermo, V., Kinloch, I. A., Ligi, S. & Pugno, N. M. Nanoscale Mechanics of Graphene and Graphene Oxide in Composites : A Scientific and Technological Perspective. *Adv. Mater.* **28**, 6232–6238 (2016).

40. Coleman, J. N. Liquid Exfoliation of Defect-Free Graphene. **46**, (2013).

41. Belyaeva, L. A. Wettability of graphene. *Surf. Sci. Rep.* **75**, 1–9 (2020).

42. Hidalgo-manrique, P. *et al.* Copper / graphene composites : a review. *J. Mater. Sci.* **54**, 12236–12289 (2019).

43. Szabo, T., Maroni, P. & Szilagyi, I. Size-dependent aggregation of graphene oxide. *Carbon N. Y.* **160**, 145–155 (2020).

44. Liu, Y., Li, Y., Li, X. & He, T. Kinetics of (3-Aminopropyl)triethoxylsilane (APTES) Silanization of Superparamagnetic Iron Oxide Nanoparticles. (2013).

45. López-zamora, L., Martínez-martínez, H. N. & González-calderón, J. A. Improvement of the colloidal stability of titanium dioxide particles in water through silicon based coupling agent. *Mater. Chem. Phys.* **217**, 285–290 (2018).

46. Zhu, M., Lerum, M. Z. & Chen, W. How to prepare reproducible, homogeneous, and hydrolytically stable aminosilane-derived layers on silica. *Langmuir* **28**, 416–423 (2012).

47. Vernon-Parry, K. D. Scanning electron-microscopy: an introduction. *III-Vs Rev.* **13**, 40–44 (2000).

48. Lewis, I. R. & Griffiths, P. R. Raman spectrometry with fiber-optic sampling. *Appl. Spectrosc.* **50**, (1996).

49. Asadena, P. & Alifornia, C. Quantitative Analysis Using Raman Spectrometry. *Focal Point* **57**, 20–42 (2003).

50. Klar, P. *et al.* Raman scattering efficiency of graphene. *Phys. Rev. B - Condens. Matter Mater. Phys.* **87**, 1–12 (2013).

51. Calizo, I., Balandin, A. A., Bao, W., Miao, F. & Lau, C. N. Temperature dependence of the raman spectra of graphene and graphene multilayers. *Nano Lett.* **7**, 2645–2649 (2007).

52. Ferrari, A. C. *et al.* Raman spectrum of graphene and graphene layers. *Phys. Rev. Lett.* **97**, 1–4 (2006).

53. Dupin, J. C., Gonbeau, D., Vinatier, P. & Levasseur, A. Systematic XPS studies of metal oxides, hydroxides and peroxides. *Phys. Chem. Chem. Phys.* **2**, 1319–1324

(2000).

54. Chen, X., Wang, X. & Fang, D. A review on C1s XPS-spectra for some kinds of carbon materials. *Fullerenes Nanotub. Carbon Nanostructures* **28**, 1–11 (2020).

55. Baba, T. & Ono, A. Improvement of the laser flash method to reduce uncertainty in thermal diffusivity measurements. *Meas. Sci. Technol.* **12**, 2046–2057 (2001).

56. Min, S., Blumm, J. & Lindemann, A. A new laser flash system for measurement of the thermophysical properties. *Thermochim. Acta* **455**, 46–49 (2007).

57. Richmond, O., Morrison, H. L. & Devenpeck, M. L. Sphere indentation with application to the Brinell hardness test. *Int. J. Mech. Sci.* **16**, 75–82 (1974).

58. Shahdad, S. A., McCabe, J. F., Bull, S., Rusby, S. & Wassell, R. W. Hardness measured with traditional Vickers and Martens hardness methods. *Dent. Mater.* **23**, 1079–1085 (2007).

59. Smith, R. L. & Sandly, G. E. An Accurate Method of Determining the Hardness of Metals, with Particular Reference to Those of a High Degree of Hardness. *Proc. Inst. Mech. Eng.* **102**, 623–641 (1922).

60. Schuetze, A. P., Lewis, W., Brown, C. & Geerts, W. J. A laboratory on the four-point probe technique. *Am. J. Phys.* **72**, 149–153 (2004).

61. Santos, T. G. 5 - Characterization of FSP by electrical conductivity. in *Surface Modification by Solid State Processing* (ed. Miranda, R.) 153–176 (Woodhead Publishing, 2014). doi:https://doi.org/10.1533/9780857094698.153.

62. Smits, F. M. *Measurement of Sheet Resistivities with the Four-Point Probe*. (1957).

63. Bottom, R. Thermogravimetric Analysis. *Princ. Appl. Therm. Anal.* **1**, 87–118 (2008).

64. Holland, R. I. Corrosion testing by potentiodynamic polarization in various electrolytes. *Dent. Mater.* **8**, 241–245 (1992).

65. Obeyesekere, N. U. Trends in Oil and Gas Corrosion Research and Technologies. *Prod. Transm.* 215–248 (2017).

66. International, A. ASTM G59-97. *Standard Test Method for Conducting Potentiodynamic Polarization Resistance Measurements* (2020).

67. Enos, David G.; Scribner, L. L. *Technical report 33*. *AMETEK Scientific Instruments* https://www.ameteksi.com/library/application-notes/solartron-analytical (1997).

68. Rafiee, J. *et al.* Wetting transparency of graphene. *Nat. Mater.* **11**, 217–222 (2012).

69. Giurlani, W., Berretti, E. & Innocenti, M. Measuring the Thickness of Metal Coatings : A Review of the Methods. (2020).

70. Poreddy, R., Engelbrekt, C. & Riisager, A. Catalysis Science & Technology dehydrogenation of alcohols with air †. 2467–2477 (2015) doi:10.1039/c4cy01622j.

71. Kear, G. Electrochemical corrosion of unalloyed copper in chloride media — a critical review. *Corros. Sci.* **46**, 109–135 (2004).

72. Hansen, N. Hall – Petch relation and boundary strengthening. *Scr. Mater.* **51**, 801–806 (2004).

73. Wang, X., Bai, H. & Shi, G. Size fractionation of graphene oxide sheets by pH-assisted selective sedimentation. *J. Am. Chem. Soc.* **133**, 6338–6342 (2011).

74. Aunkor, M. T. H., Mahbubul, I. M., Saidur, R. & Metselaar, H. S. C. The green reduction of graphene oxide. *RSC Adv.* **6**, 27807–27825 (2016).

75. Yang, Y. *et al.* Ag/graphene composite based on high-quality graphene with high electrical and mechanical properties. *Prog. Nat. Sci. Mater. Int.* **29**, 384–389 (2019).

76. Wang, X., Li, J. & Wang, Y. Improved high temperature strength of copper-graphene composite material. *Mater. Lett.* **181**, 309–312 (2016).

Paper I

Coating graphene on CU for improved thermal, mechanical properties and printability for additive manufacturing

K. H. Martinsen, J. Sun, A. Kovtun, E. Bojestig, J. Hansson, Y. Liu, J. Liu, U. Klement, E. Hryha, L. Nyborg, V. Palermo

In manuscript

Coating graphene on Cu for improved thermal, mechanical properties, and printability for additive manufacturing

K. H. Martinsen[a], J. Sun[a,*], A. Kovtun[b], E. Bojestig[a], J. Hansson[c], Y. Liu[c], J. Liu[c], U. Klement[a], E. Hryha[a], L. Nyborg[a], V. Palermo[a,b]

[a] Department of Industrial and Materials Science, Chalmers University of Technology, 41296 Göteborg, Sweden.

[b] Institute of Organic Synthesis and Photoreactivity (ISOF), CNR, via Gobetti 101, 40129, Bologna, Italy.

[c] Department of Microtechnology and Nanoscience (MC2), Chalmers University of Technology, 41296 Göteborg, Sweden.

Abstract

Graphene-reinforced metal matrix composites (GMMC) have drawn attention due to their superior mechanical, electrical and thermal properties. However, there are still difficulties that must be solved to uniformly incorporate single layer graphene within GMMCs. Herein, GMMC were prepared with uniform distribution of graphene oxide (GO) via electrostatic self-assembly on silane surfactants, followed by thermal reduction and sintering. Scanning electron microscopy and Raman characterization confirmed that reduced graphene oxide (rGO) was preserved and uniformly distributed within the GMMC. An electrical conductivity comparable to copper was obtained for the composite, indicating that rGO formed a 3D conductive network. Inclusion of 0.2wt% rGO increased hardness before and after cold working by 34% and 10%, respectively, which is attributed to load transfer. Thermal conductivity of the composite was dependent on graphene loading as adding graphene (0.625wt%) increased the thermal conductivity significantly (35%). Combined with increased laser absorbance, this improved selective laser sintering of Cu, resulting in higher density of Cu/GO compared with pure Cu. Preservation of the coating after laser sintering was confirmed by SEM and Raman. Raman also confirmed that laser sintering has an annealing effect, thus improving its heat transfer properties. Our scalable method allows new possibilities for manufacture of GMMCs.

***Corresponding author**:

E-mail address: jinhua@chalmers.se (Jinhua Sun)

Keywords:

Copper powder, graphene oxide, metal matrix composites, selective laser sintering, additive manufacturing.

1. Introduction

Metal matrix composites (MMC) serve as an interesting research area for development of high-performance materials, offering distinguished physical, mechanical, thermal and electrical properties. Such composites are playing an increasingly prominent role in the aerospace and automotive industries[1]. In particular, metal matrix composites based on copper have attracted significant attention for multiple applications ranging from heat exchangers to electric circuitry[2], because copper is abundant and is a good thermal and electrical conductor. However, copper-based matrix composites are malleable, prone to wear and over time it can also corrode in contact with moisture to form patina. One additional issue with copper is that its high reflectivity for infrared (1μm) lasers limits its utility in additive manufacturing (AM) processes like selective laser melting (SLM) and selective laser sintering (SLS)[3]. This necessitates high laser power which can be detrimental to cost effectiveness and mechanical properties due to increased heat input, which reduces cooling rate and coarsens the microstructure[4]. As a result, the poor printability of pure Cu also limits its potential applications in the aerospace and automotive industries, in which AM techniques can be used both for component production and repairs[5]. Hence, production of pure copper components is currently limited to more conventional manufacturing methods.

Graphene is an allotrope of carbon, structured as a 2D lattice consisting solely of lateral sp^2 bonds and delocalized electrons in π-bonds. It possesses ultrahigh specific tensile strength[6] (1TPa), high thermal conductivity[7] (5000W/mK), large surface area, very high carrier mobility[8] and has been demonstrated as a promising filler in polymers[9]. As unique carbon-based materials, graphene reinforced MMCs often show a better overall performance benefitting from their high electrical and thermal conductivity, excellent vibration damping properties and self-lubricating properties. Inherently, these properties make graphene composites interesting for the automotive and aerospace industries. Moreover, graphene has broad light absorbance, including in the infrared domain, which means it has the potential to reduce energy loss in laser AM processes involving reflective materials[10]–[12]. Furthermore, if the graphene can be preserved in the metal matrix after AM, this would open new possibilities for production of advanced MMCs[13]–[16].

While integrating graphene into copper to form graphene reinforced copper is expected to bring new properties and applications for the metal, there are challenges that remain to be solved to uniformly distribute graphene in the copper matrix. Firstly, due to low solubility of graphene in copper and strong Van der Waals forces between graphene layers, graphene tends to aggregate over time in copper melts[17], which makes conventional casting methods unfeasible. Moreover, the low interaction between graphene and copper result in poor interfacial adhesion[18],[19]. The combination of these issues leads to insufficient alignment and poor distribution of graphene layers in the copper matrix. Moreover, since the in-plane conductivities in graphene are much higher than the through-plane properties[20], formation of an interconnected graphene network in the metal matrix is crucial to leverage its physical properties. To this end, powder metallurgy methods like ball milling are frequently used in research to uniformly cold-weld graphene to metal powders before sintering[17],[21]. However, such physical methods are rarely applicable on an industrial scale and risk severely damaging the graphene coating as the powders are often plastically deformed in the process. A more chemical approach would both be more scalable and allow for better control of the composite powder's properties, such as coating thickness.

Instead of perfect graphene, graphene oxide (GO) has been explored as a potential precursor filler to produce graphene reinforced MMCs[6],[22],[23]. GO possesses a negative surface charge due to the presence of carboxylic group at the edges of GO sheets[24]. In addition, numerous

hydroxyls, epoxide and defects on the surface of GO makes it readily dispersible in aqueous solvents. The hydroxyl and carboxyl functional groups on GO also allow hydrogen bonding, further enriching the surface chemistry compared with graphene. Moreover, the carboxyl group bestows a net negative surface charge on GO which can be exploited to improve adhesion to a metal substrate if its surface is modified with a positively charged molecule [25],[26]. The successful encapsulation of metal particles with graphene sheets could make powder metallurgy an interesting approach for forming a graphene network in the MMC, since graphene can be distributed uniformly by coating the powder particles prior to processing by sintering and extrusion. Most importantly, the presence of graphene on Cu particles could prevent the reflection of an impinging laser and improve light adsorption, which would make copper more viable for laser AM processes like laser powder bed fusion (LPBF). In addition, a lubricating graphene coating could also improve the flowability of Cu[27], which would allow Cu powders with fine sieving fractions to be used in AM and attain better dimensional accuracy[28]. The potential for Cu powders with better flowability, stronger light absorption, increased thermal conductivity and novel mechanical properties make graphene coatings very promising for AM.

In this work, sintered composites of copper and graphene oxide were prepared with a facile, scalable solution mixing method in toluene involving coating of metal powders. The molecule 3-aminopropyltriethoxysilane (APTES) was used to bestow a net positive surface charge to copper particles, which subsequently increased electrostatic interaction with negatively charged graphene oxide. The thermal conductivity and hardness of sintered copper-graphene (GO@Cu) and thermally reduced composites (rGO@Cu) were evaluated. We also evaluated the preservation of GO and rGO in samples sintered in a ceramic furnace and by SLS with scanning electron microscopy (SEM) and Raman. Apart from the traditional powder metallurgy for the sintering of Cu/GO, the more promising additive manufacture method was for the first time investigated to sinter and build multilayer structures of graphene/Cu composites. The strong laser absorption ability of graphene prevent the reflection of laser from the surface of Cu; the coating of graphene on Cu has been proved as an efficient strategy not only to improve the printability of Cu by selective laser sintering, but also uniformly added graphene in the Cu matrix. Our method opens a new avenue for the manufacture of graphene reinforced metal matrix composites.

2. Experimental

2.1. Materials

Polycrystalline, gas atomized copper powders were purchased from Carpenter (99.9% purity, 34μm) under the product name MIM 270M ± 15μm. Toluene (98% purity) was purchased from VWR International, while 3-aminopropyltriethoxysilane (APTES , 99% purity) was purchased from Sigma-Aldrich. Graphene oxide (0.4wt%, 10μm mean lateral size, 41-50% O) was purchased from Graphenea.

2.2. Preparation of GO@Cu composite powders

Typically, the commercial copper powder was first rinsed with toluene to remove the impurities before transfer to a flask. 100ml fresh toluene was then added into 10 g powder under magnetic stirring, followed by adding a certain amount of APTES depending on the target thickness; The mixture was then kept sealed and stirring for various durations (30min, 15h, 20h). Toluene

prevented rapid self-polymerization of APTES in solution. After treatment with APTES, the solution was removed and the APTES functionalized Cu (APTES@Cu) powder was rinsed with new toluene before drying under ambient conditions. In the second step, well dispersed GO in 500ml DI water was added to a 100ml DI water suspension of APTES@Cu powder under stirring. After adding GO, the solution was kept stirring for a while before removal of the supernatant solution. Next, the GO coated Cu (GO@Cu) powder was rinsed with deionized water once before drying under low temperature overnight.

2.3. Preparation of sintered GO@Cu and rGO@Cu composites

To improve the electrical conductivity, the GO component in GO@Cu samples underwent thermal reduction (rGO@Cu) at 400°C for 2 hours under Ar protection.

In a typical small sample, 1g GO@Cu powder was consolidated into 1cm diameter disks by uniaxial, hydraulic compression under 1.25GPa. This was followed by sintering in a tube furnace at 1050°C for 4 hours in argon atmosphere at 8cm^3/s. Sintered GO@Cu (s-GO@Cu) were extracted once the furnace had cooled below 80°C. Consolidated rGO@Cu green bodies were prepared by uniaxial compaction using the same instruments and parameters. Sintered rGO@Cu (s-rGO@Cu) was prepared using the same procedure as the s-GO@Cu.

2.4. Selective laser sintering

An EOS M100 was used to sinter both rGO@Cu and Cu with 1kg powders on cast copper substrates. For a typical test, each row had lines consisting of 15 layers of powder, sintered with an Yb fiber laser operating with 40μm spot size and 1060-1200nm wavelength. The thickness of each layer was 20μm, resulting in each sintered sample line being 300μm. Lines in one row were sintered with 700mm/s scan speed and power ranging from 120W to 160W, while lines in the other row were sintered at 160W and scan speeds ranging from 400mm/s to 600mm/s.

Two samples were prepared as demonstration for further characterizations: one consisting of pure Cu, and another of GO@Cu powder synthesized with 0.625wt‰ GO and 2.5% APTES (p-GO@Cu). Both sets of samples were laser printed in argon atmosphere.

2.5. Characterization of sintered GO@Cu composites

The nanostructure and morphologies of Cu, GO@Cu, and sintered GO@Cu (s-GO@Cu) was thoroughly characterized by SEM (JEOL JSM-7800F Prime) equipped with energy dispersive spectrometer (EDS); The graphene in s-GO@Cu matrix was detected by Raman (WITec alpha300 R) with 532nm laser, the corresponding distribution of graphene in Cu matrix was investigated by Raman mapping. The hardness measurement was performed using a micro hardness tester (Struers DuraScan-70) operating at 1 kgf; The thermal conductivity of all the samples were measured by laser flash analysis (LFA) (Netzsch LFA447) and their densities were determined with Archimedes' principle.

3. Results and discussion

After the functionalization by APTES, the positively charged Cu show strong interaction with the negatively charged GO due to electrostatic attraction. The flexible feature of single layer graphene allows it to be confocally coated on the surface of graphene with strong adhesion. As shown in Fig. 1a), under low magnification, no graphene agglomeration and clusters were observed, and the Cu particles are all isolated from each other. This implies that there is no detachment of graphene during the solution processing. Under higher magnification, the SEM image of individual particles would give a sense of the coating quality in terms of uniformity and thickness. For example, Fig. 1b) show the SEM image of one typical graphene coated Cu particle, which was prepared with 0.625wt‰ GO and 2.5vol% APTES. For the rest of the article, this sample powder is referred to as p-thick-GO@Cu. As indicated by the arrows showing the graphene wrinkles, one can observe the uniform coating of GO on the Cu surface. The coating is thin enough to not obfuscate the particle surface, which makes it difficult to show the uniformity at low magnification except by identifying regions with wrinkles. By adjusting the thickness of APTES surfactant and the GO loading, a thicker and readily observable graphene coating can be obtained. For more details please refer to our other publication. In the present study, we only compared GO@Cu composite powders with coating thickness like p-thick-GO@Cu. This relatively thin coating is expected to allow better sintering of Cu.

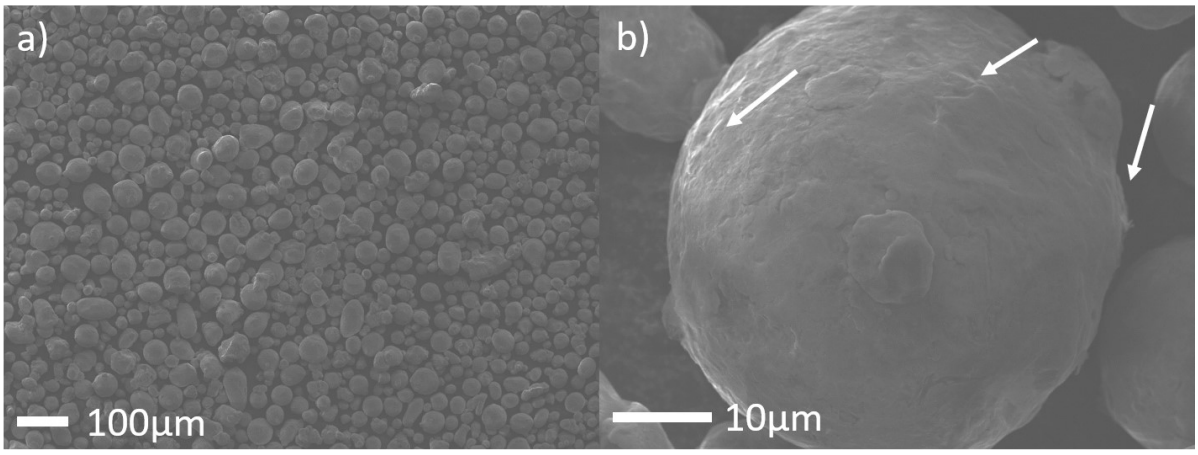

Fig. 1: *SEM images of p-thick-GO@Cu powder (0.625wt‰ GO ratio and 2.5vol% APTES) under a) low and b) relatively high magnification. No clustering was observed, and graphene was uniformly coated on Cu particles.*

3.1. Sintering of GO@CU and rGO@Cu composites

Because of the presence of oxygen containing functional groups on GO surface, the GO is unconducive. To improve the conductivity of p-thick-GO@Cu, the particles were thermally reduced at 400°C for 2 hours to obtain p-thick-rGO@Cu. Both the p-thick-GO@Cu and p-thick-rGO@Cu particles were compressed to compact small platelets with 1cm^2 diameters using 1g powder at 1.25GPa. Compacted green bodies of Cu, p-thick-GO@Cu and p-thick-rGO@Cu were then sintered in a ceramic tube furnace at 1050°C for 4 hours under argon atmosphere. These sintered GO@Cu and rGO@Cu samples are called s-thick-GO@Cu and s-thick-rGO@Cu for the remainder of the article, respectively.

Fig. 2 shows the average densities of the sintered samples measured by Archimedes' method. Each bar in the figure is an average of 2 sintered samples. Sintered Cu reached 93% of maximum density (8.96g/cm3), whereas s-thick-rGO@Cu and s-thick-GO@Cu reached 96% and 95%, respectively. The increased density in s-thick-rGO@Cu might be due to the improved internal heat transport and more efficiently distributed heat within the structure due to rGO, leading to higher densification.

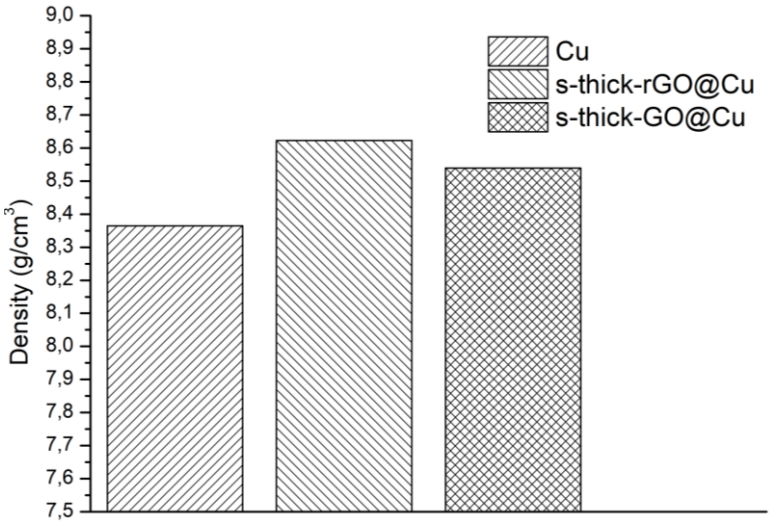

Fig. 2: *Densities of sintered Cu, s-thick-rGO@Cu and s-thick-GO@Cu.*

Samples of sintered Cu were fractured and characterized by SEM to investigate the fracture morphology and how it compares with rGO@Cu samples. Fig. 3a) to 3c) show fracture microstructures of a sintered Cu sample at various magnifications, showing that the internal structure has a densified structure and displays characteristics of a ductile fracture, such as dimples. Large dimples are encompassed by regions with higher density due to packaging of smaller Cu powder particles (Fig. 3b) and 3c)).

It was found that s-rGO@Cu samples with low GO loading (0.25wt‰ GO and 0.1vol% APTES) showed similar fracture structure as the pure Cu sample, indicating the coated graphene is very thin (Fig. 3d). This rGO@Cu sample is referred to as s-thin-rGO@Cu in the rest of the article. Like sintered pure Cu, the interior of s-thin-rGO@Cu is almost fully densified. Under higher magnification (Fig. 3e) and 3f)), ultrathin rGO with wrinkles can be observed at elongated plane regions, indicated by white arrows. High prevalence of these plane regions and dimples indicates that rGO permeates the internal matrix extensively and is situated at particle interfaces and facilitate slip upon plastic deformation by shearing stresses. Although rGO is partially present between the Cu particles, the fracture showed that the densification of s-thin-rGO@Cu was not negatively impacted by the rGO filler. This preserved the ductile properties of the sample.

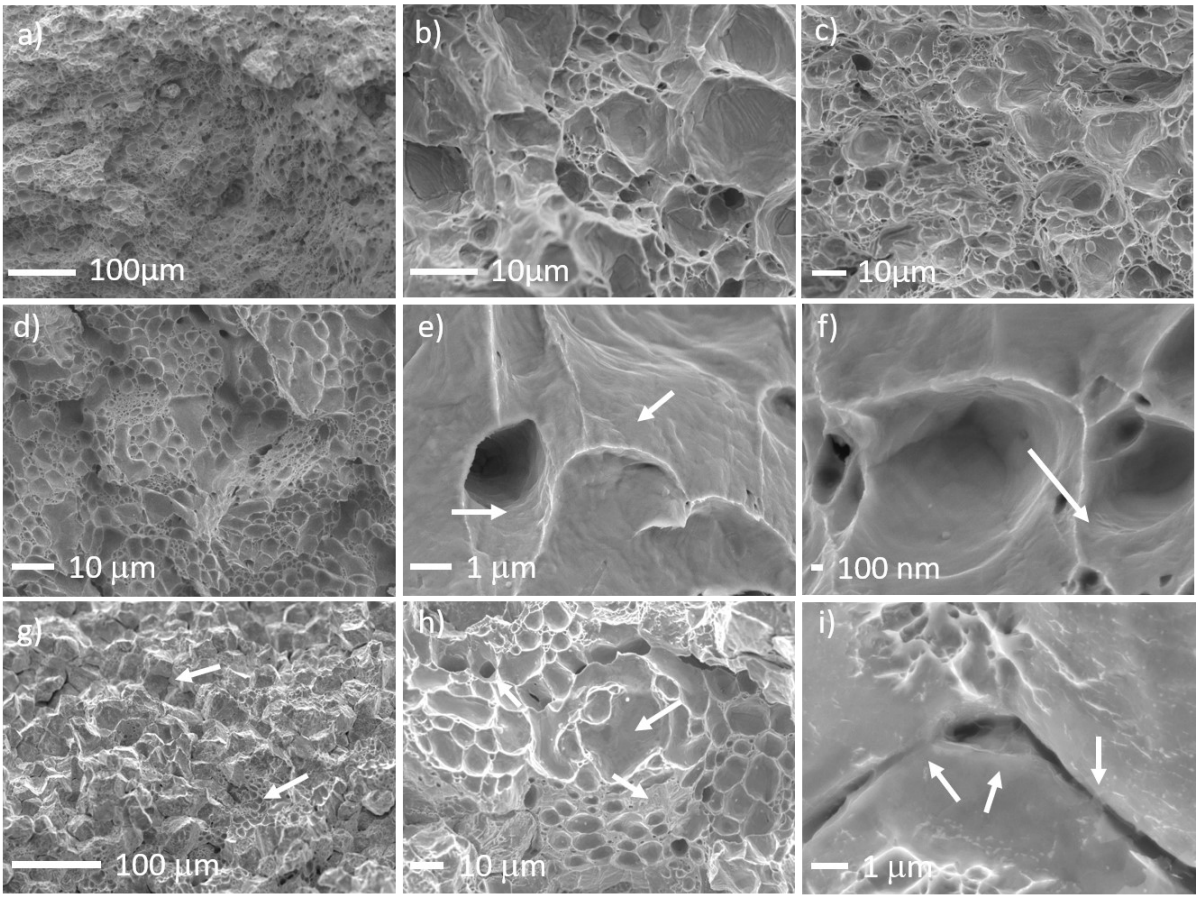

Fig. 3: *Fracture surface of a sintered samples of a)-c) Cu, d)-f) s-thin-rGO@Cu and g)-i) thick-rGO@Cu. The arrows pinpoint locations of rGO.*

In contrast, rGO@Cu samples with increased rGO loading (0.625wt‰ rGO and 2.5vol% APTES) exhibit significantly different fracture characteristics. Fig. 3g) shows the fracture surface of this sintered Cu-rGO sample, which is the thermally reduced variant of the GO@Cu powder shown in Fig. 1. This sample will be referred to as s-thick-rGO@Cu for the rest of the article. It is also shown in the same image (Fig. 3g) that more of the particle morphology is preserved due to a higher rGO concentration, which limits interparticle diffusion. In this figure, the lower arrow points at a region close to the outer surface of s-thick-rGO@Cu that exhibits higher density and more necking at particle surfaces than in the core of the composite. In other words, interparticle diffusion is less prevalent close to the sample's center, shown by the upper arrow. Here, the composite is partly sintered, and individual particles remain distinguishable. Fig. 3h) was taken from another section of s-thick-rGO@Cu that was close to the outer surface, which demonstrates an interparticle fracture surface like s-thin-rGO@Cu displayed in Fig. 3d). Moreover, the center arrow points at a large, oblong dimple inside which a 10µm region with wrinkled rGO can be seen together with darker spots consisting of multilayer rGO. This indicates that, despite coating the rGO@Cu powders nearly uniformly, subtle differences in rGO content can lead to vastly different fracture mechanics. Moreover, inspection of the preserved rGO@Cu particles close to the composite's core in Fig. 3g) shows the rGO coating bridging particle boundaries. This feature is indicated by white arrows in Fig. 3i) and may contribute to higher thermal conductivity and structural integrity in brittle parts of the composite[29]. The rGO bridges are also accompanied by vicinal necking of pure Cu, which

suggests that while rGO inhibits diffusion locally, exposed areas of Cu may still densify if the sintering process would be extended.

The rGO content on the outer composite surface was evaluated using Raman spectrometry. Fig. 4a) shows an optical image of the outer surface of another s-rGO@Cu sample (0.5wt‰ GO and 0.5vol% APTES) prepared by conventional sintering after thermal reduction of the powder. There are only trace amounts of amorphous carbon on the outer composite surface, which is identifiable by black spots. In comparison, Raman mapping of the inset area with respect to the G band signal (1580 cm^{-1}) in Fig. 4b) confirms that appreciable amounts of few-layered rGO remain on most of the outer surface after reduction and sintering, which is otherwise not readily observable by eye. The terraced morphology of the s-rGO@Cu surface causes the mapping surrounding the cross marker to be slightly out of focus, hence lowering the overall G-band mapping intensity. The Raman spectrum in Fig. 4c) containing characteristic D (1350cm^{-1}) and G (1580cm^{-1}) bands originates from the point indicated by the cross marker, which contains rGO multilayers.

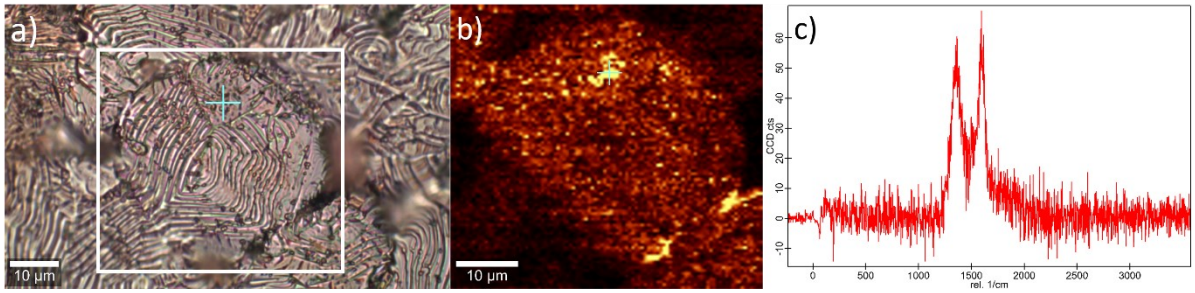

Fig. 4: *a) Optical microscopy image, b) G-band Raman mapping and c) Raman spectrum of a GO@Cu sample sintered after thermal reduction.*

Due to the uneven fracture surface of this sample, Raman mapping of rGO content in the interior of the composite was unfeasible. Point analysis was instead performed on corrugated edges vicinal to the dimple structures shown in Fig. 3), as rGO was not readily visible by SEM on these surfaces. The Raman spectra of two such sites are given in Fig. 5a) and 5b) and compared with an arbitrary site on the fracture surface, indicated with a green marker in the center of Fig. 5c). The three spectra all display signal intensities for D (1350cm^{-1}) and G (1580 cm^{-1}) bands which are characteristic to rGO, with an I_D/I_G ratio close to 1 in all cases. However, spectrum a) and b) which originate from the ridges vicinal to dimples demonstrate higher rGO content than the spectrum from site c). This was evident by the peak CCD counts for a) and b) being more than 10000 and 6000, respectively, versus 2000 for c). Wang et al.[30] found a similar distribution of graphene at dimple ridges in graphene-aluminium composites and attributed lower load transfer and brittle fracture to poor interfacial adhesion. However, in this work the fracture surface of s-rGO@Cu samples remain primarily ductile despite the high rGO content. The red spectrum a) and blue spectrum b) also show bands for CuO (520cm^{-1}), as well as Si from APTES (630cm^{-1} and 1000cm^{-1}). The large bands at 50cm^{-1} to 100cm^{-1} are artefacts from the background subtraction and convolutes additional bands for CuO, which would normally be found at 290cm^{-1} and 340cm^{-1}.

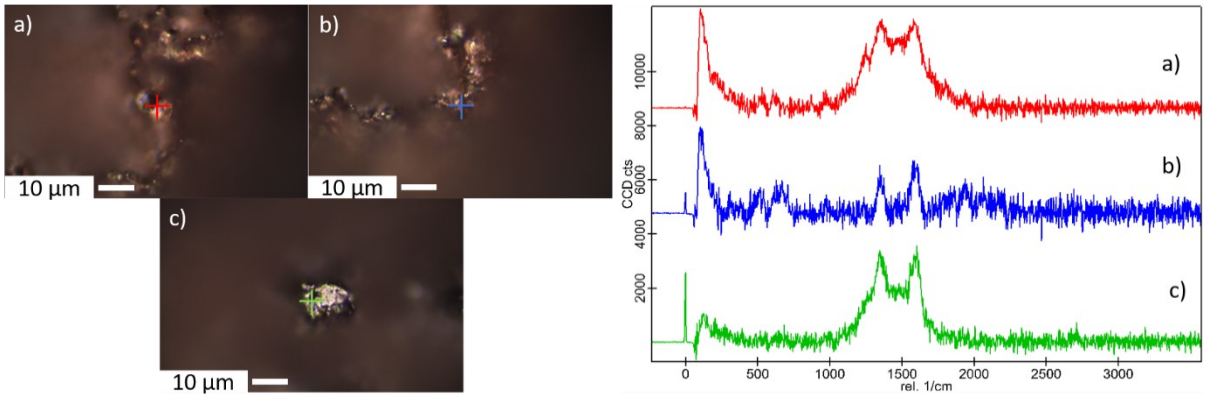

Fig. 5: *Raman analysis on the cross section of the sintered Cu-rGO sample. The spectra are taken at the location of the marker, shown in the center of the respective optical images.*

The combination of SEM and Raman characterization of sintered Cu-rGO samples indicate that, although some rGO remains on the outer sample surface after sintering, it is mostly existent within the composite's interior. Moreover, the existence of dimples through most of the composite's interior implies that at low GO loading (0.5wt‰ GO and 0.5vol% APTES), the GO can remain within the structure without embrittling the matrix. The main detriment to mechanical properties is caused by release of oxygen and carbonaceous gases from GO/rGO during sintering, which further weakens the interfacial adhesion between Cu and the coating.

The significance of rGO persisting within the metal matrix was evaluated with the laser flash method (LFA), which measures thermal conductivities in solid samples. Fig. 6a) shows the thermal conductivities in green bodies of Cu, p-thick-GO@Cu and p-thick-rGO@Cu. Due to high porosity and surface oxides, the thermal conductivity for the Cu green body was only 75W/mK, which was further reduced to 32W/mK for p-thick-GO@Cu by grafting APTES and GO to the Cu particle surface. This reduction in thermal conductivity can be explained by grafted APTES inherently possessing low thermal conductivity, being a polymerized silane. After heat treatment to obtain p-thick-rGO@Cu, the thermal conductivity is improved by 56% relative to p-thick-GO@Cu. Although the thermal conductivity is improved, it remains lower than pristine Cu since, at this point, there is no interconnection between the coated particles.

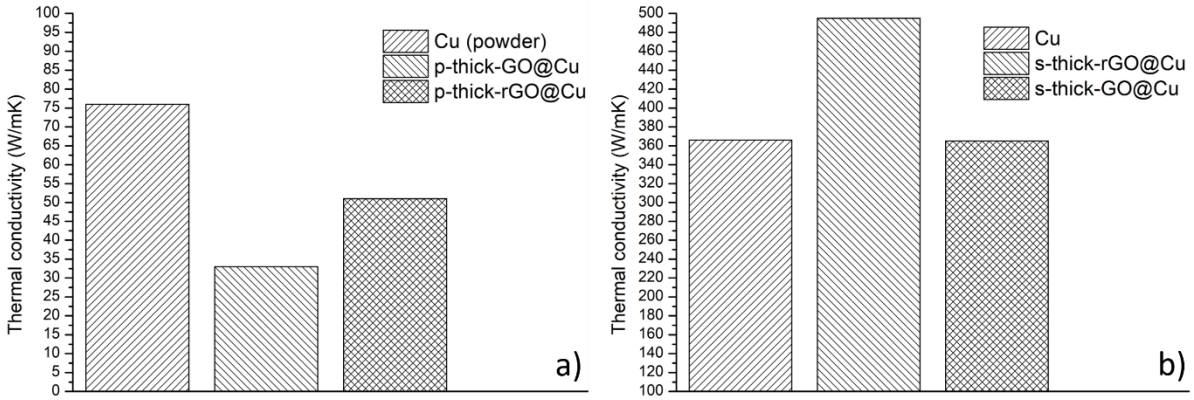

Fig. 6: *Thermal conductivities of a) compacted green bodies and b) sintered samples.*

However, after compaction and sintering the thermal conductivity can be restored to levels comparable with pristine Cu and even further improved, as shown in Fig. 6b). Here, it is shown that the sintering process at 1050°C for 4 hours yields Cu samples with lower thermal conductivity (366W/mK) than what is reported for cast Cu (385-400W/mK). This is attributed to the density of the sintered sample reaching 93% of cast Cu, given in Fig. 2, due to decomposition of surface oxides and subsequent pore formation. Interestingly, the GO@Cu sample (0.625wt‰ GO) demonstrates nearly identical thermal conductivity as Cu and 95% density. Moreover, after thermal reduction of the GO@Cu powder (0.625wt‰ GO) the thermal conductivity is raised to 495W/mK, which is ~23% higher than the best thermal conductivity for Cu reported in literature, as well as ~33% higher than our Cu sample. This coincides with a small increase in density, up to 96% as shown in Fig. 2.

Some information can be gleaned from these results. First, although thermal reduction of p-GO@Cu will occur during sintering due to the elevated temperatures and can contribute to increased densification, the highest thermal conducitivity is obtained by reduction of p-GO@Cu prior to compaction. This reduces the release of intercalated water, CO/CO_2 and oxygen from the GO coating during sintering which would otherwise contribute to increased internal porosity. Second, as shown in Fig. 3i), there exist regions with low densification of adjacent rGO@Cu particles due to rGO acting like a diffusion barrier. Yet, this particular sample also demonstrated a thermal conductivity of 495W/mK and 96% maximum density. Despite the local particles not densifying due to diffusion inhibition, the rGO sheets act as interconnecting bridges reinforcing the microstructure and transporting heat across particle boundaries. Moreover, while decomposition of surface oxides occur in all samples, the interconnecting GO and rGO coatings can restrain the particles to prevent significant pore formation, which limits the overall impact on density. The efficiency of these thermal bridges would be limited by the rGO sheet size, sheet thickness and internal porosity, which explains why the same effect was not observed in s-thin-rGO@Cu (Fig 3d)-3f)).

Although the rGO coating contributes to raising thermal conductivity via formation of an interconnected rGO network, its effect on the composite's surface properties has not been detailed. For this reason, the electrical conductivity was assessed with the four-point probe (4PP) method. Fig. 7 shows resistances obtained by 4PP measurements of sintered samples of Cu, s-thick-GO@Cu and s-thick-rGO@Cu composites. The presented resistances are averages of 5 measurements taken from one sample of each type. Sintered Cu demonstrated the highest resistance and standard deviation with 1.17±0.35Ω, which was comparable to the GO@Cu and Cu-rGO sample. However, the measured resistance in the s-thick-rGO@Cu had less variance, resulting in an average resistance of 1.15±0.18Ω.

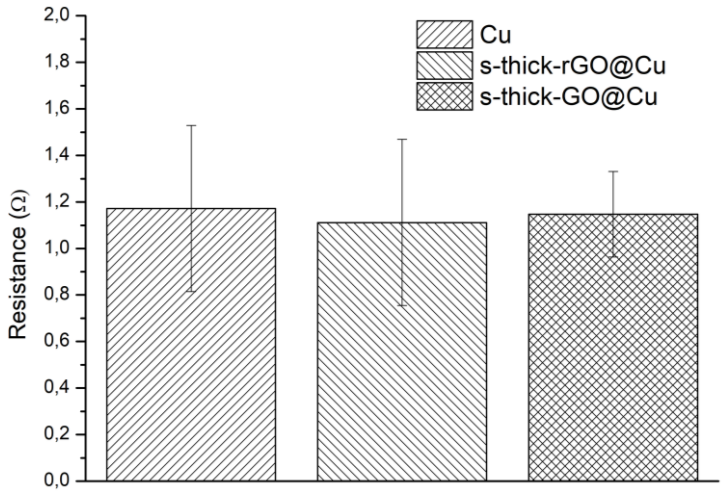

Fig. 7: *Resistance in sintered Cu, s-GO@Cu and s-rGO@Cu samples measured by 4PP.*

It was expected that inclusion of a GO filler would significantly increase the measured resistance, since oxygen functional groups make it insulating or semiconducting depending on oxygen content. In this case, while the GO was not reduced to rGO prior to sintering, the sintering process has still removed some of the functional groups and thus limited the negative impact on conductivity. It should be mentioned that the 4PP method measures resistance at the contact surface and has limited penetration depth (100nm), meaning that most of the internal conditions are of little significance. While the Raman mapping (Fig. 4 and Fig. 5) shows that rGO can remain on the MMCs surface after sintering, the comparable ~1.1Ω resistance and variance in Cu and s-thick-GO@Cu implies that not enough GO is preserved on the surface to influence the measurement. The result is similar for s-thick-rGO@Cu, though lower variance implies higher densification leading to better conductivity. Since Cu-rGO releases less carbonaceous gases during sintering and has higher thermal conductivity than GO, the inclusion of rGO to the matrix may have promoted heat conduction and facilitated necking at the surface. Even so, since the resistances are nearly identical and GO/rGO acts as a diffusion barrier due to low solubility in Cu, the beneficial effect of this mechanism has been marginal.

The reinforcing effect of the rGO fillers were evaluated by measuring the Vickers microhardness of sintered samples (s-rGO@Cu) at 1 kgf (HV1), shown in Fig. 8 as the average of 5 measurements on separate platelets. The synthesis parameters for all s-rGO@Cu samples in the figure are summarized in table 1 below. In the table, treatment time refers to the duration of APTES@Cu synthesis in toluene. It should be mentioned that, despite the long treatment time (20 hours), the sample s-thin-2-rGO@Cu is classified as thinly coated with rGO since not all of the dispersed 2wt‰ GO adhered to APTES@Cu when synthesizing the composite powder.

Table 6.Synthesis parameters for hardness tested samples

Sample	GO [‰]	APTES [vol%]	Treatment time
s-thick-rGO@Cu	0.625	2.5	15 hours
s-thin-2-rGO@Cu	2.0	0.5	20 hours
s-thin-3-rGO@Cu	0.2	0.2	30 minutes

As shown in Fig. 8a), the Vickers hardness of s-rGO@Cu samples are strongly dependent on coating thickness. Interestingly, the sample s-thick-rGO@Cu (Fig.1 and Fig.3g)-3i) which demonstrated high thermal conductivity (495 W/mK) shows somewhat lower hardness (38HV1) than sintered Cu (53HV1), while the sample s-thin-rGO@Cu exhibits 36% higher mean hardness (71HV1) than Cu. This discrepancy can be explained by the LFA method measuring transient heat passing through the sample, meaning that it should ideally be homogeneous. However, the sample s-thick-rGO@Cu has higher rGO content and density in the core, as compared with a more porous outer surface caused by carbonaceous gases from residual oxygen functional groups in rGO. Thus, the lower hardness reflects the conditions of the composite's surface. In contrast, utilizing less rGO in the sample s-thin-2-rGO@Cu reduces the amount of gas escaping from the core, resulting in higher density at the surface. Furthermore, the measured microhardness is higher in s-thin-rGO@Cu than in Cu, which means an additional mechanism must be in effect to raise the microhardness in s-2-thin-rGO@Cu beyond sintered Cu. Also, as evidenced by high variance, this microhardness is not uniform throughout the sample surface. This implies that in some areas of the sample with interconnecting rGO at particle interfaces, the Cu matrix is strengthened by compressive load transfer.

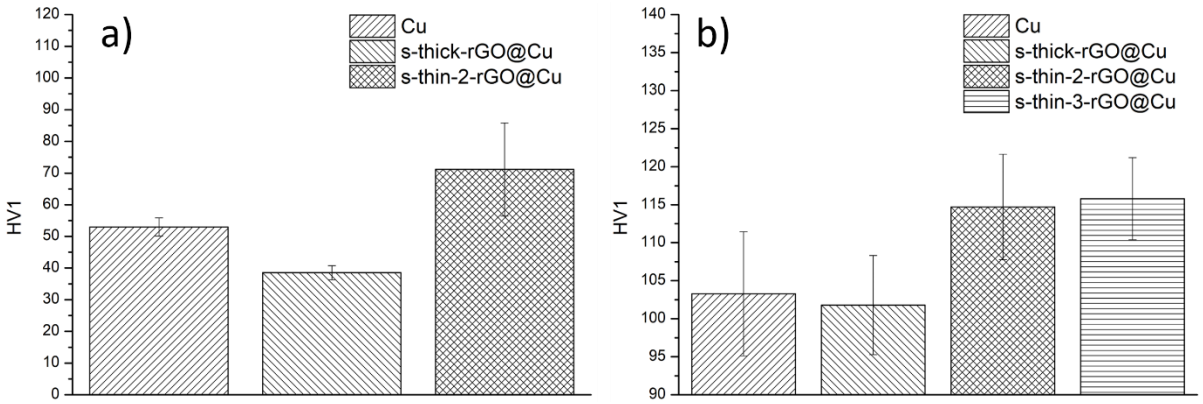

Fig. 8: *HV1 hardness of a) sintered samples and b) sintered samples after uniaxial compression.*

Sintered samples were cold worked to investigate whether they could be strengthened, as Li *et al.*[31] and others have reported that this approach redistributes graphene and eliminating pores. As shown in Fig. 8b), after cold working by uniaxial compression at 1.25GPa, the hardness disparity between Cu (103HV1) and s-thick-rGO@Cu (102HV1) becomes less pronounced. This modest increase in hardness for s-thick-rGO@Cu relative to Cu is most likely due to pore elimination caused by the cold working. Although this sample displayed higher thermal conductivity than Cu (495W/mK), which was attributed to the rGO forming a conductive network within the matrix, the low Vickers hardness indicates no improvement in interfacial

bonding, load transfer or dislocation pinning between Cu and rGO. This contrasts with the samples s-thin-2-rGO@Cu (115HV1) and s-thin-3-rGO@Cu (116HV1) which were synthesized with 0.2%-0.5% APTES and thin rGO coatings, yet show ~10% higher HV1 hardness than Cu.

This suggests that while a high (2.5vol%) APTES loading facilitates formation of thick GO or rGO coatings on Cu, it can have an adverse effect on interfacial bonding between rGO and Cu after sintering. In the case of p-thick-GO@Cu, the strong electrostatic surface charge on APTES@Cu particles resulted in all the dispersed GO (0.625wt‰) bonding electrostatically to the particles. As a result, the coating is an amalgam of several layers of GO sheets with various lateral sizes. While this coating can improve thermal conductivity by transporting heat between adjacent layers, the outer layers are only loosely bound to the APTES@Cu substrate and can be readily displaced under plastic deformation. In contrast, the much lower APTES loading in s-thin-2-rGO@Cu and s-thin-3-rGO@Cu means that more of the GO can be in contact with the Cu surface during sintering, thus allowing more covalent bonds between GO and Cu/CuO.

3.2. Selective laser sintering of GO@Cu

Since these results indicate that rGO can influence the thermal conductivity and light absorbance of copper, its potential as a thermal coating to improve laser sintering processes was investigated next. Fig. 10 shows lines consisting of 15 layers of 20µm size made with 0.625wt‰ GO@Cu powder prepared by selective laser sintering (SLS) at various intensities and laser scan speeds. All lines were successfully sintered to the copper substrate, and the effect of each set of parameters could be evaluated by observing the line's surface roughness. Moreover, the metallic luster normally found in Cu is not observable in any of the sintered lines. Instead, the sintered lines show darker hues which are dependent on the laser power and scanning speed. For example, the subsample in Fig. 10c) was sintered at 120W and with 700 mm/s scan speed, resulting in a porous surface and darker coloration than the other lines. Maintaining the scan speed and increasing the laser intensity to b) 140W and finally c) 160W yielded significant and sequential improvement in the lines' density while at the same time restoring some of the metallic luster. A similar effect was observed by maintaining the laser power at 160W while increasing the scan speed from d) 400 mm/s to e) 500 mm/s and finally 600mm/s. Although the line sintered with the slowest scan speed displayed the highest degree of densification among all 6 lines, the observable difference among lines d), e) and f) was not considerable. The gradual change in density and coloration implies that some rGO is preserved even after sintering at the highest energy output (Fig. 10d)), while being proportionally more abundant with lower energy output.

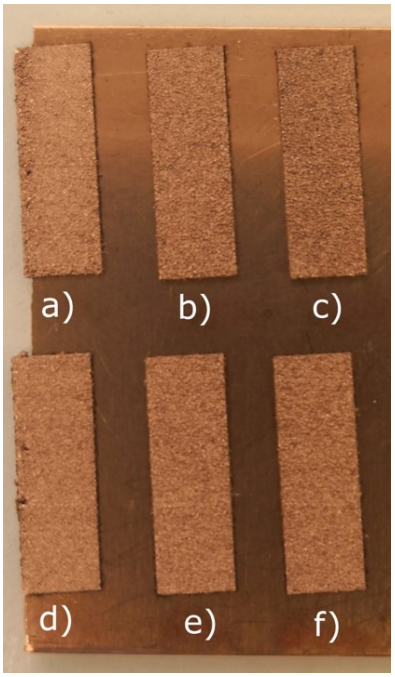

Fig. 10: *GO@Cu composite densified by SLS. The top row was sintered with 700 mm/s scan speed and a) 160W, b) 140W and c) 120W laser power. The lower row was sintered at 160W and d) 400 mm/s, e) 500 mm/s and f) 600 mm/s scan speed.*

Application of a GO coating and subsequent reduction during laser sintering significantly improves the heat transfer between deposited layers and improves laser absorbance, as compared with the highly porous morphologies found in SLS processed pristine Cu, shown in Fig. 11. The 6 sample lines created with SLS were sintered with the same parameters are their GO@Cu counterparts. As shown in Fig. 11d), even a Cu line sintered with 160W power and 400 mm/s scan speed failed to heat Cu close to the melting point, resulting in Cu particles in each layer retaining a spherical structure. Moreover, lower laser intensities are insufficient for initiating necking between adjacent Cu particles, resulting in fragile or even disintegrated structures shown in Fig. 11b) and 11c), respectively. For Cu sintered at 160 W, slowing the scan speed to 400 mm/s does not result in higher density in the deposited layers – Fig. 11d) displays the same partially sintered and porous structure as in Fig. 11a).

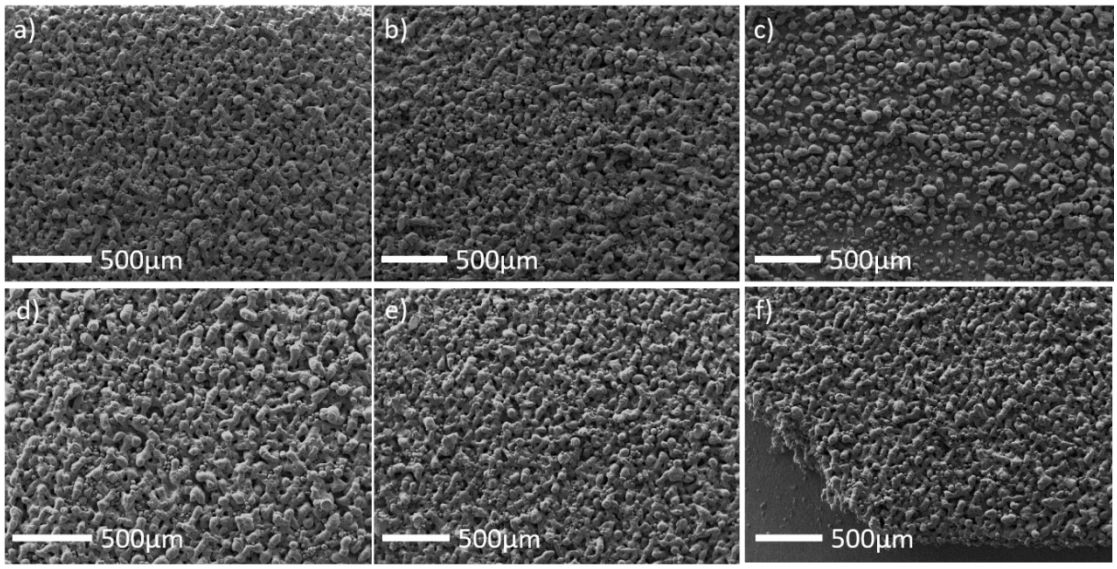

Fig. 11: *SEM images of Cu powder sintered with SLS. The Cu powders in the top row were sintered with a) 160 W, b) 140W and c) 120W at 700 mm/s. The other samples were sintered with 160W powder and d) 400 mm/s, e) 500 mm/s and f) 600 mm/s*.

The SLS processed GO@Cu lines were characterized with SEM, as shown in Fig. 12 in which each image corresponds to a stripe in the array shown in Fig. 10. Among the samples, the lowest degrees of porosity are demonstrated in lines a) and d), correlating to the visual inspection in Fig. 10. Although these samples still exhibit some degree of porosity, the heat transfer was sufficient to almost liquify the substrate layers between depositions, resulting in a denser structure. In lines b), c), e) and f) this layer morphology is absent as the spherical features of underlying layers are noticeable.

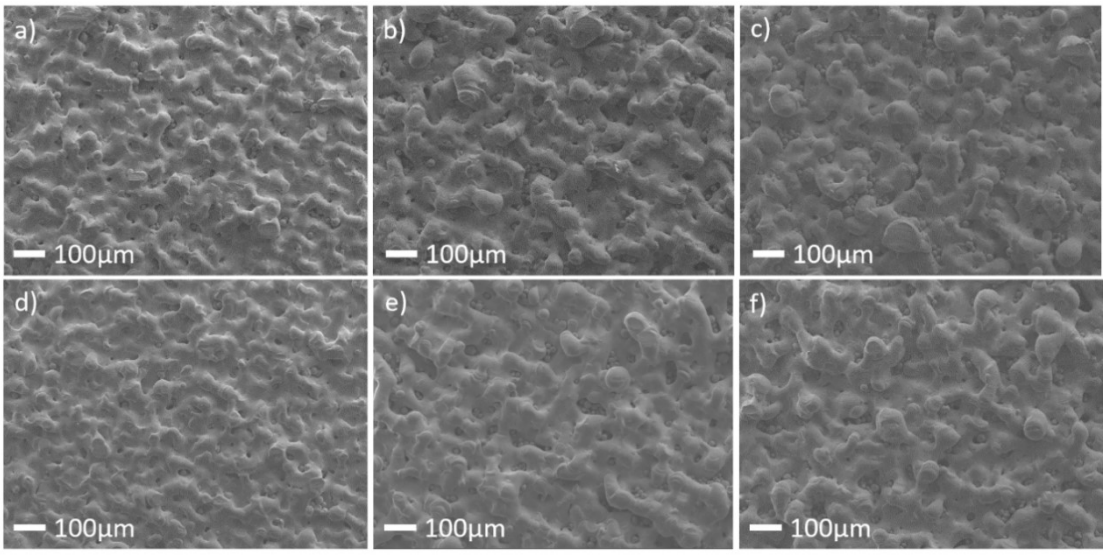

Fig. 12: *SEM images of the GO@Cu powder sintered with SLS. The GO@Cu powders in the top row were sintered with 700 mm/s scan speed and a) 160W, b) 140W and c) 120W laser power. The lower row was sintered at 160W and d) 400 mm/s, e) 500 mm/s and f) 600 mm/s scan speed*

After SLS processing, the surfaces of the lines sintered at 100W and 160W power and 700 mm/s scan speed were gently sandpapered to deform GO, thus making it readily identifiable by SEM. In particular, large amounts of GO were found on the line shown in Fig. 10c). As shown in Fig. 15a), which depicts the surface of GO@Cu sintered at 100W and 700 mm/s scan speed, the remaining GO consist of multilayers that has deformed and wrinkled during sintering. Several sites on this line were inspected by SEM and similar coating integrity was observed. In the background of Fig. 15a), spherical nanoparticles are decorating the sintered surface. Energy dispersive spectrometry (EDS) reveal that the spherical artefacts shown in the background of Fig. 13a) contain ~70% Cu, 25% carbon and ~5% oxygen. Considering this, the 50-100 nm sized artefacts are likely copper oxide precipitates originating from the liquified outer particle surface. In Fig. 13b), only trace amounts of GO could be identified on the surface by SEM, as evidenced by wrinkling. However, as indicated by the arrows, some particles contained large, damaged GO sheets.

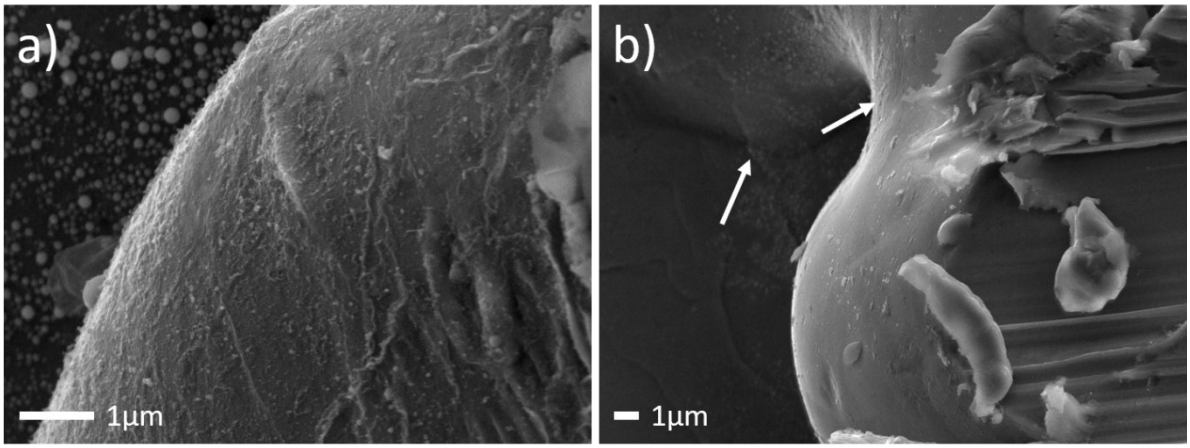

Fig. 13: *SEM images of GO@Cu sintered with SLS at a) 100W and b) 160W power, after abrasion with sandpaper. The scan speed was 700mm/s in both cases. Arrows indicate areas with trace amounts of GO.*

In short, the inspection has confirmed that GO is retained on the 0.625wt‰ GO@Cu after laser sintering at 100W and 160W powder. Further surface analysis of both sintering lines was performed with Raman in order to assess the quality of the remaining GO. As shown in Fig. 14a) and 14b), laser sintering of GO@Cu at 100W and 700 mm/s does not remove GO from the particle surfaces. Rather, in Fig. 14c), the appearance of a small 2D band at ~2600cm^{-1} and ratio $1 < I_D/I_G$ suggests that the laser thermally reduced the coating and that the remaining layer may have pyrolyzed to damaged graphene. The appearance of a small 2D band implies that few layers of graphene remains on the sintered surface. Furthermore, the Raman spectrum was measured at the center of the sintered particle, shown in Fig. 14b), where the intensity counts were not the highest. Hence, the remaining graphene covers most of the particle and has not exfoliated the coating from the Cu substrate.

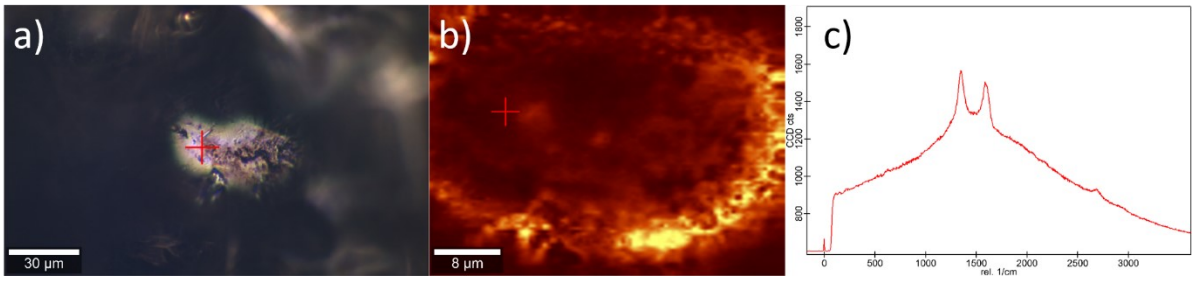

Fig. 14: *Raman of GO@Cu sintered with SLS at 100Wand 700 mm/s, showing a) optical microscopy image, b) G band Raman mapping and c) spectrum measured at the red marker.*

Interestingly, increasing the laser power to 160W is sufficient to augment this reduction. Another Raman inspection of the area in Fig. 15a) yielded the G band mapping shown in Fig. 15b). As seen in the optical image, there are no visible graphitic layers on the sintered Cu surface, which would appear as dark spots. Rather, the Raman mapping in Fig. 15b) shows that the surface coverage and G band intensity has significantly increased. Interestingly, the length of several graphene sheets is close to 10µm, which is the average sheet length in the original GO dispersion. This would suggest that the SLS process at 160W is not detrimental to the sheet size of the coating. Moreover, Fig. 18c) shows that at 160W laser intensity, the Raman spectrum demonstrates increased counts for the G and 2G bands. Specifically, the I_D/I_G and I_{2D}/I_G ratios improve to 0.66 and 0.49, respectively. Although this still constitutes few-layered graphene, this can be explained by the increased laser intensity having an annealing effect on the sp^2 graphene lattice.

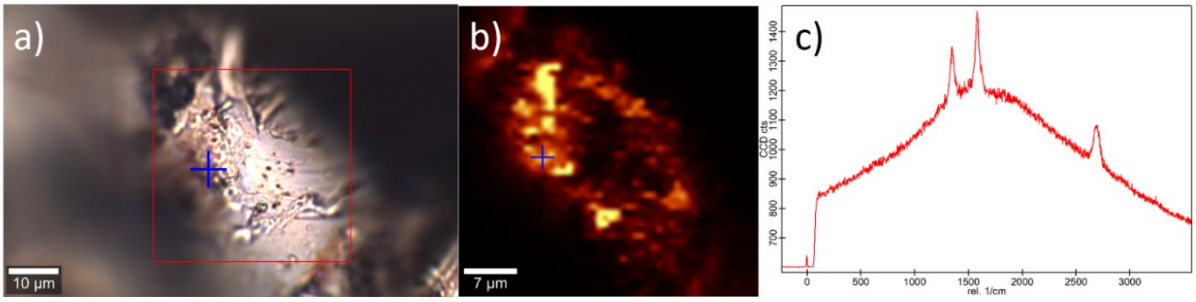

Fig. 15: *Raman of GO@Cu sintered with SLS at 160W and 700mm/s, showing a) optical microscopy image, b) G band Raman mapping and c) spectrum measured at the red marker.*

4. Conclusion

Furthermore, the results obtained from selective laser sintering of GO@Cu indicate that even a modest GO loading (0.625wt‰) can significantly reduce sample porosity, by virtue of its *in situ* reduction to rGO over a range of laser intensities (120W-160 W). The high light absorbance and low thermal conductivity (~30W/mK) of p-GO@Cu helps localizing energy from the impinging laser before reduction. Both SEM and Raman inspection verified the preservation of the coating after laser sintering, as well as the appearance of characteristic 2D bands, the highest of which was obtained after laser sintering at 160W powder. The increased densification is attributed to a reduction in energy loss due to a combination of raised thermal conductivity and reduced laser scattering caused by rGO.

These results demonstrate the viability of thermally conductive rGO@Cu composite powders obtained via surface charge modification of Cu with APTES. The flexibility of this synthesis process means it can be adapted for production of both conventional metal matrix composites, as well as composite metal powders for additive manufacturing. In particular, the reduced energy loss in laser additive manufacturing opens new possibilities for laser sintering of complex geometries with reflective metal powders.

Acknowledgements

The authors gratefully acknowledge the received funding from the European Union's Horizon 2020 research and innovation program under GrapheneCore2 785219 – Graphene Flagship.

References

1. Sidhu, S. S., Kumar, S. & Batish, A. Metal Matrix Composites for Thermal Management : A Review. *Crit. Rev. Solid State Mater. Sci.* **8436**, 132–157 (2016).

2. Hu, Z. *et al.* Graphene-reinforced metal matrix nanocomposites - A review. *Mater. Sci. Technol. (United Kingdom)* **32**, 930–953 (2016).

3. Ikeshoji, T., Nakamura, K., Yonehara, M., Imai, K. E. N. & Kyogoku, H. Selective Laser Melting of Pure Copper. *JOM* **70**, 396–400 (2018).

4. DeBroy, T. *et al.* Additive manufacturing of metallic components – Process, structure and properties. *Progress in Materials Science* vol. 92 112–224 (2018).

5. Liu, R., Wang, Z., Sparks, T., Liou, F. & Newkirk, J. *Aerospace applications of laser additive manufacturing*. *Laser Additive Manufacturing* (Elsevier Ltd, 2017). doi:10.1016/B978-0-08-100433-3.00013-0.

6. Palermo, V., Kinloch, I. A., Ligi, S. & Pugno, N. M. Nanoscale Mechanics of Graphene and Graphene Oxide in Composites : A Scientific and Technological Perspective. *Adv. Mater.* **28**, 6232–6238 (2016).

7. Balandin, A. A. *et al.* Superior Thermal Conductivity of Single-Layer Graphene 2008. *Nano Lett.* **8**, 902–907 (2008).

8. Novoselov, K. S. *et al.* Electric field effect in atomically thin carbon films. *Science (80-.).* **306**, 666–669 (2004).

9. Phiri, J., Gane, P. & Maloney, T. C. General overview of graphene : Production , properties and application in polymer composites. *Mater. Sci. Eng. B* **215**, 9–28 (2017).

10. Sakai, T. & Hirono, M. Laser welding of highly reflective metal with absorbance - enhanced surface structure fabricated using picosecond laser. *Appl. Phys. A* **126**, 1–8 (2020).

11. Fai, K., Ju, L., Wang, F. & Heinz, T. F. Optical spectroscopy of graphene : From the far infrared to the ultraviolet. *Solid State Commun.* **152**, 1341–1349 (2012).

12. Malouf, A. & Henderson-sapir, O. Two-photon absorption and saturable absorption of mid-IR in graphene. *Appl. Phys.* **091111**, 6–11 (2019).

13. Pontevedra, T. Conventional and Additive Manufacturing with Metal Matrix Composites: A Perspective. *Procedia Manuf.* **30**, 159–166 (2019).

14. Chu, K. *et al.* Largely enhanced thermal conductivity of graphene/copper composites with highly aligned graphene network. *Carbon N. Y.* **127**, 102–112 (2018).

15. Kumar, H. G. P. & Xavior, M. A. Graphene Reinforced Metal Matrix Composite (GRMMC): A Review. *Procedia Eng.* **97**, 1033–1040 (2014).

16. Hu, Z. *et al.* Laser additive manufacturing bulk graphene-copper nanocomposites. *Nanotechnology* **28**, 1–9 (2017).

17. Yue, H. *et al.* Effect of ball-milling and graphene contents on the mechanical properties and fracture mechanisms of graphene nanosheets reinforced copper matrix composites. *J. Alloys Compd.* **691**, 755–762 (2017).

18. Belyaeva, L. A. Wettability of graphene. *Surf. Sci. Rep.* **75**, 1–9 (2020).

19. Liang, A. *et al.* Recent Developments Concerning the Dispersion Methods and Mechanisms of Graphene. *Coatings* **8**, 1–23 (2018).

20. Chen, F. *et al.* Effects of graphene content on the microstructure and properties of copper matrix composites. *Carbon N. Y.* **96**, 836–842 (2016).

21. Yang, Y. *et al.* Ag/graphene composite based on high-quality graphene with high electrical and mechanical properties. *Prog. Nat. Sci. Mater. Int.* **29**, 384–389 (2019).

22. Hu, Z. *et al.* Laser sintered single layer graphene oxide reinforced titanium matrix nanocomposites. *Compos. Part B* **93**, 352–359 (2016).

23. Lin, D., Richard Liu, C. & Cheng, G. J. Single-layer graphene oxide reinforced metal matrix composites by laser sintering: Microstructure and mechanical property enhancement. *Acta Mater.* **80**, 183–193 (2014).

24. Suk, J. W., Piner, R. D., An, J. & Ruoff, R. S. Mechanical Properties of Monolayer Graphene Oxide. *ACS Nano* **4**, 6557–6564 (2010).

25. Wu, Y. *et al.* Graphene oxide / Al composites with enhanced mechanical properties fabricated by simple electrostatic interaction and powder metallurgy. *J. Alloys Compd.* **775**, 233–240 (2019).

26. Gao, X. *et al.* Mechanical properties and thermal conductivity of graphene reinforced copper matrix composites. *Powder Technol.* **301**, 601–607 (2016).

27. Gan, C., Liang, T., Li, W., Fan, X. & Zhu, M. Applied Surface Science Amine-terminated ionic liquid modified graphene oxide / copper nanocomposite toward efficient lubrication. *Appl. Surf. Sci.* **491**, 105–115 (2019).

28. P. Mellin P. Harlin, H. Brodin, H. Blom, and A. Strondl, O. L. Evaluating flowability of additive manufacturing powders, using the Gustavsson flow meter. *Met. Powder Rep.* **72**, 322–326 (2017).

29. Kvetkova, L. Fracture toughness and toughening mechanisms in graphene platelet reinforced Si 3 N 4 composites. **66**, 793–796 (2012).

30. Wang, J. *et al.* Effect of the graphene content on the microstructures and properties of graphene / aluminum composites. *New Carbon Mater.* **34**, 275–285 (2019).

31. Li, J., Zhang, X. & Geng, L. Improving graphene distribution and mechanical properties of GNP / Al composites by cold drawing. *Mater. Des.* **144**, 159–168 (2018).

Paper II

Dual anticorrosion protection of Cu by silanes and graphene with controlled thickness

K. H. Martinsen, J. Sun, Z. Xia, A. Kovtun, U. Klement, E. Hryha, L. Nyborg, V. Palermo

In manuscript

Dual anticorrosion protection of Cu by silanes and graphene with controlled thickness

K. H. Martinsen[a], J. Sun[a,*], Z. Xia[a], A. Kovtun[b], U. Klement[a], E. Hryha [a], L. Nyborg[a], V. Palermo[a,b]

[a] Department of Industrial and Materials Science, Chalmers University of Technology, Gothenburg 412 58, Sweden

[c] Institute of Organic Synthesis and Photoreactivity (ISOF), CNR, via Gobetti 101, 40129, Bologna, Italy.

Abstract

Herein, we investigate a scalable and facile solution mixing approach to creating a composite powder of Cu with dual corrosion protection from graphene oxide (GO) and 3-aminopropyltrietoxysilane (APTES). X-ray photospectrometry of surface modified particles confirmed covalent bonding between Cu and APTES, which acted as a molecular scaffold for GO by electrostatic interaction with protonated amine. Scanning electron microscopy and Raman showed that the thickness of adsorbed GO correlated with APTES concentration. This controllable surface morphology meant up to 70% composite mass could be preserved after 3 hours in ammonium persulfate. Moreover, sintered composites preserved up to 50% mass after 300 hours in 37% HCl. Polarization of composite green bodies demonstrated corrosion currents comparable to Cu, though the corrosion potential of all composite samples were 0.12V to 0.15V higher. Thermal reduction of composite powder before sintering improved hydrophobicity and shifted the corrosion potential of the outer surface to 0.9V while lowering the corrosion current from $5.31*10^{-6}$ A/cm^2 to $3.86*10^{-7}$ A/cm^2. The composite powders demonstrate good chemical and thermal stability, which make them viable for production of corrosion resistant metal composites through powder metallurgy processes and additive manufacturing.

***Corresponding author**:

E-mail address: jinhua@chalmers.se (Jinhua Sun)

Keywords:

Copper powder, graphene oxide, APTES, surface modification, anticorrosion, metal composite.

1. Introduction

Corrosion is a big issue for the metal-based products and systems operating in ambient environments. The total cost of corrosion in the world is estimated to have reached about 2.5 trillion US dollar several years ago. Various strategies of corrosion prevention have been developed to address this issue, for example by employing a protective coating of polymers, oxide layers or alloys. In this regard, the coating materials play a critical role on the anticorrosion performance and lifetime of underlying metal. The widely used polymer based anticorrosion coating is usually thick (in millimeter scale), as the protective efficiency is proportional to its thickness. Moreover, a thick coating is required to lower the risk of leakage due to the presence of micropores formed during solvent evaporation.

Graphene is considered the thinnest and the most promising coating materials for anticorrosion owing to its combined properties of monoatomic thickness and excellent impermeability to all gases and ions (except for H^+)[1]. As an additive to improve the existing polymer based anticorrosion coating, it has been reported that incorporating 30-40nm graphene layer into polyethylenimine (PEI) can dramatically reduce the oxygen transmission rate to 0.05cc/m^2 per day[2]. Recently, we demonstrated that aligning 25 layers graphene between PEI with only 92nm in thickness gave a 96% reduction of oxygen transmission rate, while pure PEI does not inhibit oxygen diffusion[3]. However, as a solo protective coating materials, in terms of anti-oxidation, it has been demonstrated that the as-grown chemical vaper deposition (CVD) single layer graphene on Cu surface not only failed to protect underlying Cu from oxidation, but also accelerated corrosion of copper in the long-term. This was attributed to the high conductivity of graphene which can cause the galvanic corrosion by forming an electrochemical circuit with the Cu, similar to contacting graphite with metal[4].

In addition, the boundaries of single layer CVD graphene sheets are polycrystalline defects that allow penetration of corrosive or otherwise aggressive species. Such defects delimit the efficacy of the graphene/Cu interface as the governing inhibitor of the corrosion process. If the protective graphene coating is damaged or otherwise incomplete, the corrosion would extend along the horizontal direction with the diffusion of oxygen, thus leading to severe crevice corrosion of Cu[5]. As an exception, the oxidation and corrosion of underlying Cu can be completely inhibited by growing monocrystalline graphene on Cu (111) as compare with Cu (100). This is because strong interfacial coupling with graphene/Cu(111) prevents H_2O diffusion into the graphene/Cu(111) interface[1]. However, it is challenging to achieve adequate and large-scale graphene coating on arbitrary metals for practical applications, as they are rarely monocrystalline nor bond well with graphene. Roy et al.[6] showed an alternative strategy which involved stacking multilayer CVD graphene, forming a sufficiently thick diffusion barrier to inhibit the penetration of oxygen through crevices and grain boundaries. Stacking multiple layers had a multiplicative effect on corrosion protection due to diffusion becoming increasingly tortuous. However, it is rather complicated to transfer and stack CVD graphene without forming wrinkles and defects, which can compromise the efficacy of the protective layer.

One approach to reaching a thin coating of graphene on a substrate is to use organic-inorganic compounds like silanes, which can self-assemble to form a monomolecular scaffold. Such self-assembled layers of silane have been much used to engineer the surface properties of substrates like Si wafers, as the organic functional group on the other side of silane can be hydrophobic or hydrophilic depending on its dipolarity[7],[8]. In the same way, after hydrolysis, the silanol groups can covalently bond to the metal surface via condensation reactions[9].

While a self-assembled monolayer of silane can improve corrosion protection, there are some limitations. Abrasion or incomplete self-assembly can reveal the metal substrate, which can subsequently become critical weak points that are susceptible to severe pitting corrosion[10]. To counter this, silane-polymer hybrid layers can dramatically improve anticorrosion performance and enhance adhesion to the substrate[11]. However, since formation of micropores in hybrid coating layers is difficult to prevent during solvent evaporation, corrosive species may still permeate through a network of microcavities and cause delamination of the layers by attacking the metal surface oxide. Therefore, new coating strategies must simultaneously prevent diffusion to the metal substrate and passivate it.

Previous work by others have attempted to solve this issue by applying a composite coating consisting of a silane and graphene oxide (GO)[12]. However, while the composite coating can significantly improve corrosion resistance, the methods often involve small scale electrodeposition or even manual application due to poor electrical conductance[13]. This approach was used by Raza *et al*.[14] to electrodeposit a GO protective coating followed by a dip-coating with silane, which resulted in a composite coating with significantly lower corrosion current and a positive shift in corrosion potential. However, it would be advantageous to combine this dual corrosion resistance provided by GO and silane with a more scalable and industrially relevant process.

To this end, powder metallurgy provides an interesting angle. With recent advances in additive manufacturing technologies, powder metallurgy has transitioned from use conventional processes like hot-rolling, extrusion and press-and-sinter to novel production of highly complex metal components via laser sintering. This process flexibility would allow a composite GO-Cu (GO@Cu) powder to not only benefit from graphene as a corrosion inhibitor, but also as a reinforcing filler which can improve tensile strength, heat conductivity and even electrical conductance[15]–[17].

In this work, a novel method for engineering a uniform, dual coating of GO on Cu was explored. A surfactant molecule 3-aminopropyltriethoxysilane (APTES) was grafted onto Cu in toluene to bestow a net positive surface charge via hydrolyzation of terminating amine functional groups. Using an anhydrous solvent limited the self-polymerization of APTES and allowed better control of the surface grafting. This synthesis of surface-modified Cu (APTES@Cu) was followed by a facile, scalable and quick solution mixing process with commercially available GO to create a composite powder of Cu with a comprehensive GO coating (GO@Cu). The synthesized GO@Cu composites were characterized with SEM and Raman to evaluate how the APTES concentration and surface treatment duration can influence the coating morphology and thickness. SEM was also employed to compare the fracture surfaces of sintered GO@Cu and reduced graphene oxide (rGO@Cu) composites. The thermal stability of GO@Cu powders with thin and thick coatings was investigated with thermogravimetric

analysis (TGA). Finally, the corrosion resistance of the samples was evaluated by corroding sintered samples in 37vol% HCl, composite powders in 0.5M ammonium persulfate (APS) and by polarization measurements of both compressed green bodies and sintered samples.

2. Experimental

2.1. Materials

Polycrystalline, gas atomized copper powders were purchased from Carpenter (99.9% purity, 34 μm mean diameter) under the product name MIM 270M ± 15μm. Toluene (98% purity) and HCl (37vol%) were purchased from VWR, while 3-aminopropyltriethoxysilane (99% purity) and ammonium persulfate (APS) were purchased from Sigma-Aldrich. Graphene oxide (0.4wt%, 10μm mean lateral size, 41-50% O) was purchased from Graphenea.

2.2. Preparation of GO@Cu composite powders

Copper powder was first rinsed once with toluene to remove impurities on the particle surface before transfer to a beaker. 10g rinsed Cu powder was then added to 100ml fresh toluene and kept suspended by magnetic stirring. A volumetric percentage of APTES was added to this solution depending on the target thickness of the GO coating. Some samples were heated with an electric plate for the duration of the APTES@Cu synthesis – water bath was not used. Low APTES concentrations and short treatment durations were used to synthesize GO@Cu composites with thin coatings, whereas higher APTES concentrations and extended treatment durations were used to create composites with thicker GO coatings. After synthesis of the Cu grafted with APTES (APTES@Cu), the powder was rinsed three times with fresh toluene. The rinsed APTES@Cu powder was then dried at ambient conditions. In a separate beaker, GO was well diluted in 500ml DI water and sonicated for 1 hour. GO@Cu composite powder was then synthesized by adding the sonicated GO dispersion to APTES@Cu suspended in 100ml magnetically stirred DI water. The solution was kept stirring for 20 seconds until the dispersed GO had coated the APTES@Cu, leaving a supernatant solution. After removal of the supernatant, the GO@Cu powder was rinsed with deionized water once before drying under low temperature overnight.

Table 1 below summarizes the parameters used in synthesizing the GO@Cu powders in this work.

Table 7: Summary of synthesized samples

Sample name	GO	APTES	Duration	Temperature
GO@Cu-1	33 wt‰	6.25 vol%	15 hours	RT
GO@Cu-2	0.625 wt‰	2.5 vol%	15 hours	60 °C
GO@Cu-3	0.25 wt	0.2vol%	30 min	50 °C
GO@Cu-4	0.625 wt‰	0.2vol%	30 min	RT
GO@Cu-5	1 wt‰	2.5vol%	30 min	RT
0.1%-GO@Cu-7	1 wt‰	0.1 vol%	8 hours	RT
0.3%-GO@Cu-7		0.3 vol%		
0.5%-GO@Cu-7		0.5 vol%		
0.8%-GO@Cu-7		0.8 vol%		
1.5%-GO@Cu-7		1.5 vol%		
GO@Cu-8	1 wt‰	0.5 vol%	8 hours	RT
GO@Cu-9	1 wt‰	0.8 vol%		

A subset of these samples was reduced to rGO@Cu by thermal annealing in a ceramic tube furnace with target temperature 400 °C and 2 hours duration. The heating rate was 5 °C/min and the furnace was kept in an inert atmosphere by continuously flushing with argon at 8 cm^3/min. Reduced samples were extracted once the furnace temperature was below 60 °C.

2.3. Preparation of sintered GO@Cu composites

Both rGO@Cu and GO@Cu samples were consolidated into 1 cm diameter disks by uniaxial, hydraulic compression in a die mould under 1.25 GPa pressure. This was followed by sintering in a ceramic tube furnace at 1050°C for 4 hours in argon atmosphere with 8 cm^3/s flow rate. Sintered GO@Cu (s-GO@Cu) or rGO@Cu (s-rGO@Cu) samples were extracted once the furnace had cooled below 80 °C.

2.4. Polarization measurements

The corrosion properties of Cu and GO@Cu samples were evaluated with polarization in a 700ml solution of 3.5wt% NaCl. Both green bodies and sintered samples were used, and the diameter of the corroding surface was 0,5 cm. The scan rate was 5mV/s and the equalization of open circuit voltage (OCV) was run for 20 minutes prior to polarizing each sample, and the electrochemical cell was rinsed with DI water and then the NaCl solution after each measurement. The potentiostat was interfaced with the CorrWare software.

2.5. Etching in ammonium persulfate (APS) and hydrochloric acid

A subset of GO@Cu and rGO@Cu powders where immersed in corrosive solutions to investigate the anticorrosive properties of GO and rGO. Cu was used as a reference sample.

For both GO@Cu and rGO@Cu, 0.3g of powder were etched in sealed vials with 10ml of 0.5M APS solution. Special care was taken to prevent smudges and other contaminants from affecting the weight of the vials. The vials were gently shaken every 30 minutes to redisperse the solution. After 3 hours the APS etchant was removed from each sample, and the corroded powders were gently rinsed 5 times with DI water by using a pipette. Rinsed samples were vacuum dried at room temperature in a Buchi oven for 3 hours and then weighted by subtracting the weight of the sample vial.

Sintered rGO@Cu and GO@Cu samples of 0.5g average weight were immersed in 10ml of 37vol% HCl in sealed vials. The vials were gently shaken once per day to redisperse the solution, and the corroding samples were extracted once per day for weight measurement. Before weighing, the samples where gently rinsed with DI water and blow dried with compressed air. The total duration of the corrosion in 37vol% HCl was 220 hours.

2.6. Characterization methods

SEM (JEOL JSM-7800F Prime) was used at 5 kV and 10 mm working distance to inspect how the GO morphology and coverage on GO@Cu powders are influenced by APTES concentration, GO concentration and APTES treatment duration. It was also employed to evaluate the fracture morphology, sample density and the preservation of GO/rGO in sintered samples. Gold sputtering was not employed to increase surface conductivity and to prevent electron charge buildup, since this could compromise the GO features at higher magnification. This surface characterization was further expanded with Raman spectrometry performed with a WITec alpha300R operating with a 532 nm Nd:YAG laser. Mapping with respect to the G band was performed on GO@Cu green bodies to evaluate how APTES concentration influences the coverage of GO. In addition, point analysis was performed on cross sections of sintered GO@Cu samples to characterize the coating in the core of the composite.

Thermogravimetric analysis (NETZSCH TG 209F1) was carried out on Cu and GO@Cu powders with a 10 ºC/min heating rate in nitrogen atmosphere to investigate the thermal stability of APTES and GO. The target temperature was 1000 °C and no isotherm was used.

XPS measurements were performed on GO@Cu powder with a PHI VersaProbe III operating with a monochromated Al Ka anode (1486.6 eV).

3. Results

3.1. Synthesis of GO@Cu with thin GO coating

Figure 1 shows GO@Cu powder synthesized with by grafting 0.2vol% APTES to Cu for 30 minutes before drying and addition of 0.25wt‰ GO. As shown in the low magnification SEM image in Fig. 1a), all particles are isolated and no clusters can be observed. Closer inspection of a single particle in Fig. 1b) reveals that the particle surface has no visible artefacts in the form of micron-sized GO sheets, nor any extensive damage to the particle surface which could be caused by the solution mixing process. At this magnification level, GO is difficult to be identified. However, 20000x magnification of the inset area in Fig. 1b) allows more features of the GO coating to be clearly discerned. The GO coating in this area, shown in Fig. 1c), is so thin that it does not significantly obfuscate features like depressions or furrows on the Cu particle substrate. The coating itself was identified by noticing folds and ripples of less than 50 nm size distributed over the ~5 μm surface area. In Fig. 1c), some of these folds are pinpointed with white arrows.

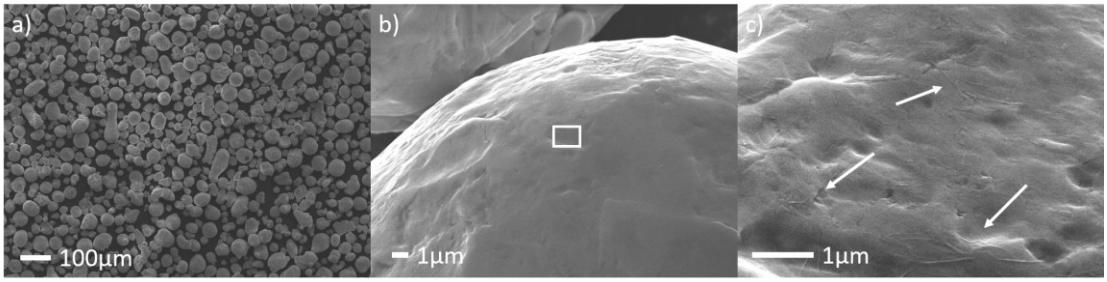

Figure 1: *GO@Cu powder synthesized with 0.2wt‰ GO and 0.2vol% APTES for 30 minutes.*

A similar result was obtained by maintaining the synthesis parameters like APTES concentration (0.2vol%) and APTES treatment duration (30 minutes) while increasing the GO concentration from 0.25wt‰ to 0.625wt‰. In fact, Fig. 2a) shows that this increase in GO concentration only caused a marginal increase in frequency of GO@Cu clusters. Fig. 2b) is a magnified image of one such cluster, which shows that rather than completely enveloping several particles at the same time, the clustering is caused by strands or sheets connecting vicinal GO@Cu particles. Like for the previous sample in Fig. 1, Fig. 2b) shows that the features of the GO coating are difficult to observe at this magnification and that the coating morphology was not visibly affected by the increase in GO concentration. Besides the slight increase in formation of clusters, the white arrows in the image also show that several GO@Cu particles were decorated with 1-3 μm APTES@Cu or GO@Cu artefacts. Each of these surface artefacts are spread throughout the surface of the host GO@CU particle and are enveloped in GO. This is

discernable by identifying contrasting silhouettes surrounding the artefacts, which are suspended, thin GO sheets obfuscating the underlying Cu. One such enveloped particle was found at the intersection between two GO@Cu particles in the inset area in Fig. 2b). A higher magnification of this particle is shown in Fig. 2c), which also shows that the stretched GO coating is so thin as to be nearly transparent to the 5kV electron beam. In addition, the same magnification shows that this GO stems from the surface of the larger particle.

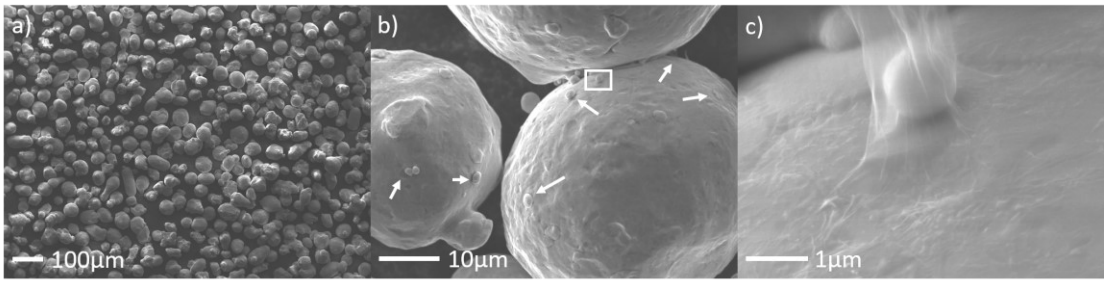

Figure 2: *GO@Cu powder synthesized with 0.625wt‰ GO and 0.2% APTES for 30 minutes.*

A similar coating morphology was obtained by increasing the GO concentration to 1wt‰ and the APTES concentration to 2.5vol% while maintaining the APTES treatment duration at 30 minutes. Fig. 3a) shows a SEM image of several GO@Cu particles synthesized with these parameters. Like the preceding GO@Cu samples, the clustering between GO@Cu particles was minimal and the GO coating was so thin as to being undetectable at low magnification. This is exemplified by the arrows in Fig. 2b) which show locations with GO only detectable in the form of folds or sheets covering surface features on the GO@Cu particle. Despite using increased GO and APTES concentration in synthesizing this sample, the resultant GO coating has a thickness comparable to the previous samples shown in Fig. 1 and Fig. 2. Fig 3c) is a magnification of the inset area in Fig. 2b) and shows that the surface features of Cu are clearly visible. The spherical object beneath the thin GO coating are nucleating surface oxides.

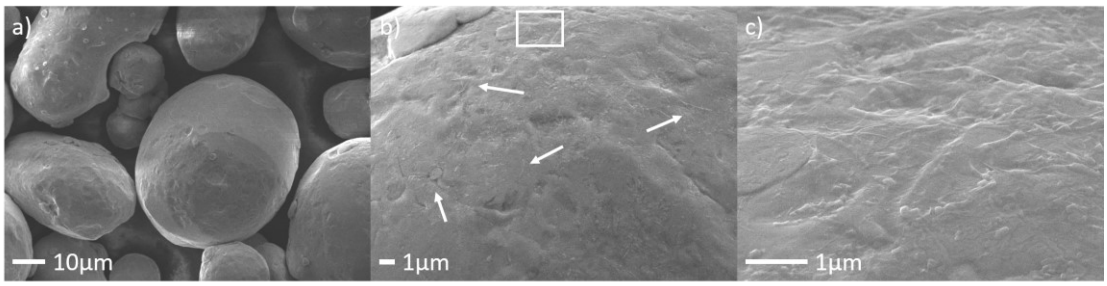

Figure 3: *GO@Cu powder synthesized with 1wt‰ GO ratio and 2.5vol% APTES for 30 minutes.*

3.2. Synthesis of GO@Cu with thick GO coating

The first attempt at synthesizing GO@Cu powders with a thick GO coating is shown in Fig. 4. The well-defined particles shown in Fig. 4a)-4c) are from the same sample batch synthesized with 6.25vol% APTES for 15 hours followed by coating with 33wt‰ GO. All three particles are completely coated with an amalgam of GO layers, which results in the outer layers being only loosely attached to the particle and therefore prone to flaking off. Based on the protruding GO sheets shown in Fig. 4b) and 4c), the outer GO sheets are estimated to have a thickness of 500 nm. It should be mentioned that the particles shown in Fig. 4 do not accurately represent the quality of the sample batch as a whole, but rather represent the coating morphology and GO thickness on GO@Cu samples which did not form clusters. In fact, the powder consisted of dozens of superclusters consisting of 20 to 30 GO@Cu particles bound together by overlapping GO sheets.

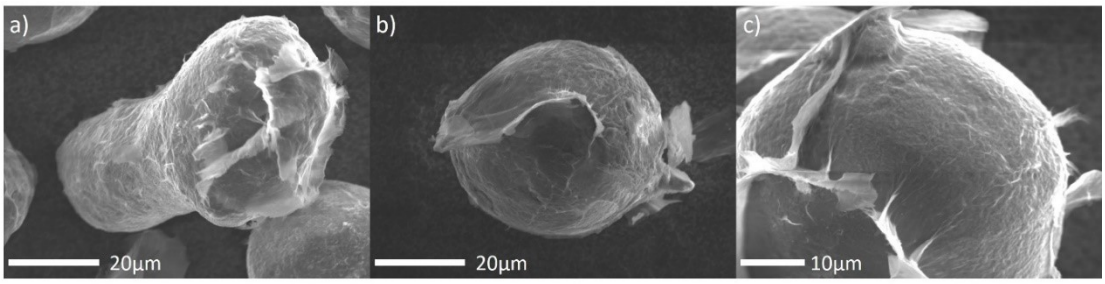

Figure. 4: *GO@Cu powder synthesized with 33wt‰ GO and 6.25vol% APTES for 15 hours. Each image originates from separate GO@Cu particles from the same sample batch.*

The next sample was synthesized with lower APTES and GO concentration for better control of the coating process. Fig. 5a) shows that the GO@Cu powder synthesized with 2.5vol% APTES and 0.625wt% GO exhibited no appreciable degree of clustering and that the GO coating had not delaminated from the particle surfaces. Closer inspection of individual particles, like the one in Fig. 5b), reveals that the GO@Cu particles were completely covered with GO. The white arrows in the image pinpoint areas that exhibit attached GO sheets visible at low magnification. As shown in the figure, areas with visible GO coating encompassed most of the particle surface, indicating that this synthesis procedure was adequate to achieve a comprehensive coating without clustering. A closer inspection of the inset area in Fig. 5b) is shown in Fig. 5c) and revealed that the outer layer of the coating adheres poorly to the underlying GO, which leads to crumpling and folding.

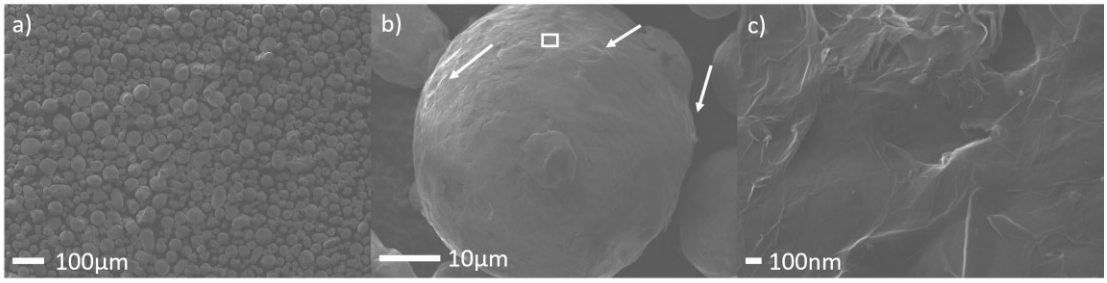

Figure. 5: *GO@Cu powder synthesized with 0.625wt‰ Cu:GO ratio and 2.5vol% APTES for 15 hours. The rectangular area indicated in b) contains the high magnification image c).*

3.3. Synthesis of GO@Cu with scaling APTES concentration

Additional samples were synthesized by maintaining the GO concentration at 1wt‰ and APTES treatment time at 8 hours while changing the APTES concentration. Fig. 6 shows the resulting coating morphologies of samples synthesized with a) 0.1vol% APTES, b) 0.3vol% APTES, c) 0.5vol% APTES, d) 0.8vol% APTES and e) 1.5vol% APTES. No appreciable clustering was observed in any of the samples, hence lower magnification images were not taken. Arrows in the juxtaposed images indicate locations with detectable GO coating.

Compared with the sample in Fig. 5 (0.625wt‰GO, 2.5vol% APTES, 15 hours) it can be seen that all samples synthesized with 1wt‰ GO and 8 hours APTES treatment duration did not attain a thick coating of GO, even with 1.5vol% APTES. For samples synthesized with 0.1% to 0.5% APTES, shown in Fig. 6a) to 6c), thin layers of GO were only detectable under high magnification and by noticing obscured features of underlying Cu, or GO membranes covering surface artefacts in the case of Fig. 6b).

Increasing the APTES concentration to 0.8vol% (Fig. 6d) and 1.5vol% (Fig. 6e) leads to GO cover more of the particle surface, as well as obfuscation of the underlying Cu. This was particularly the case for the sample synthesized with 1.5vol% APTES.

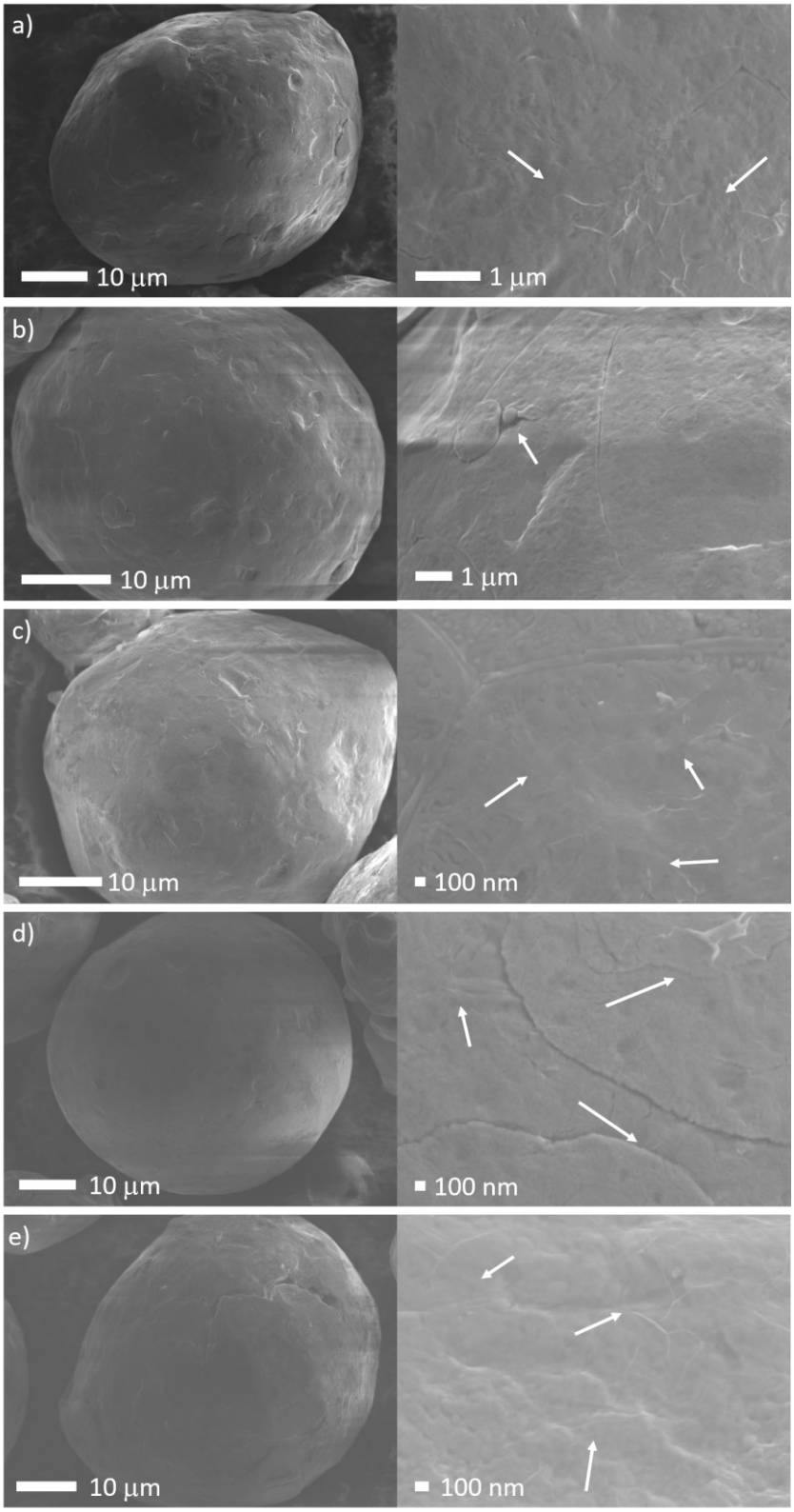

Figure 6: *GO@Cu composite powders synthesized with a) 0.1%, b) 0.3%, c) 0.5%, d) 0.8% and e) 1.5% APTES. Each row corresponds to one sample. The arrows point at regions with detectable GO.*

3.4. XPS

An APTES@Cu powder synthesized with 1vol% APTES was inspected with XPS to analyze the composition of the surface and the integrity of the surface grafting after rinsing and drying. As shown in Fig. 7, both Si 2p peaks (~102 eV) and N 1s peaks (~400 eV) were detected on the rinsed and dried powder along with Cu peaks and O 1s (~525 eV). Although the surface oxides and contaminants on Cu contribute significantly to the C and O peaks, the N and Si peaks stem from APTES. The elemental composition of the surface was not quantified with peak fitting.

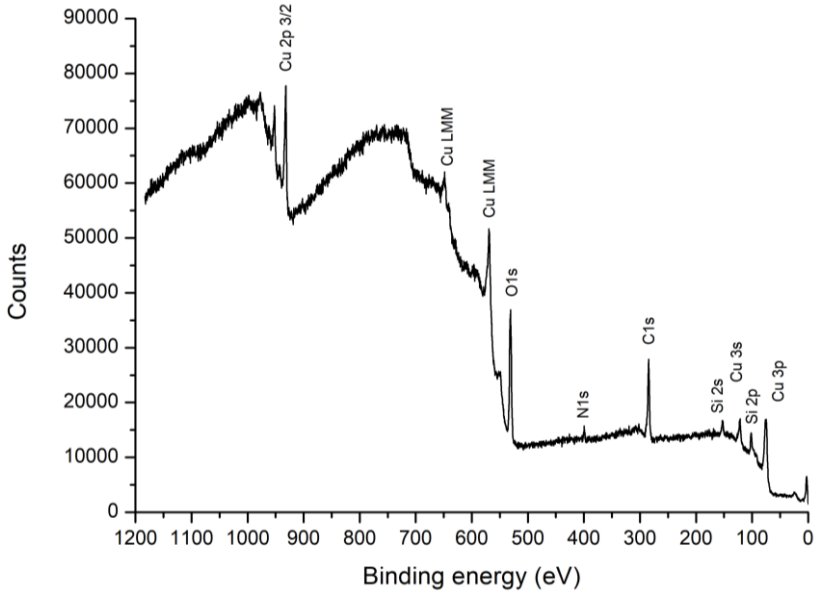

Figure 7: *Wide XPS spectrum of Cu-APTES after rinsing in water. Peaks for N 1s and Si 2p were detected at ~400cm^{-1} and ~102 cm^{-1}, respectively.*

Individual peaks in the survey XPS spectrum shown in Fig. 7 were compared with a reference spectrum. By comparing a Cu 2p peak from pure Cu powder (Fig. 8a)) with Cu 2p from APTES@Cu synthesized with 1vol% APTES, the covalent bonding states change after grafting APTES to the Cu powder. Specifically, the Cu 2p peak in Fig.8a) was found to be a convolution of two peaks originating from $Cu(OH)_2$ at 935.2 eV and CuO/Cu_2O at 933.7 eV. After synthesizing Cu-APTES, the resultant XPS peak in Fig. 8b) show that the $Cu(OH)_2$ peak vanished while a single peak at 934.3 eV was preserved, which can be ascribed to the Cu 2p peak from Cu-O in Cu-O-Si bonds. As shown in Fig. 8c), this peak remained after thorough rinsing with ethanol. Similarly, while no Si 2p peak was found in the reference Cu powder (Fig. 8.d)), it was detected at 102 eV after synthesis of APTES@Cu (Fig. e)). After rinsing with ethanol, the Si 2p count also diminished but was still detected (Fig. 8f)). The diminished peak intensity indicates that some APTES was removed by rinsing, possibly by detaching due to copper surface oxides partaking in alcohol reduction[18]. The coinciding change in Cu 2p bonding mode and detection of Si 2p indicates that APTES covalently bonds with CuO or reacts with $Cu(OH)_2$ via condensation reactions.

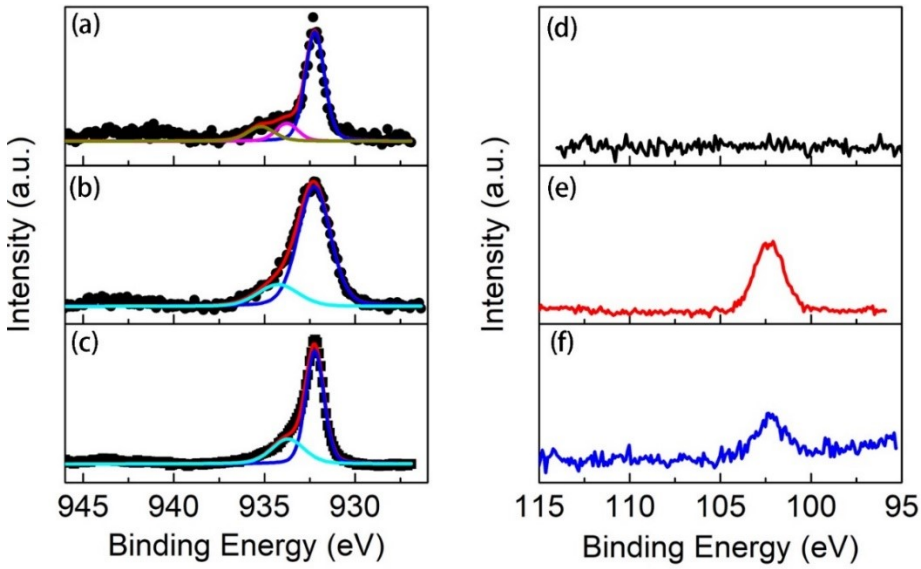

Figure 8. *Cu 2p XPS spectra of a) pure Cu particles, b) Cu-APTES synthesized using 1% APTES solution, and c) Cu-APTES after rinsing. Si 2p XPS spectra of d) pure Cu particles, (e) Cu-APTES synthesized using 1% APTES solution, and (f) ethanol washed Cu-APTES.*

The N 1s signal was strongly bound to ~400 eV binding energy, which is indicative of a covalent C-NH_2 bond. No peak shift towards higher binding energies near 405 eV was observed, meaning that the amine group had not undergone any chemical reaction to form a covalent bond with surface oxides on Cu. Rather, it is known that amine (-NH_2) readily undergoes protonation in weakly acidic, hydrous environments to form -NH_3^+. This means that the remaining APTES on can bestow a net positive surface charge to APTES@Cu in contact with diluted GO, which is acidic and has a net negative surface charge due to the carboxyl functional groups. This negative charge on GO confirmed by measuring a -30mV Zeta potential in our GO dispersion, as shown in Fig. 9. As a result, well-dispersed GO nanosheets in water can rapidly self-assemble on Cu by electrostatic interaction with -NH^{3+} on APTES.

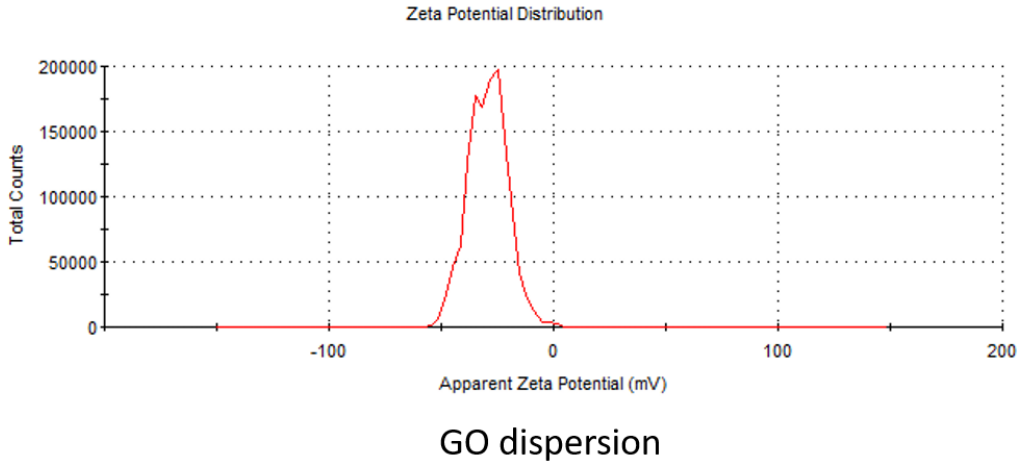

Figure 9. *Zeta potential distribution of GO dispersion used for coating.*

3.5. Synthesis of rGO@Cu by thermal reduction

The sample GO@Cu-2 (0.625wt‰ GO, 2.5vol% APTES) was thermally reduced in a ceramic tube furnace at 400 °C for 2 hours to remove oxygen from the GO coating. Fig. 10 shows the SEM images of two rGO@Cu particles after thermal reduction, with white markers where EDS analysis were performed. Though some parts of the GO coating were damaged or partly exfoliated by the thermal treatment, most of the GO coating is intact and resemble Fig. 10a) and 10b). Like in the previous images in Fig. 1 to Fig. 6, the GO coating can be indentified by wrinkles or contrast against enveloped, 2-3 µm sized particles.

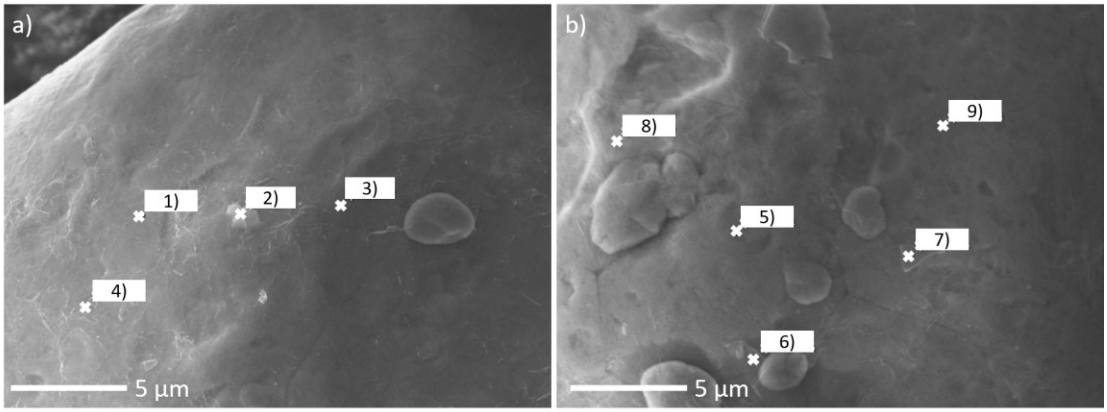

Figure 10: *GO@Cu-2 composite powder after thermal reduction to rGO@Cu-2. The sample was synthesized with 0.625wt‰ GO and 2.5vol% APTES.*

The effectiveness of the thermal reduction in argon atmosphere was evaluated by comparing O/C ratios of original GO from Graphenea against the O/C content found the particles in GO@Cu-2. The elemental composition of each point in Fig. 10 is presented in table 2 and shows that after thermal reduction the average oxygen content is 1.5wt% versus 11.5wt% for carbon. A significant amount of the oxygen content stems from surface oxides on Cu and not from the rGO coating itself, which implies that the actual oxygen content in rGO is lower than 1.5wt%. Regardless, the O/C ratio after thermal reduction is nearly 0.1 and significantly lower than the 0.5 C/O ratio for the original GO. In addition, trace amounts of 0.1-0.2wt% Si from APTES were identified throughout the surface.

Table 8: Elemental composition after thermal treatment

Point	Cu (wt%)	C (wt%)	O (wt%)	Si (wt%)
1)	84.5	14.5	0.9	0.1
2)	85.6	12.8	1.4	0.2
3)	86.1	12.7	1.1	0.1
4)	89.7	9.3	1.0	0.1
5)	88.1	11.1	0.8	N/A
6)	90.3	8.5	1.1	0.1
7)	82.6	14.5	2.7	0.2
8)	88.0	10.4	1.4	0.2
9)	87.0	10.1	2.8	0.2

3.6. Cross section of sintered samples

Sintered samples of Cu and GO@Cu composites were fractured to inspect the fracture morphology. Fig. 11a)-c) shows the cross-section copper sintered at 1050 °C for 4 hours in argon atmosphere. The sample's density was 8.4 g/cm^3 after sintering, or 94% of max density. As expected, the fracture surface has a clear ductile morphology with numerous dimples. Fig. 11b) and Fig. 11c) also show that the 6% porosity is mostly caused by few, large pores originating from decomposition of surface oxides.

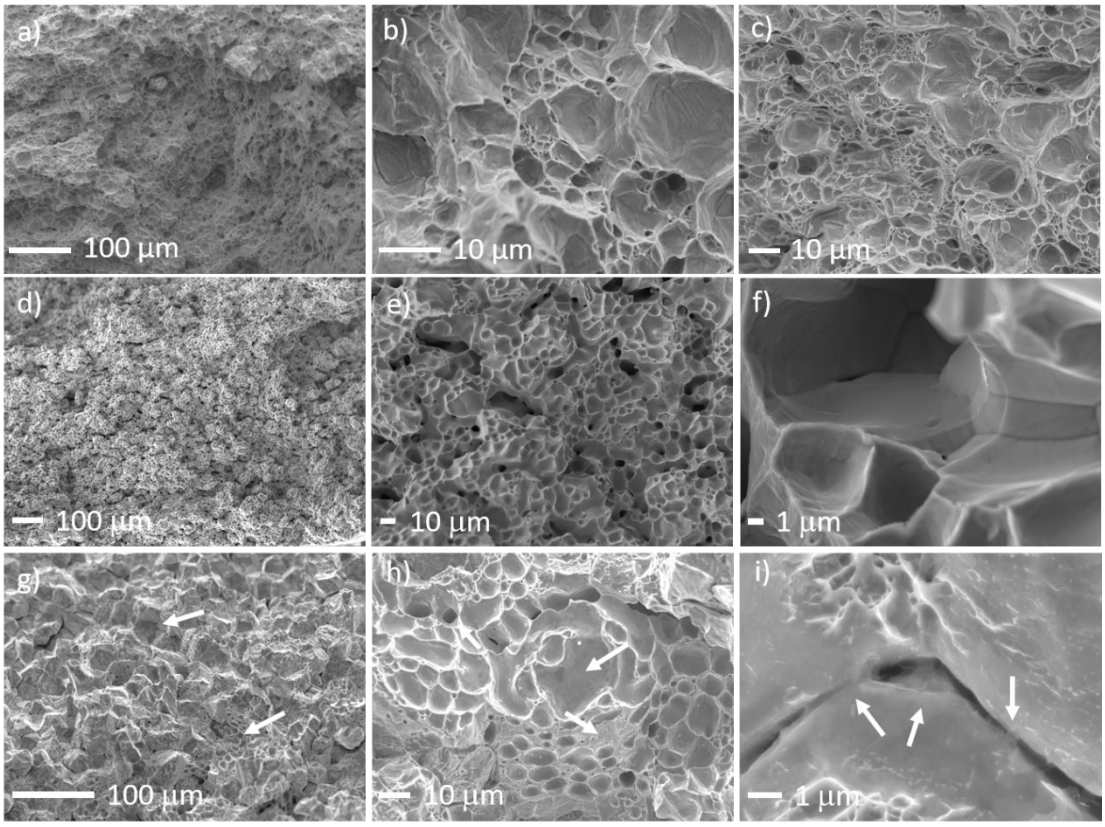

Figure 11: *Cross section of a)-c) sintered Cu, d)-f) sintered GO@Cu-4 and g)-h) sintered rGO@Cu-2.*

In contrast, Fig. 11d)-11f) shows a GO@Cu-4 composite (0.625wt‰G O, 2.5vol% APTES, 30 min) sintered with the same parameters that exhibits a much more porous interior. As shown in Fig. 3, the short APTES treatment time lead to a uniform and thin GO coating for the particles in GO@Cu-4, yet the sintered sample exhibits a low density of only 7.47 g/cm^3. The smoothened surfaces imply that interparticle diffusion has been inhibited, though closer inspection of cavities and depression like the one in Fig. 11f) did not reveal any clear traces of GO remaining in the structure.

In comparison, the sintered sample of thermally reduced powder rGO@Cu-2 (0.625wt‰. 2.5vol%, 15 hours) has a much higher density at 8.7 g/cm^3. As shown in Fig. 11g) to Fig. 11i), the sintered rGO@GO-2 contains rGO@Cu particles that have not fully fused with one another. Smooth areas or sockets are juxtaposed with both porous cavities and regions with rougher surfaces, indicating necking with vicinal particles. In Fig. 11i), closer inspection of the poorly densified Cu-rGO reveal that intact rGO sheets act as bridges between multiple particles. Similarly, the upper and lower parts of the image depict areas with rGO damaged by the fracture. However, the most notable difference between the composite cores in rGO@Cu-2 and GO@Cu-4 is the disparity in density. In other words, even a thin coating of GO releases enough gas during heating to inhibit diffusion mechanisms between Cu particles.

3.7. Raman

As a complement to SEM characterization, the efficacy of the synthesis method was also inspected with Raman spectrometry. The coating thickness and uniformity could be qualitatively verified by creating mappings of characteristic G bands from GO on compressed green bodies of GO@Cu samples.

Fig. 12 shows the optical microscopy images and mapping of the G band signal intensity for samples 0.1%-GO@Cu-7 to 1.5%-GO@Cu-7. As shown in Fig. 12a) and Fig. 12b), the G band signal is detectable even on 0.1%-GO@Cu-7 and 0.3%-GO@Cu-7, respectively. The G band intensities increase with even higher APTES loading, as shown by progressively stronger features in the G band mapping in Fig. 12c) to Fig. 12e). While the G band intensity increase is substantial from 0.1vol% to 0.3vol% APTES loading, it is subtler between 0.3vol% to 0.8vol% APTES loading. Increasing the APTES loading from 0.8vol% to 1.5vol% causes the G band signal to further strengthen, nearly saturating the mapping area.

This increase in coating coverage correlates with the SEM images in Fig. 6, for which the sample synthesized with 1.5% APTES displayed the most uniform and widespread coverage of GO. However, the optical microscopy images in Fig.12a) to Fig. 12e) also reveal a gradual increase in graphitic GO, shown as black spots. In other words, increasing the APTES concentration not only improves the electrostatic attraction to GO monolayers and increases coverage rate as a result, but can also be detrimental in the sense that the electrostatic attraction becomes strong enough to retain multilayer, i.e. graphitic GO.

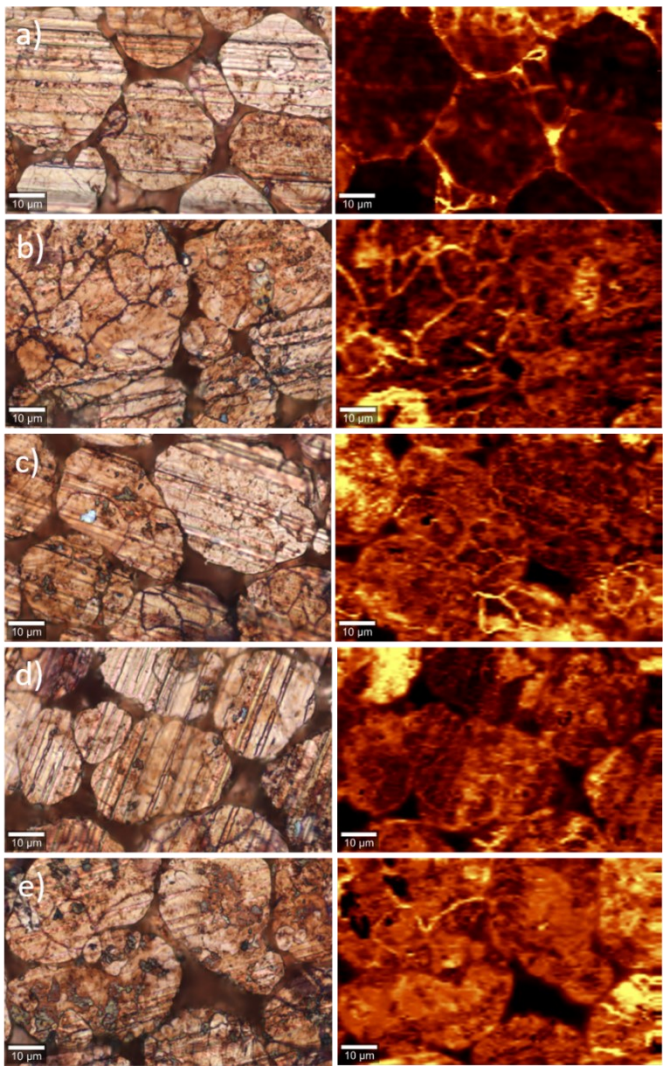

Figure 12: *Optical images (left) and Raman mapping (right) of unsintered GO@Cu samples. The samples were synthesized with a) 0.1%, b) 0.3%, c) 0.5%, d) 0.8% and e) 1.5% APTES for 8 hours. The scale bars represent 10 µm.*

Additional Raman analysis was conducted on sintered composites to investigate the preservation and quality of graphene after heat treatment. Fig. 13a) to Fig. 13c) shows the optical microscope images and corresponding Raman spectra of a cross section from a sintered rGO@Cu composite (0.25wt‰ GO, 0.1vol% APTES, 3 hours), which had been undergone thermal reduction prior to compaction at 1.25 GPa and sintering at 1050 °C for 4 hours.

The three spectra, taken at the fracture surfaces shown by optical microscopy, all display significant signal intensities for D and G bands at 1350 cm^{-1} and 1580cm^{-1} and indicate that rGO persists within the Cu matrix after sintering. The a) red and b) blue spectra also show bands for CuO at 520 cm^{-1}, as well as Si from APTES at 630cm^{-1} at 1000cm^{-1}. The large bands at 50cm^{-1} to 100cm^{-1} are artefacts from the background subtraction and convolutes additional bands for CuO, which would normally be found

at 290 cm^{-1} and 340 cm^{-1}. No 2D band at ~2700 cm^{-1} were found at these sites, nor in other ones within the structure.

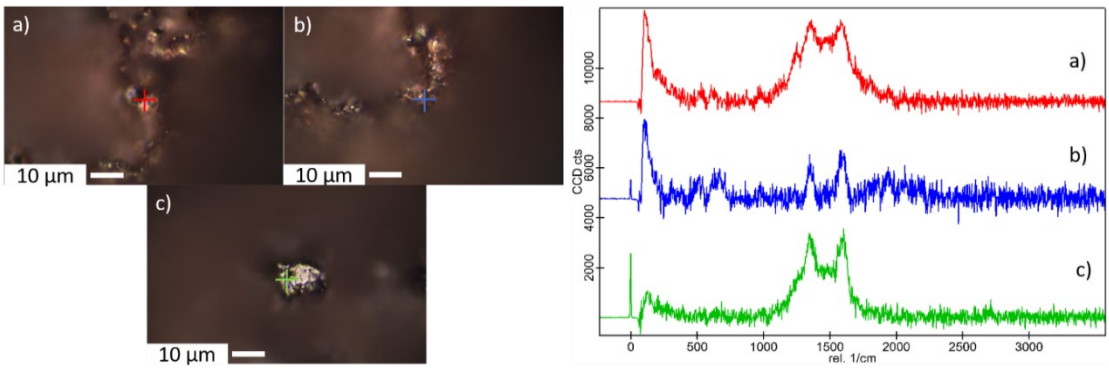

Fig. 13: *Raman analysis on the cross section of the sintered Cu-rGO sample. The spectra are taken at the location of the marker, shown in the center of the respective optical images.*

3.8. Thermogravimetric analysis (TGA)

TGA was used to investigate the thermal stability of APTES and GO on Cu. Fig. 14 below shows the thermal weight loss profile of Cu and two GO@Cu composite powders, which were heated from room temperature to 1000 °C at 5 °C/min. One sample, GO@Cu-3, was synthesized with a thin GO coating (0.25wt‰ GO, 0.2vol% APTES, 30 min) whereas the other had a thicker coating and has previously been shown in Fig. 5 as GO@Cu-2 (0.625wt‰. 2.5vol% APTES, 15 hours).

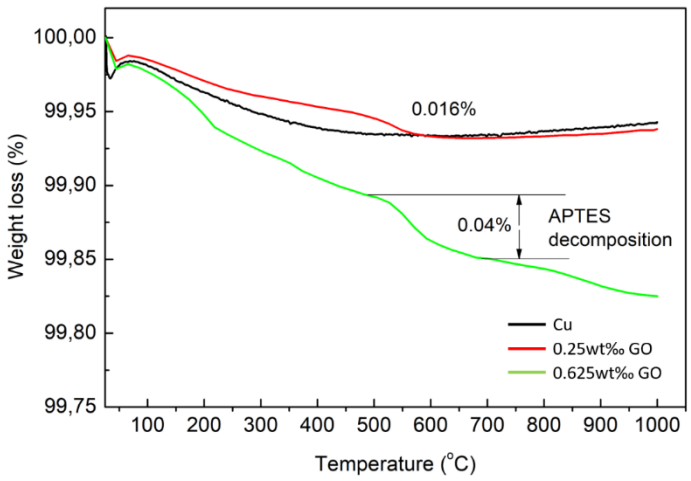

Figure 14: *TGA curves of Cu together with GO@Cu-3 (0.25wt‰ GO) and GO@Cu-2 (0.65wt‰ GO) composite powders.*

As shown in the TGA curve, the weight loss in Cu commences at 100 °C and slows down gradually before flatlining at ~99.95wt% remaining weight. The weight loss in

Cu constitutes amorphous carbon impurities and thermodynamically labile surface oxides. The sample GO@Cu-3 undergoes a similar same weight loss event involving decomposition of $CuO/Cu_2O/Cu(OH)_2$ until 520 °C. However, the smooth weight loss transition from 70 °C to 520 °C indicates that there was no significant release of intercalated water or decomposition of labile oxygen functional groups on GO. This can be explained by the thin, few-layered GO coating in GO@Cu-3 intercalating significantly less water molecules than Cu@GO-2. Moreover, a thinner GO coating implies fewer oxygen functional groups which can decompose to CO_2 and CO. In contrast, the sample GO@Cu-2 decomposed at a linear rate between 100 °C to 500 °C. The initial weight loss starting at 70 °C owes to dehydration of intercalated water in the GO layers. This dehydration continues until 200 °C, after which decomposition of labile oxygen groups in GO dominates until 350 °C. These functional groups are mostly hydroxides and epoxides. At 350 °C, a small weight loss event is observed for GO@Cu-2, indicating the onset at which more stable oxygen groups in GO decompose. In both GO@Cu-3 and GO@Cu-2, the decomposition of APTES begins at 520 °C and results in a 0.016% and 0.04% weight loss, respectively. In other words, if one compares the weight loss with APTES concentration, the sample Cu@GO-2 lost 12.5 times less weight than GO@Cu-3.

3.9. Chloric acid (HCl)

The weight loss profile for sintered GO@Cu and rGO@Cu samples are shown in Fig. 15.

The weight loss was most significant for the sintered GO@Cu samples until 250 hours of etching, after which the etching of Cu accelerates due to increased porosity. At this point the composites display higher corrosion resistance than Cu – only 7% of the original weight of Cu remains, whereas ~50% of the weight remains for the GO@Cu-2 (0.625wt‰ GO) composites and the sample rGO@Cu-3 (0.2wt‰ GO) has 70% remaining weight. Also, it is worth noting that the rGO@Cu sample which was synthesized with a thin coating (rgO@Cu-3) outperformed sintered Cu, as well as rGO@Cu-2 and GO@Cu-2 synthesized with 0.625wt‰ GO. HCl is highly erosive to metals due to Cl^- forming structurally weak metal chlorides, which caused the Cu sample to disintegrate after 260 hours while some GO@Cu remained. Similarly, the GO@Cu-2 composites etched at an accelerated rate due to the high internal porosity through which HCl could propagate. However, once saturated by HCl, the diffusion of H^+ and Cl^- ions are inhibited by GO and rGO, the latter being slightly hydrophobic.

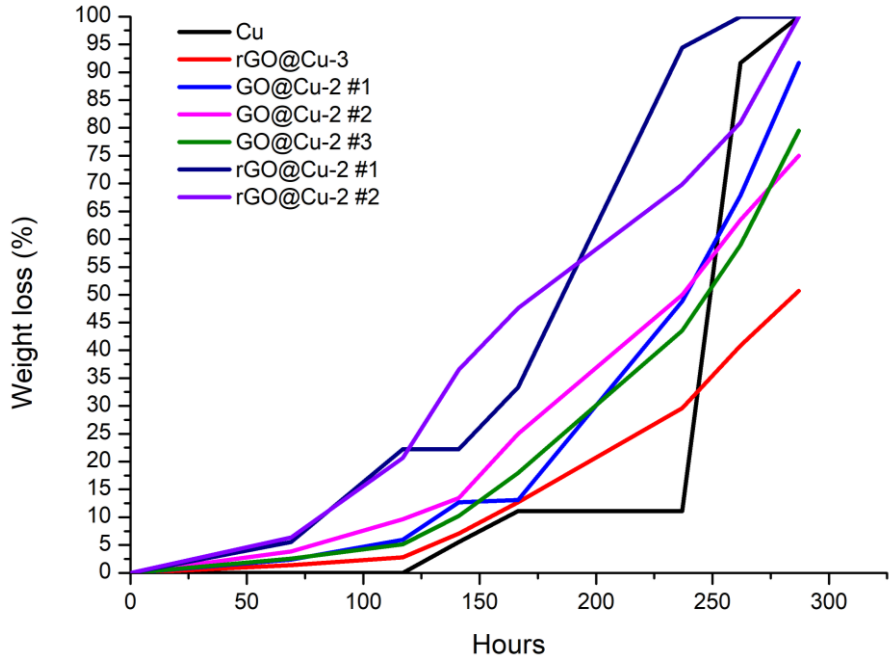

Figure 15: *Etching sintered samples in 37% HCl.*

3.10. Ammonium persulfate (APS)

Fig. 16 shows corrosion weight loss curves for Cu and GO@Cu-2 (a), Cu and rGO@Cu powders synthesized with various amounts of APTES (b) and finally Cu and GO@Cu-7 powders with synthesized with APTES concentrations between 0.1vol% to 1.5vol% (c).

After 3 hours of etching in 0.5M APS, all GO@Cu samples show lower weight loss than Cu. As shown in Fig. 16a), the sample GO@Cu-2 (0.625wt‰ GO) lost only 8% weight compared with original Cu, which lost 15%. In comparison, the weight loss observed for Cu-rGO powders began approximating that of Cu after 1 hour in APS. The rate of weight loss for rGO@Cu powders (Fig. 16b)) followed no clear trend with APTES concentration. Moreover, the GO@Cu-7 composite powders, which were synthesized with 1wt‰ GO and APTES concentrations between 0.1vol% and 1.5vol%, show variance in weight loss after 3 hours. Interestingly, the samples synthesized with 0.5vol% to 1.5vol% APTES have lost more weight than the GO@Cu made with 0.1vol% and 0.3vol% APTES. In the latter case, the weight loss is between 8.2% and 7.4%, respectively. In addition, rGO@Cu lost 7-8% mass after 1 hour in APS, while GO@Cu lost between 6-7% mass. Within the first 30 minutes of etching, this difference is even more significant with GO@Cu losing 4-6% mass while rGO@Cu lost 7-8%.

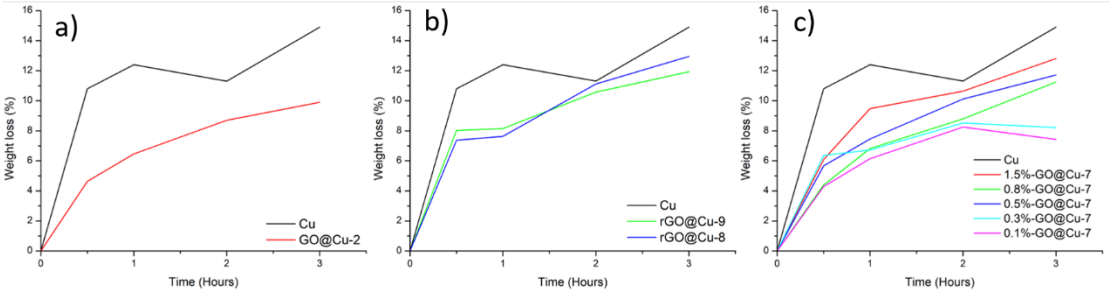

Figure 16. *Etching of Cu and a) 0.625wt‰ GO@Cu, b) 1wt‰ Cu-rGO and c) 1wt‰ GO@Cu with various APTES concentrations in 0.5M APS.*

3.11. Potentiodynamic polarization curves

Figure 17 shows the polarization curves for compacted green bodies of Cu and GO@Cu-7 composites, synthesized with APTES concentrations from 0.1vol% to 1.5vol%. These GO@Cu composites are identical to the ones presented in Fig. 6.

Compared to compacted Cu powder, the GO@Cu-7 green bodies all exhibit E_{corr} shifted from -0.46V and reduced cathodic polarization potentials while retaining the same anodic polarization potential. In other words, the kinetics of the anodic reactions $Cu(s) \rightarrow Cu^{2+}+2e^-$ and $Cu(s) \rightarrow Cu^{+}+e^-$ have not been significantly affected by the inclusion of APTES nor GO. On the other hand, reduction reactions on the Cu surface have become inhibited. This shift in corrosion potential correlates with APTES loading and thus GO coating uniformity, as indicated by a +0.12V shift for 0.1% Cu-APTES and +0.15V for 1.5% APTES. The GO@Cu composite powders synthesized with 0.5% and 0.8% APTES exhibit slightly higher positive shift, which implies that the cathodic corrosion inhibition is not dominated by APTES coverage alone. It should be mentioned that for these results, the E_{corr} for Cu is -0.46V and deviates from the values presented in literature[19], which is closer to -0.35V. This lower corrosion potential could be an effect of higher surface area due to porosity.

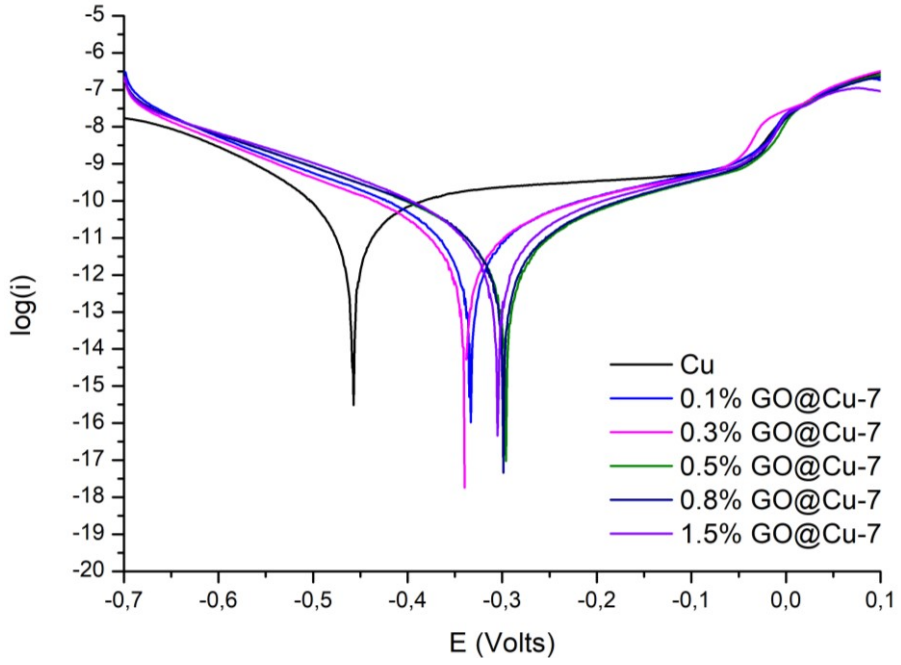

Figure 17: *Polarization curves of green bodies of Cu and GO@Cu synthesized with various concentrations of APTES. All samples were synthesized with 1wt‰ GO and 8 hours synthesis time.*

These results show that a APTES-GO surface treatment of Cu powder can inhibit the cathodic corrosion reaction, by virtue of acting as an oxygen diffusion barrier. The corrosion protection behavior for sintered GO@Cu-2 composites was also investigated and compared with sintered Cu. These resulting polarization curves are shown in Fig. 18 and indicate that reduction of GO@Cu prior to sintering is paramount for retaining a protective layer on the composite surface. In this graph, the nearly identical polarization of Cu and GO@Cu-2 (0.625wt‰, 2.5vol% APTES) imply that the outer surface of the composite has been stripped of GO during the sintering. In contrast, the surface of the Cu-rGO composite is sufficiently passivating to result in a +0.9V shift in E_{corr} to -0.206V and a reduction of the corrosion current i_{corr} from $7.14*10^{-6}$ A/cm^2 to $3.86*10^{-7}$ A/cm^2.

Thermal reduction of the coated particles has also affected the polarization kinetics. The anodic domain in rGO@Cu-2 displays a passivated regime that is absent in the samples of Cu and GO@Cu-2, resulting in log(i) only changing by 0.5 between -0.45V < E < -0.27V. Hence, within the interval -0.45V to -0.3V the log(i) for the Cu sample changes nearly four times as quickly as the rGO@Cu-2 composite. In addition, log(i) in the cathodic domain between -0.206V and -0.07V is initially much lower than for both the Cu and GO@Cu sample. However, as shown in figure 37, the asymmetric polarization curve for rGO@Cu indicates that there is no passivation for the cathodic reaction and that the corrosion rate accelerates from E > -0.15V. In other words, the rGO coating can passivate the sample surface to limit anodic decomposition of Cu and

the cathodic reaction involving reduction of solvated oxygen, yet the cathodic reduction of oxygen is diffusion limited and the passivating effect breaks down quickly when increasing the potential.

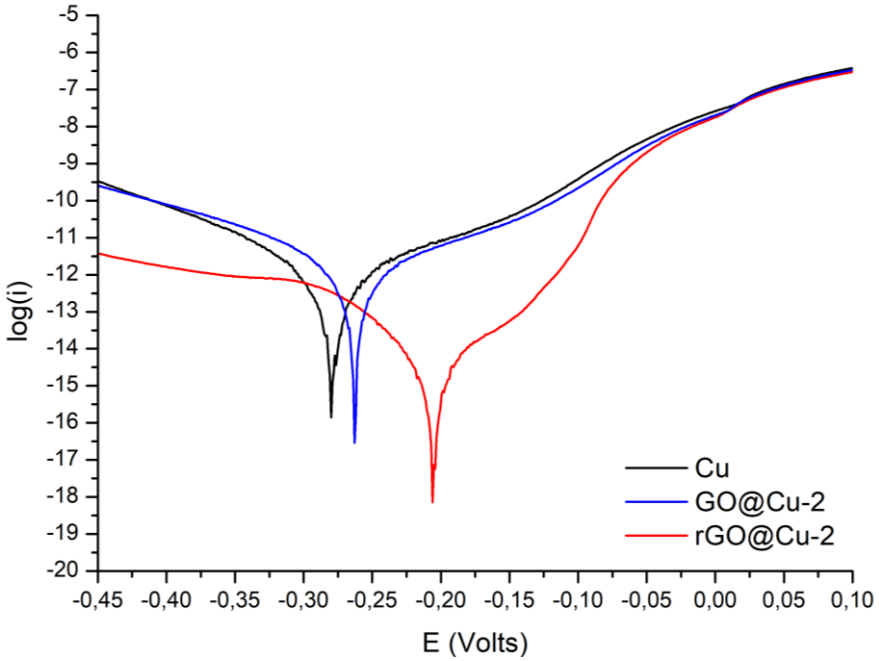

Figure 18: *Polarization curves of Cu and sintered GO@Cu composites with thick powder coating (0.625wt‰ GO) and 2.5vol% APTES.*

The polarization curves in Fig. 17 and Fig. 18 were fitted to Tafel plots to obtain estimates for $i_{Corr.}$. Table 3 below summarizes the parameters used, as well as the resulting i_{Corr} and error function χ^2. The high values for χ^2 for the sintered samples are due to fitting the model based on points that were within 0.03V to E_{Corr}. The results show that i_{Corr} values for the GO@Cu-7 and GO@Cu-2 samples are at the same order of magnitude as Cu. In other words, most of the GO on the composite's outer surface is removed during sintering and that which remains is insufficient to provide to inhibit oxygen diffusion or passivate the surface oxides. On the other hand, sintered Cu-rGO powder exhibits a corrosion current of $3.86*10^{-7}$ A/cm^2, which is one order of magnitude lower than sintered Cu.

Table 9: Tafel parameters

Sample type	Sample	GO (wt‰)	APTES (vol%)	β_a (mV)	β_c (mV)	I_{Corr} (A/cm^2)	E_{Corr} (V)	X^2
Green body	Cu	1	0.1	140	90	$1.91*10^{-5}$	-0.457	54.1
	0.1%-GO@Cu-7			277	211	$2.02*10^{-5}$	-0.333	35.4
	0.3%-GO@Cu-7		0.3	420	270	$2.67*10^{-5}$	-0.339	33.3
	0.5%-GO@Cu-7		0.5	370	270	$2.36*10^{-5}$	-0.296	15.43
	0.8%-GO@Cu-7		0.8	320	250	$2.08*10^{-5}$	-0.298	35.4
	1.5%-GO@Cu-7		1.5	330	260	$2.23*10^{-5}$	-0.303	36.1
Sintered composite	Cu			200	160	$7.14*10^{-6}$	-0.279	113
	GO@Cu-2			80	78	$5.31*10^{-6}$	-0.278	103
	rGO@Cu-2			65	62	$3.86*10^{-7}$	-0.206	90.5

4. Discussion

XPS analysis indicates that APTES preferentially forms covalent bonds with Cu via condensation reactions with $Cu(OH)_2$, as evidenced by a reduction of detected Cu^{2+} binding energy. This allows $-NH_2$ to protonate in water and form electrostatic interaction with GO. Moreover, it was established APTES can covalently bond to Cu within 30 minutes in toluene to yield GO@Cu composite powders with thin (~50 nm) GO coatings.

Interestingly, SEM characterization showed that no clear morphological distinction was found between GO@Cu powders synthesized with 0.2vol% and 2.5vol% APTES for 30 minutes. Although the GO concentration used in synthesizing these GO@Cu composites varied from 0.2wt‰ to 1wt‰, the resulting GO coating was always thin. Extending the APTES treatment time to 8 hours and varying the APTES concentration between 0.1vol%-1.5vol% yielded a similar result, in which the GO coating on GO@Cu-7 samples could only be found at high SEM magnification (20000x). However, while extending the APTES@Cu synthesis time to 8 hours had no strong effect on coating thickness, it did promote uniformity of the GO coating as shown by Raman mapping of compacted green bodies of GO@Cu-7. In the samples synthesized with 0.8vol% (0.8%-GO@Cu) and 1.5vol% (1.5%-GO@Cu) APTES, some pieces of graphitic GO were decorating the GO@Cu surface. In contrast, synthesis of GO@Cu samples with visibly thicker GO coatings required a combination of higher APTES concentrations and treatment duration. After 15 hours treatment with APTES, an APTES@Cu composite powder synthesized with 2.5vol% APTES could electrostatically interact with both 0.625wt‰ GO (GO@Cu-2) and 33wt‰ GO

(GO@Cu-1), respectively. However, while the GO@Cu-2 particles displayed no aggregation yet had GO coatings consisting of multilayers, the GO@Cu-1 powders were heavily aggregated.

These results indicate that the morphology and thickness of GO on GO@Cu composite powders can be precisely controlled by modulating the total positive charge bestowed by hydrolyzed APTES on the particle surface. The need for extended APTES treatment time to create GO@Cu powders with thick GO coating can be attributed to the steric effect of assembled APTES on Cu. While an incomplete APTES monolayer on Cu can be synthesized within 30 minutes, the formation of a dense layer of APTES becomes progressively inhibited as more APTES crowds the Cu surface.

Thermal reduction of GO@Cu-2 for 2 hours at 400 °C in argon was adequate to lower the oxygen content in GO from ~50wt% to ~10wt%. In addition, the GO coating did not suffer any visible damage such as flaking or delamination from the Cu surface. This may be attributed to the trace amounts (0.1wt%) of APTES remaining on the rGO@Cu surface, which can anchor the rGO to Cu. TGA analysis of GO@Cu-2 and GO@Cu-3 shows that surfactants and oxygen functional groups are not completely removed before reaching 500°C, at which point the GO coating pyrolyzes.
Moreover, thermal reduction of GO@Cu to rGO@Cu significantly reduced the formation of internal pore structures in compacted and sintered samples. This attributes pore formation to the release of carbonaceous gases when heating GO from 70 °C to 500 °C, which can be prevented with thermal reduction of GO@Cu prior to sintering. It was also observed that this thermal reduction of GO@Cu to rGO@Cu influenced the corrosion resistance of both sintered samples in 37% HCl and freestanding composite powder in 0.5M APS. While the initial corrosion rates of rGO@Cu samples in 37vol% HCl were higher than Cu due to higher porosity and low rGO content on the outer sample surface, the higher rGO content in the core of the composites resulted in preservation of 20% to 70% of the sample mass after 250 hours of corrosion. In comparison, pure Cu disintegrated after 240 hours due to embrittlement caused by Cl^-. The best corrosion protection was provided by rGO@Cu-3, which had been synthesized with a thin GO coating by grafting 0.2vol% APTES to Cu for 30 minutes. A similar result was obtained by corroding GO@Cu samples in 0.5M APS, which showed that a GO@Cu powders synthesized with a thin GO coating (0.1%-GO@Cu-7 and 0.3%-GO@Cu) performed better than rGO@Cu, Cu and GO@Cu-7 powders synthesized with more APTES. The cause for lower corrosion protection with rGO@Cu may be attributed to introduction of defects and structural damage during the thermal reduction process. As for the discrepancy between higher APTES content and anticorrosion performance, it can be attributed to the increased presence of graphitic GO and uneven coating caused by stronger electrostatic interaction with GO. In presence of APS, electrostatic bond between APTES and these heavy surface features may be weakened to the point of detachment, thus revealing exposed Cu. Polarization of green bodies of GO@Cu-7 samples revealed that a dual coating of APTES and GO does not reduce the corrosion rate appreciably but does offer some protection against cathodic reactions by inhibiting diffusion of oxygen. This effect was observed to greater effect in sintered

rGO@Cu-2, which displayed significantly lower i_{corr}, lower cathodic reaction rate and a higher corrosion potential than sintered Cu.

5. Conclusion

The work presented herein shows that GO@Cu composite powders can be synthesized in a scalable solution mixing process by grafting the silane 3-aminopropyltriethoxysilane (APTES) onto commercial Cu powder in toluene, followed by addition of a dispersion of commercially available graphene oxide (GO). The surface morphology could be precisely controlled by modifying APTES concentration and duration of surface functionalization. The synthesized GO@Cu powder demonstrates good stability, as it does not decompose during thermal reduction at 400 °C, nor is the electrostatic interaction between APTES and GO deteriorated by exposure to water. Thermal reduction of GO@Cu before sintering greatly improved the density of the composite due to reduced gas release, and increased hydrophobicity provided by rGO improved the coatings anticorrosive properties after consolidation and sintering.

Acknowledgements

The authors gratefully acknowledge the received funding from the European Union's Horizon 2020 research and innovation program under GrapheneCore2 785219 – Graphene Flagship.

References

1. Xu, X. *et al.* Greatly Enhanced Anticorrosion of Cu by Commensurate Graphene Coating. *Adv. Mater.* **30**, 1–7 (2018).

2. Yu, L. *et al.* A graphene oxide oxygen barrier film deposited via a self-assembly coating method. *Synth. Met.* **162**, 710–714 (2012).

3. Pierleoni, D. *et al.* Selective Gas Permeation in Graphene Oxide − Polymer Self-Assembled Multilayers. (2018) doi:10.1021/acsami.8b01103.

4. Zahran, R. R., Ibrahim, I. H. M. & Sedahmed, G. H. The corrosion of graphite/copper composites in different aqueous environments. *Mater. Lett.* **28**, 237–244 (1996).

5. Ren, S. *et al.* N-doping of graphene: toward long-term corrosion protection of Cu. *J. Mater. Chem. A* **6**, 24136–24148 (2018).

6. Roy, S. S. & Arnold, M. S. Improving graphene diffusion barriers via stacking multiple layers and grain size engineering. *Adv. Funct. Mater.* **23**, 3638–3644 (2013).

7. Sun, J. *et al.* Multiple-bilayered RGO-porphyrin films: From preparation to application in photoelectrochemical cells. *J. Mater. Chem.* **22**, 18879–18886 (2012).

8. Sun, J., Xiao, L., Meng, D., Geng, J. & Huang, Y. Enhanced photoresponse of large-sized photoactive graphene composite films based on water-soluble conjugated polymers. *Chem. Commun.* **49**, 5538–5540 (2013).

9. Zhu, D. & Van Ooij, W. J. Corrosion protection of metals by water-based silane mixtures of bis-[trimethoxysilylpropyl]amine and vinyltriacetoxysilane. *Prog. Org. Coatings* **49**, 42–53 (2004).

10. Bajat, J. B. *et al.* Corrosion protection of aluminium pretreated by vinyltriethoxysilane in sodium chloride solution. *Corros. Sci.* **52**, 1060–1069 (2010).

11. Bera, S., Rout, T. K., Udayabhanu, G. & Narayan, R. Water-based & eco-friendly epoxy-silane hybrid coating for enhanced corrosion protection & adhesion on galvanized steel. *Prog. Org. Coatings* **101**, 24–44 (2016).

12. Zhu, H. *et al.* Fabrication and characterization of self-assembled graphene oxide/silane coatings for corrosion resistance. *Surf. Coatings Technol.* **304**, 76–84 (2016).

13. Geng, Y. *et al.* Fabrication of superhydrophobicity on foamed concrete surface by GO/silane coating. *Mater. Lett.* **265**, 127423 (2020).

14. Raza, M. A., Rehman, Z. U. & Ghauri, F. A. Corrosion study of silane-functionalized graphene oxide coatings on copper. *Thin Solid Films* **663**, 93–99 (2018).

15. Nieto, A., Bisht, A., Lahiri, D., Zhang, C. & Agarwal, A. Graphene reinforced metal and ceramic matrix composites : a review. **6608**, (2016).

16. Zhang, X. *et al.* A powder-metallurgy-based strategy toward three-dimensional graphene-like network for reinforcing copper matrix composites. *Nat. Commun.* **11**, 1–13 (2020).

17. Li, Y. *et al.* Additive manufacturing high performance graphene-based composites : A review. *Compos. Part A* **124**, 105483 (2019).

18. Poreddy, R., Engelbrekt, C. & Riisager, A. Catalysis Science & Technology dehydrogenation of alcohols with air †. 2467–2477 (2015) doi:10.1039/c4cy01622j.

19. Kear, G. Electrochemical corrosion of unalloyed copper in chloride media — a critical review. *Corros. Sci.* **46**, 109–135 (2004).